A Close Look at Molecular Self-Assembly with the Transmission Electron Microscope

Aoon Rizvi,[1] Justin T. Mulvey,[2] Brooke P. Carpenter,[1] Rain Talosig[1] and Joseph P. Patterson[1]*

[1]*Department of Chemistry, University of California, Irvine, Irvine CA 92697-2025*

[2]*Department of Materials Science and Engineering, University of California, Irvine, Irvine, CA 92697-2025*

Corresponding author email: patters3@uci.edu

ABSTRACT:

Molecular self-assembly is pervasive in the formation of living and synthetic materials. Knowledge gained from research into the principles of molecular self-assembly drives innovation in the biological, chemical, and materials sciences. Self-assembly processes span a wide range of temporal and spatial domains and are often unintuitive and complex. Studying such complex processes requires an arsenal of analytical and computational tools. Within this arsenal, the transmission electron microscope stands out for its unique ability to visualize and quantify self-assembly structures and processes. This review describes the contribution that the transmission electron microscope has made to the field of molecular self-assembly. An emphasis is placed on which TEM methods are applicable to different structures and processes and how TEM can be used in combination with other experimental or computation methods. Finally, we provide an outlook on the current challenges to, and opportunities for, increasing the impact that the transmission electron microscope can have on molecular self-assembly.

Table of Contents

1. Introduction

Molecular self-assembly is the spontaneous organization of molecules into higher order structures.[1–3] The use of the term spontaneous is important as it indicates that the process of self-assembly has a negative free energy change. As such, self-assembly processes can be represented by a free energy landscape.[4] The free energy landscape describes all possible microstates (configurations) as a function of their free energy. Self-assembly processes are a change in the microstate, going from a high energy position in the free energy landscape to a lower energy position. The free energy landscape is determined by the thermodynamics of the system, which depends on parameters such as the molecular structure of the building blocks, the medium of self-assembly, and the temperature. Self-assembly processes are initiated by a change in the system parameters such that a new, lower energy microstate becomes accessible. A full understanding of a self-assembly process requires a description of the initial and final microstates as well as the kinetic mechanisms by which these microstates are connected. This complete understanding is essential for the rational design of functional self-assembled systems as their functionality is dependent on their structure and structural dynamics.

Self-assembly processes can be described by a complexity continuum. Simple processes consist of a small number of building blocks and microstates, assemble down a single pathway, evolve homogeneously (only one microstate is observed at each sampled time point), and form atomically precise structures that can be described by a few parameters. Complex processes can have multiple building blocks and microstates, assemble down multiple pathways, evolve heterogeneously, and form high dispersity structures that require many parameters to be accurately described. Self-assembly processes are studied throughout the chemical, biological, and materials sciences and have been applied in medicine, catalysis, separation science, energy conversion and storage, and sensing applications.[1–3] Common precursors for self-assembled

materials include small molecules, polymers, and biological molecules. These building blocks range from a few angstroms to nanometers in size, while their assembled structures can range from the nanoscale to the macroscopic scale.[1,5] The assembly process can occur in 1, 2, or 3 dimensions (3D) and can take place over timescales that range from nanoseconds to multiple days.[6,7] The vast continuum of space, time, and complexity makes understanding self-assembly a grand challenge, requiring multiple experimental, computational, and theoretical methods. Within our method arsenal, the transmission electron microscope (TEM) stands out as unique for its ability to ***discover, visualize, and quantify*** self-assembly mechanisms and structural features with atomic resolution.

In this review, we provide a comprehensive overview of how the transmission electron microscope has enabled a close look at molecular self-assembly. For molecular self-assembly to occur the building blocks must be mobile, for this reason self-assembly is often performed in solution or at an interface.[8] Solutions have historically presented a significant challenge for TEM analysis and is therefore a focus of this review. We begin with a brief overview of TEM including strengths and challenges. The article is then divided into sections that review some of the most common TEM methods (sections 3.1-3.7), including combined and correlative methods (sections 4.1- 4.5), and the application of TEM to specific material classes (sections 5.1-5.3). The article concludes with an outlook specifically focused on the application of TEM to the field of molecular self-assembly. After the outlook, an addendum is provided that describes some important aspects of TEM including sample preparation, electron-sample interactions, and image analysis. This section is referenced throughout the main text and is meant to serve as a non-technical guide. The section also provides relevant references to direct the reader to more detailed texts.[9]

2. TEM overview

Ernst Ruska developed the transmission electron microscope in the 1930s after discovering that a magnetic coil could be used as a lens to manipulate electron beams.[10,11] In comparison to photons of light, electrons have two key differences: a short wavelength (~pm) and a strong interaction with matter. These electron properties are advantageous in that they enable electron microscopes to achieve atomic resolution and image single atoms.[12] However, these properties also result in several disadvantages for electron microscopy: the specimen can be damaged by the electron-sample interactions, must be thin (typically < 1 micron),[13] [10] and the microscope must be under high vacuum. These disadvantages are key challenges for understanding self-assembly and can result in the collection of images which are not representative of the native self-assembly process. However, enormous efforts have been made to quantify and overcome these challenges and take advantage of the high resolution and sensitivity of electron microscopes. These efforts have resulted in the development of a plethora of TEM methods, each with benefits and limitations. When designing a TEM experiment, it is essential to consider the motivation for using this instrument. TEM can be used for ***discovery, visualization, and quantification***. One of the biggest and most fundamental challenges in molecular self-assembly is that the processes are occurring in time and space domains that are extremely far away from our everyday experience. Visualization of the structures and processes throughout the assembly mechanism is the most reliable and useful way to guide our research and teaching of molecular self-assembly. Even for structures that can be determined by scattering experiments alone, TEM experiments are often performed to provide easily interpretable data - an image. TEM can also be used to quantify structural or dynamic features of a sample such as particle size distributions, the ratio of different morphologies within a single sample, particle growth kinetics, and particle fusion times. Quantification experiments can guide the design and optimization of synthetic procedures and improve our understanding of structure-property relationships. For these experiments, it is essential that the data is collected efficiently and with sufficient quality to make the required measurements. TEM can also be used for the discovery of new structures and dynamic

processes.[14] This is perhaps the most important and exciting function of the TEM. Discovery can often happen serendipitously when attempting to visualize or quantify systems that are believed to be understood, but it can also occur through deliberate investigation of a self-assembly process using a new TEM method.

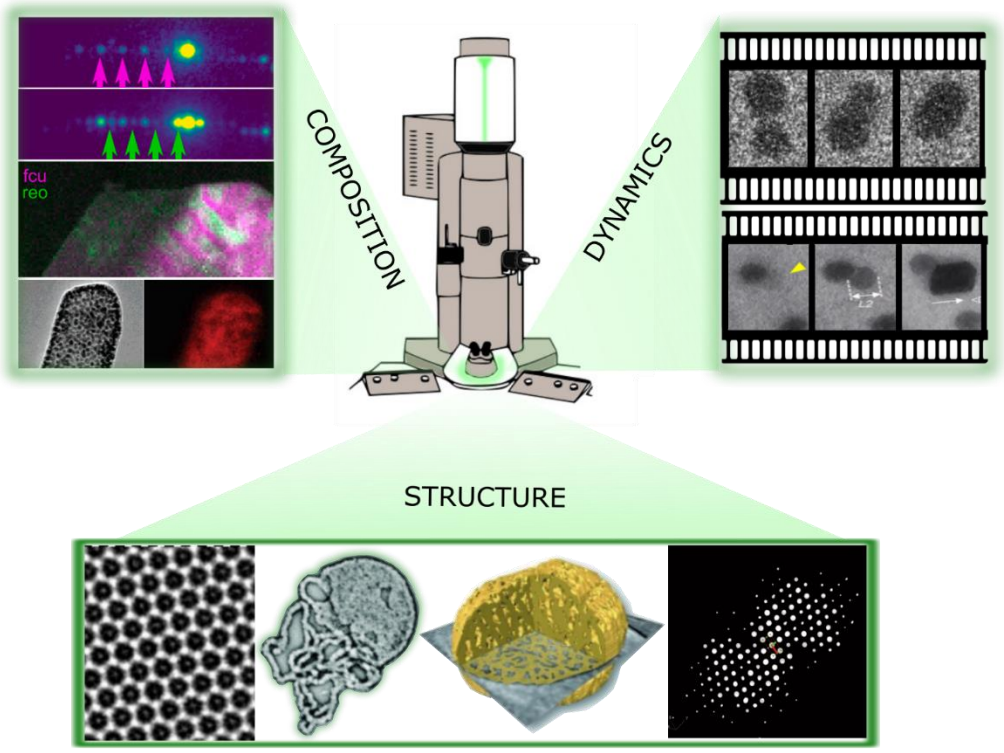

Figure 1: Overview of TEM data for molecular assemblies. The presented images are discussed in the following paper, the three panels present the compositional, structural, and dynamic capabilities of TEM. Reproduced with permission from ref (52). Copyright 2011 American Chemical Society. Reproduced with permission from ref (102). Copyright 2017 American Chemical Society. Reproduced with permission from ref (111). Copyright 2017 National Academy of Sciences. Reproduced with permission from ref (186). Copyright 2010 American Chemical Society. Reproduced with permission from ref (204). Copyright 2007 American Chemical Society. Reproduced with permission from ref (214). Copyright 2021 American Chemical Society.

Reproduced with permission from ref (63). Copyright 2019 Elsevier. Reproduced with permission from ref (149). Copyright 2018 Wiley and Sons.

2.1 Strengths and challenges

The main strengths of TEM are that it can provide both real-space and reciprocal-space projection images of individual nanoscale objects. This contrasts with scattering methods that provide ensemble reciprocal space information. Thus, TEM is especially useful for the analysis of complex self-assembly processes. For example, comparing TEM analysis of samples that contain a single morphology or multiple morphologies. The sample with multiple morphologies requires more individual particles to be imaged to obtain a representative view. This increases the analysis time, but the quality of the data for the single morphology or multiple morphology sample is the same, because particles are analyzed individually. In contrast, scattering data on the multiple morphology sample requires a model with more parameters compared to the single morphology sample. This increase of model complexity decreases the confidence with which the scattering data can be fit. The main challenges for TEM are: removing the sample from its native environment (the environment challenge), collecting data on large numbers of structures (the statistics challenge), choosing which particles to image and present is subjective (the representation challenge), and measuring samples can affect the observation (beam damage challenge). These challenges, if not addressed, can result in an inaccurate description of the assembly process. The environment challenge can be addressed by cryogenic TEM (cryoTEM) (section 3.2) and liquid phase TEM (LPTEM) (section 3.3). Innovations in these areas have enabled imaging methods that are extremely close to the true native environment. The statistics challenge and the representation challenge are discussed in the conventional TEM section (section 3.1) and in the outlook section with reference to recent and future improvements in automation. The beam damage challenge is discussed in the electron-sample interactions section (section 7.4). In recent years, great improvements have been made in controlling and

understanding electron-sample interactions, and the beam damage challenge only remains in methods such as LPTEM, electron tomography, and atomic resolution imaging. Even with these challenges, TEM is one of the most useful methods to study molecular self-assembly. However, it is most powerful when combined with other analytical or computational methods. In section 4, we highlight combined and correlative TEM methods.

3. TEM methods

3.1 Conventional TEM

Conventional TEM can be defined by the absence of any advanced imaging method, such as those described in the following sections (section 3.2-3.7). For solution self-assembly studies, the specimen is typically prepared by depositing the sample solution onto a grid and letting the solution evaporate (section 7.2). The simplicity in sample preparation and imaging makes conventional TEM a useful approach for “high-throughput” imaging. In addition, the lack of a water or ice layer can help with the collection of high-resolution, high signal to noise images. Furthermore, conventional TEM is often the most convenient and accessible method. While conventional TEM has several advantages, the challenge with this approach is that some solution based molecular self-assemblies will partially or fully rearrange upon drying. This results in the collection of images that are not representative of the structure in its native environment. However, for assemblies that are formed in the bulk,[15] or are stable or partially stable upon drying useful information can be obtained. For example, it has been well established that high glass transition temperature polymers (e.g. polystyrene) are partially stable to drying,[16,17] and morphology assignment by conventional TEM is valid. A comparison of conventional TEM and cryoTEM was performed on Doxil, a liposomal nanocrystal formulation.[18] The comparison showed that while drying induced collapse of the liposomal membrane, the nanocrystal remained intact,

which was demonstrated by quantitative comparison of nanocrystal lengths. This is an important demonstration as it shows that even if some rearrangements occur, useful information on the native structure can still be obtained.

Conventional TEM is commonly used to visualize sample morphology and quantify structural features, such as particle size, when investigating self-assembly processes.[19,20] Examples include DNA origami,[21–24] metal-organic frameworks,[25–27] polymers,[19,28–33] small molecules,[34–36] and peptide-based nanomaterials.[37–40] In DNA based materials, conventional TEM allows for structural analysis based on slight modifications to the particles,[22,41] such as imaging the specific angle bends of anisotropic DNA based materials (Figure 2 iii).[42] In block copolymer systems, conventional TEM enables the exploration of large phase spaces due to the ease of sample preparation.[43–45] Additionally, conventional TEM has been used to image single-walled carbon nanotubes wrapped with semiconducting polymers.[46] The TEM images were used to quantify how "tightly" the polymer chain wrapped around the carbon nanotube, which influenced the electrical properties of the hybrid system (Figure 2 iv). These images would be extremely difficult to obtain using cryoTEM or LPTEM due to additional background scattering of the water layers. Assemblies formed from crystalline polymers tend to be stable to dehydration and are commonly imaged with conventional TEM.[47–49] For example, crystalline cylindrical block copolymer micelles have been analyzed by conventional TEM to quantify micelle growth.[19] Images were taken at different time points to quantify the change in the size distributions overtime which helped the kinetics of the assembly process.

For chiral assemblies, conventional TEM has enabled characterization of the helices.[50] For example, gemini surfactants were studied with TEM to determine how the pitch of the helix evolved as a function of building block length.[51] In addition, conventional TEM has been used to study the mechanism of self-assembly and morphological transformations. Imaging polystyrene based block copolymers at different stages in the assembly process revealed that block

copolymer vesicles exist in thermodynamic equilibrium.[20] It was hypothesized that size changes occur via fusion and fission events, due to the observation of fission/fusion intermediates. Conventional TEM has also been used to study vesicle formation and enabled the discovery of “jellyfish” intermediates (Figure 2 ii).[52] Additionally, small molecule dynamics like fullerene dimerization has been imaged in real-time, which revealed bond formation between two molecules as the initiation of the fusion process (Figure 2 i).[53] The spatial/temporal resolution required to make such observations would be extremely challenging or impossible with LPTEM. As the accessibility and capabilities of advanced imaging methods improve, we envision a decrease in the use of conventional TEM for studying molecular assemblies. However, conventional TEM will still likely be the preferred method when imaging large volumes of sample and when acquiring high-resolution, high signal to noise images of materials that are known to be stable to dehydration.

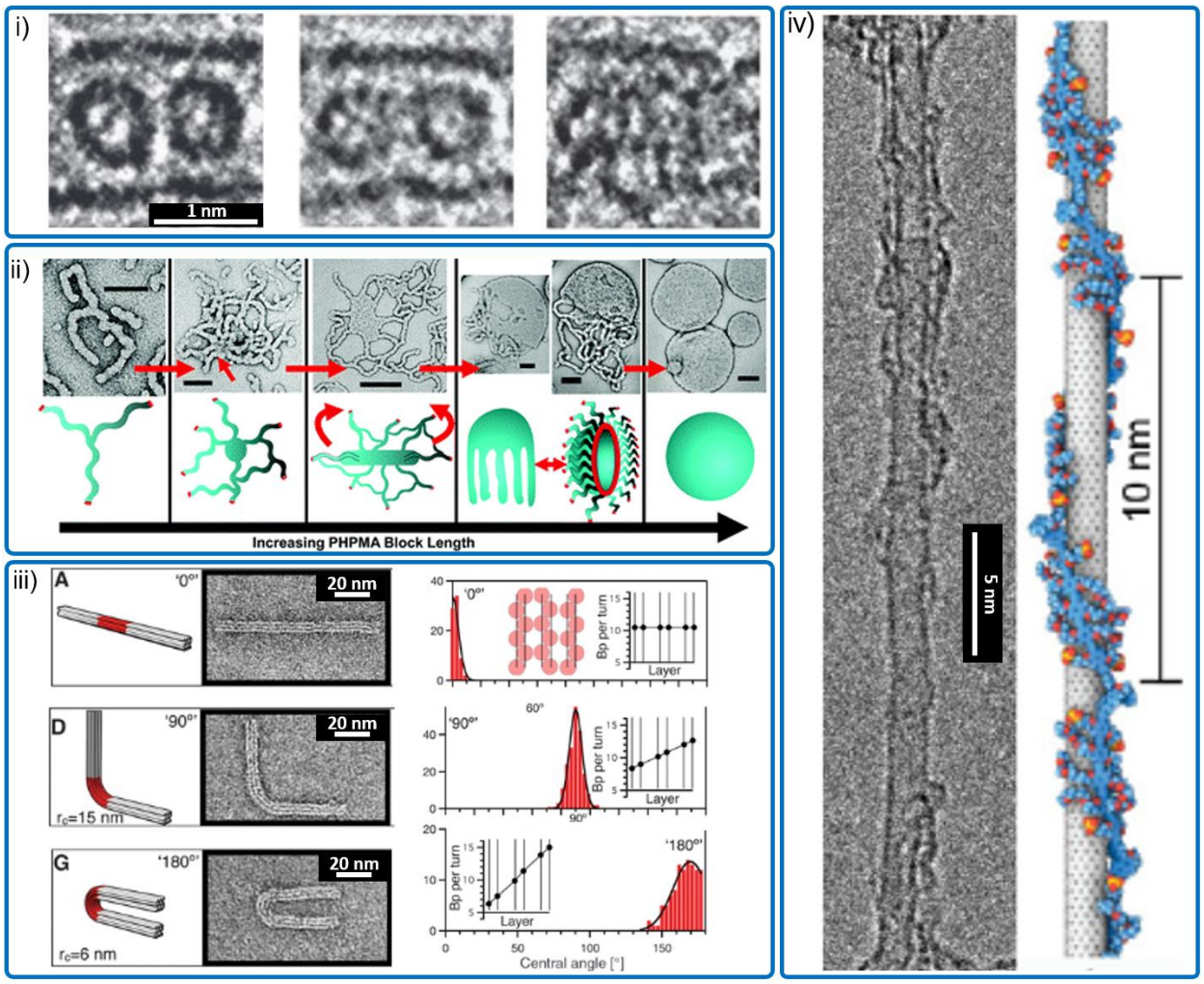

Figure 2: Molecular assemblies analyzed by conventional TEM. i) TEM image sequence of fullerene fusion process. Reproduced with permission from ref ([53]). Copyright 2010 Springer Nature. ii) Proposed mechanism for the polymerization-induced worm-to-vesicle transformation with "jellyfish" intermediates. Scale bars, 200 nm. Reproduced with permission from ref ([52]). Copyright 2011 American Chemical Society. iii) Site-directed bent shapes of DNA-origami observed by negative-stain TEM. Histograms of bend angles as observed in individual particles. Reproduced with permission from ref ([42]). Copyright 2009 AAAS. iv) TEM image of aryleneethynylene polymer wrapped around a carbon nanotube. Reproduced with permission from ([46]). Copyright 2013 American Chemical Society.

3.2 Cryogenic TEM

CryoTEM has revolutionized the characterization of self-assembled structures by enabling atomic resolution imaging of nanomaterials in their solution state.[54] Self-assembled structures are often stabilized by various solution conditions such as pH, concentrations, and temperature; thus, assemblies can become distorted and artifacts can appear in conventional TEM imaging. By vitrifying a thin layer (typically 10-300 nm) of the liquid sample, cryoTEM prevents sample dehydration, or loss of volatile molecules during imaging, and can also reduce electron beam damage by maintaining sample temperatures of ~120 K.[55,56] The importance of vitrification has been demonstrated by comparing images of solvated and dehydrated surfactant assemblies.[57] The evaporated sample images revealed several drying artifacts such as overly concentrated samples, altered microstructures, and formation of new nanostructures. Although mostly applied to aqueous samples, cryoTEM has enabled imaging of some samples in organic solvents,[58,59] including ionic liquids.[60] Furthermore cryoTEM has enabled time resolved studies with subsecond temporal resolution to visualize and quantify self-assembly mechanisms.[61,62] A key advantage of cryoTEM for studying self-assembly mechanisms is that transient intermediates can be “frozen” which enables them to be studied at high resolution. In section 3.5, we discuss how single particle analysis and electron tomography can be used to obtain 3D structural information. Both of these techniques are routinely performed under cryogenic conditions. While cryoTEM is typically performed on particles in solution, it can also be performed on “dry” particles, where the vitrification process and cryogenic imaging conditions are used to prevent the evaporation of volatile encapsulated molecules.[63] More details on the sample preparation for cryoTEM can be found in section 7.2.

<u>Structure Determination</u>

CryoTEM and single particle analysis (Section 3.2,3.5) have revolutionized the field of structural biology, demonstrated by the 2017 Nobel Prize in Chemistry.[64–66] CryoTEM is ideal for structure

determination as it requires little sample and does not require crystallization. Early efforts in obtaining high resolution images with cryoTEM were largely focused on viruses with icosahedral symmetry, with the hepatitis B virus core being the first structure to be reconstructed with atomic resolution (7.4 Å).[67] CryoTEM technologies have continued to advance and are now able to capture atomic resolution images of amino acid backbones in various virus particles (Figure 6i) .[68–70] Currently, the highest resolution cryoTEM reconstruction of a biomolecule is 1.22 Å, which was recorded with the protein apoferritin.[71] This advancement in resolution has enabled research in understanding how DNA packs within a condensate, which is particularly useful in gene therapy.[72] One study evaluated the packing of DNA in toroidal condensates and was able to conclude that hexagonal and nonhexagonal packing could be present in the same toroid. This helped support the model in which toroid formation is known to be nucleated by a single DNA loop. CryoTEM has also been used for structure determination in polypeptoid crystals,[73,74] and vesicles.[75] Polypeptoids are sequence defined polymers that are capable of assembling into biomimetic materials with defined structures. From rational design of material properties, it is essential to obtain atomic scale information on the supramolecular structures. CryoTEM was capable of capturing the a alternate packing of polypeptoids when a chiral substituent was installed in the backbone,[73] furthermore, cryoTEM was also used to visualize the direct relation ship in peptoid membrane morphologies with its respective block lengths.

CryoTEM and single particle analysis can be used to solve the structure of synthetic assemblies if they are highly symmetric. For example, self-assembled micelles formed from amphiphilic [3:3] hexakis adducts of C_{60} were characterized with cryoTEM, with some micelles being as small as 5 nm.[76] With atomic resolution imaging, it was possible to conclude that increasing the hydrophobic portion of the amphiphiles led to a higher density of amphiphile packing. However, most molecular assemblies are not ordered or symmetric enough to apply single particle analysis.[77] Therefore,

cryo-electron tomography (cryoET) (section 3.5) is typically preferred for obtaining 3D reconstructions of nonsymmetric self-assemblies.

Particle size and Morphology

CryoTEM is ideal for the determination of particle morphologies and quantification of structural features, especially for complex structures that are not stable to dehydration. For example, one study investigated the assembly of multicompartment micelles composed of three polymers: poly(ethylene oxide), poly(ethylethylene), and poly(perfluoropropylene oxide).[78] The structures formed from these polymers were complex, and cryoTEM was ideal to visualize the locations of the polymeric regions. Imaging the assembled multicompartment micelles provided information on the interactions dictating the final structures. In some studies, quantifying particle size distributions is essential to understanding the stabilization of the assembled structure as well as molecular packing parameters.[60,79] For example, a monodispersed vesicle sample was reported to be stabilized by a strong spontaneous curvature whereas polydisperse samples are stabilized by thermal fluctuations.[80] CryoTEM was also used to assess the core domain size of poly-butadiene-*block*-poly ethylene oxide micelles formed in ionic liquids to understand their packing characteristics, this was the first example of using block copolymers to self-assembly nanostructures in ionic liquids[81] In addition, cryoTEM is capable of determining topological defects that can arise in assembled structures. This can be particularly important when investigating whether branching occurs within a micelle.[82] Identifying defects further provides insight into the thermodynamics of systems since branched structures indicate a higher entropy. In one study, cryoTEM confirmed the formation of Y-junctions in high molecular weight diblock copolymer systems.[83] The Y-junctions were a result of decreasing the hydrophilic block length which allowed for the longer hydrophobic block to undergo rearrangement that favored complex geometries such as branching (Figure 3 ii).

Structure Interactions

The vitrification of samples is not only useful for preserving the solvated structures of individual particles but also the solvated interactions between particles. To study the interactions dictating the self-assembly of β-cyclodextrin (β-CD) in water, structures were imaged by cryoTEM after manipulating the β-CD concentration.[84] As the concentration of β-CD increased, small particles (~6 nm) were observed to aggregate to form branched structures (30 -100 nm) with uniform thickness. Further studies of aggregated particles found particles to interact only on their surfaces or fuse together to form a homogeneous aggregate, which provided evidence for supramolecular assemblies of β-CD in water at 3mM concentrations or above. The shape of particle aggregates can further be altered based on electrostatic interactions between neighboring particles as well as the ionic strength of the solution. In a structural study, polyelectrolyte chains were found to collapse as a result of increasing the ionic strength of a solution.[85] In addition, the shape of the polyelectrolyte chains could be further manipulated to form irregular shapes in response to encountering other charged particles in solution (Figure 3 iii). Although visualizing the micelle coronas can be difficult as they are highly solvated, the size of the corona can still be predicted based on the distance measurements between cores of adjacent micelles that are closed packed in vitrified ice layer.[78] In addition, cryoTEM can also be applied to samples in fully organic solvents such as the assembly of P3HT nanowires in both toluene and ortho-chlorobenzene.[58] Through combination of cryoTEM, cryo electron tomography (cryoET), and low-dose electron diffraction, ordered nanowires were reported to form in both solvents as result of pi-pi stacking. However, the specific ordering of the nanowires was solvent dependent and determined the final morphology.

Self-Assembly Mechanisms

Vitrification is extremely beneficial for trapping and imaging transient species, enabling time resolved studies of molecular self-assembly. All self-assembly mechanisms involve transient intermediates, which are typically solvated and disordered.[56] A study investigated the mechanism of crystalline arrays formed from perylene diimide amphiphiles.[86] It was observed that the system

initially formed amorphous aggregates that later crystallized into arrays. CryoTEM also provided insight into the organization of the transient precursors, which would have been impossible to observe using other characterization methods.[56] To better understand the formation of nanotubes from chiral amphiphiles, a study monitored the chiral self-assembly of $C_{12}\beta_{12}$ using cryoTEM.[87] Throughout the study, cryoTEM revealed various intermediates including fibrils, twisted ribbons, and helical ribbons where the ribbons were found to widen over time and form nanotubes. Overall, the study established a new mechanism for nanotube formation and emphasized the importance of chirality throughout the assembly process. CryoTEM has also been used to study poly(ethylene oxide)-b-poly(octadecyl methacrylate) self-assembly into bicontinuous polymer nanoparticles.[88] Throughout the experiment, various morphologies such as vesicles, worms, and spheres were reported as a result of altering water/tetrahydrofuran ratios and temperature (Figure 3iv). Another study found that by altering the pH, a vesicle could exhibit “breathing” characteristics due to the volume of the vesicle being reversible.[89] In addition, the size and the thickness of the polymeric layers were observed to change as a function of pH. Freeze-fracture-replication cryoTEM can also serve as an important technique when imaging intermediate species of complex liquid samples such as those that are highly viscous or consist of large assembled structures. [60] This technique proved to be useful when monitoring the assembly of a mesoporous material, SBA-15. [90] Throughout the time-resolved study, the initial sample with low viscosity was observed to have micelles which later evolved into a highly viscous solution with the arrangement of a crystalline hexagonal phase.

The disadvantage of cryoTEM to study self-assembly mechanisms is that the history or future of any individual particle is unknown. This means that the series of images which the user selects to represent the mechanisms can be subjective; the user must decide which particle is most representative of the time point. This is not a challenge for relatively simple processes, but for complex processes that contain multiple types or structure or mechanistic pathways, the

confidence with which the user can assemble the series of representative images is reduced. This challenge can be addressed by the application of liquid phase TEM.

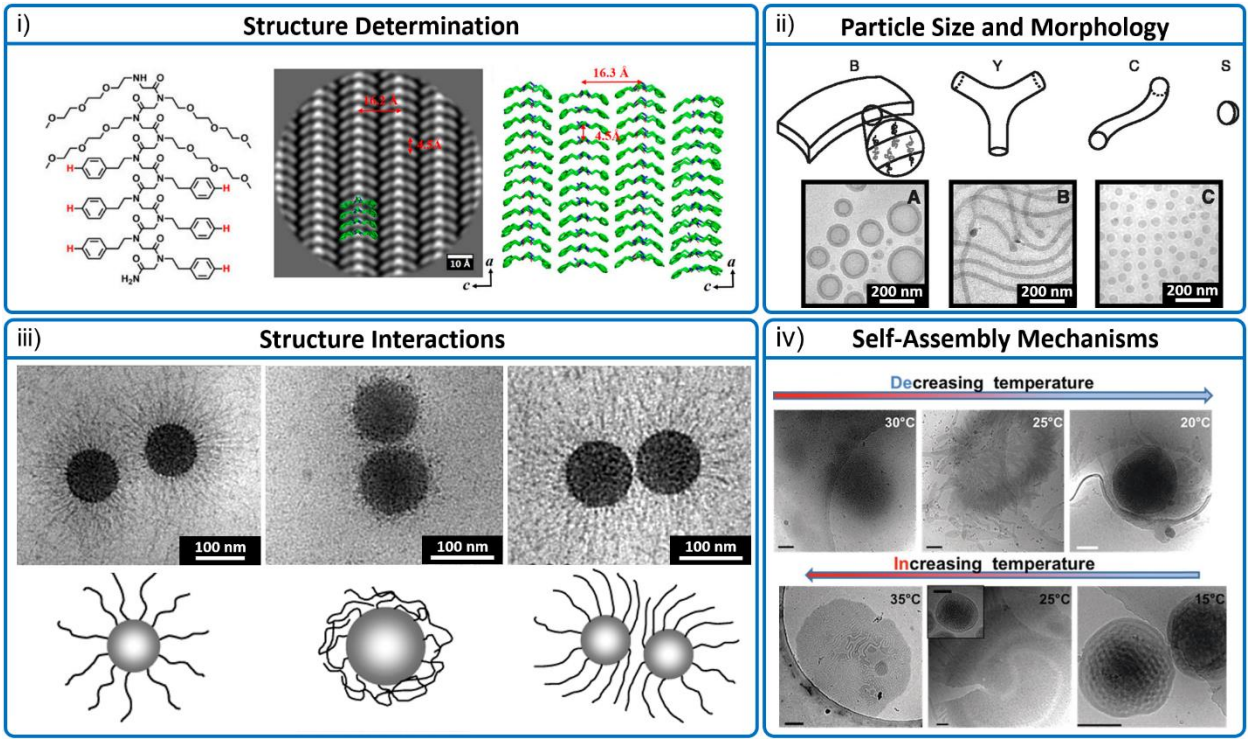

Figure 3: An overview of cryoTEM being used to understand molecular structure, nanoscale morphology, particle interactions and self-assembly mechanisms. **i)** CryoTEM imaging of polypetoid nanosheets with respective reconstructed molecular model. Reproduced with permission from ref ([73]). Copyright 2019 National Academy of Sciences. **ii)** Schematic and cryoTEM images of PB-PEO diblock polymers exhibiting bilayer, Y-junction, and cylinder morphologies. Reproduced with permission from ref ([83]). Copyright 2003 AAAS. **iii)** CryoTEM images of extended, collapsed, and repulsed conformations of polyelectrolyte chains as a result of structural interactions with other particles or with solution. Reproduced with permission from ref ([85]). Copyright 2005 American Chemical Society. **iv)** Self-assembly mechanisms of bicontinuous polymeric nanospheres as a result of decreasing and increasing temperature (scalebar = 200 nm). Reproduced with permission from ([88]). Copyright 2016 Royal Society of Chemistry.

3.3 Liquid phase TEM

Liquid phase TEM (LPTEM) enables dynamic processes to be observed in real-time while in the liquid state, making it an ideal platform for studying self-assembly mechanisms.[91,92] Although the first LPTEM experiments were attempted in the 1930's,[93] modern LPTEM is still early in its development. Several challenges need to be addressed related to sample preparation methods (section 7.2), control of particle confinement within the cell,[94] quantification of electron-sample interactions (section 7.4), and development of efficient movie analysis methods (section 7.5).[95–97] Sample preparation is challenging as experiments are difficult to reproduce, hindering the collection of large numbers of experimental datasets. Confinement within the ~100-1000 nm thick liquid cells limits the data to visualization of processes at a solid-liquid interface. The surface interactions can significantly affect particle dynamics, resulting in anomalous diffusion behavior.[98] All liquids are beam sensitive, and the electron-liquid interactions can significantly affect the observations made (section 7.4).[99] Furthermore, LPTEM data is typically very large and collected at the limit of signal to noise (section 7.4). Despite these challenges, LPTEM has been used to study block copolymers,[100–104] homopolymers,[101,102,105,106] peptides,[107] proteins,[108–111] covalent-organic frameworks,[112] metal-organic frameworks,[99,113] nucleic acids,[114] and lipids.[115,116]

Several methods can be used to initiate self-assembly inside the liquid cell, including induction from the electron beam,[101] heating,[103,117] and solvent mixing.[100,118,119] LPTEM has been used to study the formation and evolution of block copolymer micelles.[102,104] In two separate papers, the processes of micelle fusion and unimer addition were found to occur simultaneously.[102–104] In the case of the norbornene-based polymers, which are known to form kinetically trapped assemblies,[120] the LPTEM data revealed that micelle fusion resulted in the formation of micelles with internal water pockets.[102] Fusion is a complex process that is extremely challenging to study by scattering or ex-situ methods. LPTEM enables the determination of fusion relaxation times

(Figure 4i,ii), particle collision frequency, and the fraction of collisions which result in a successful fusion event.[102]

Self-assembly mechanisms involving multiple phase changes are complex and require real-time imaging. For example, protein crystallization can proceed via liquid or amorphous precursor phases,[121] but the mechanistic details of how one phase converts into another are largely unknown. LPTEM observations of lysosome crystallization enabled the discovery of a new crystallization pathway.[111] (Figure 4 iii) Lysozyme crystals were observed nucleating at the surface of amorphous solid precursor particles. Previously, these types of precursors were not known to act as heterogeneous nucleation sites for crystallization. In addition to this new pathway, nucleation was observed to occur from within a separate liquid-like precursor particle. The study observed multiple crystallization pathways in the same system, which would have not been possible using other analytical methods. LPTEM has also been able to visualize single strand DNA helix formation (Figure 4 iv).[114] During the double stranded helix formation, the DNA molecules were observed to form transient loops which were corrected for error as the formation proceeded. Furthermore, the study also observed in the “melting” of DNA assemblies when a third DNA strand was in contact the double stranded helix, such behavior has large implication in DNA based technologies in precision medicine and DNA-controlled colloidal assembly.

Vesicle formation is one of the most well studied molecular self-assembly mechanisms.[122,123] Prior to LPTEM studies, extensive research had concluded that amphiphilic molecules could form vesicles by two different pathways, known as Pathway I and II.[124] Both pathways begin with the formation of spherical micelles, which evolve to form vesicles via an anisotropic (Pathway I) or isotropic (Pathway II) intermediate structure. Pathway 1 is reported to occur for high concentrations and low molecular weight amphiphiles with weak interaction parameters.[125,126] Direct observation of the vesicle formation using LPTEM revealed a two-step process.[100] Amphiphiles first undergo liquid-liquid phase separation to form droplets and then organize into

vesicles at the interface between the droplets and the bulk solution (Figure 15iv). Importantly, by changing the temporal resolution with which the assembly process is visualized, features of either Pathway I or II, could be observed. This observation reveals that within a single particle, multiple pathways can occur over the same time period, but with different temporal dynamics.

Although relatively few molecular assembly processes have been studied by LPTEM, a general feature emerging from that data is that multiple pathways are common. This level of complexity is not typically discussed in the molecular assembly literature but must be embraced if complex processes are to be understood and controlled. For dynamic mechanistic studies chemist have traditionally used spectroscopy techniques such as nuclear magnetic resonance (NMR), infrared, and Raman spectroscopy. However, these instruments are limited in that they provide an ensemble average information of the molecular interactions. While LPTEM can distinguish multiple pathways and observe rare but important events during the nanoscale material formation. For example, it was discovered that the nucleation of primary particles during crystallization by particle attachment occurs in proximity of preformed nanoparticles. This explains the self-similar morphology of branched nanoparticles. The determination of this mechanism was only possible via the real-time visualization of the crystallization process.[127] Continued development of LPTEM is required to improve our understanding of complex self-assembly processes. This includes improving and automating sample preparation,[118] improving control over the environment inside the cells,[128] improving our understanding of electron-sample interactions in liquids,[129] and automating data analysis.[130] In addition, the combined use of cryoTEM and LPTEM will be essential. CryoTEM is the ideal method to obtained high resolution images of transient intermediates, while LPTEM is ideal for understanding the kinetics mechanisms that connect these intermediates.

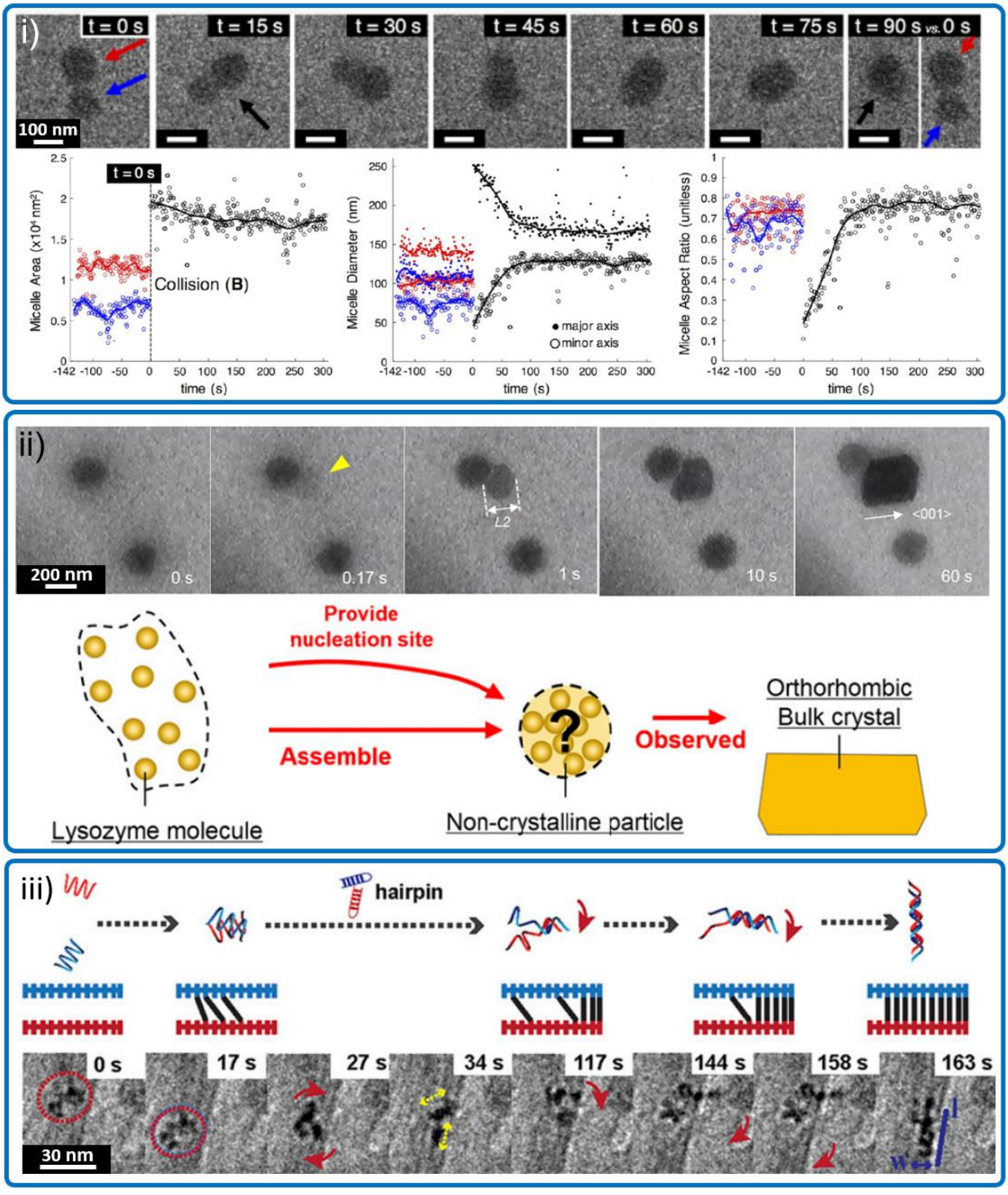

Figure 4: LPTEM observations self-assembly processes. **i)** Direct visualization of block copolymers micelle fusion process, the relaxation times of the fusion process are plotted using the LPTEM data. Reproduced with permission from ref ([102]). Copyright 2017 American Chemical

Society. **ii)** Real-time visualization of lysosome crystallization via a liquid intermediate. Reproduced with permission from ref ([111]). Copyright 2017 National Academy of Sciences. **iv)** DNA molecule dynamics during helix formation visualized in real time using graphene liquid cell. Reproduced with permission from ref ([114]). Copyright 2020 National Academy of Sciences.

3.4 Electron diffraction and crystallography

TEM imaging is typically performed in real-space. However, by changing the power of the objective lens it is possible to project the back focal plane (section 7.1) onto the detector and collect reciprocal space information - a diffraction pattern.[131] This technique is analogous to X-ray diffraction, however, the strong interaction of electrons with matter enables the collection of diffraction data on individual nanoparticles. This is in contrast to X-ray diffraction which requires either bulk powders or single micron scale crystals.[132] In electron diffraction, the term “selected area diffraction” is often used because the user selects an area of the grid to collect the diffraction pattern using an aperture. Electron diffraction patterns are typically collected for crystalline materials to obtain information such as symmetry, lattice constants, and reflection intensities.[133] However, electron diffraction can also provide structural information on amorphous materials.[134] A benefit of electron diffraction over real-space imaging is that high resolution information can be obtained at much lower electron doses which allows data acquisition with minimal electron beam damage (section 7.4). This is because the electron-sample interaction events of many atoms are averaged to provide high signal to noise information when collecting diffracted electrons. The limitation is that the diffraction patterns contain no real-space information. Therefore, a combination of real-space imaging and electron diffraction is typically used to determine the nanoscale morphology and atomic scale structure. Like X-ray crystallography, crystal structures can be solved by collecting electron diffraction patterns of crystals at multiple projection angles. This can be achieved by either imaging different particles with an identical crystal structures under

different orientations, or by collecting a tilt series of a single particle using electron beam tilt and goniometer rotation.

Numerous electron crystallography methods have been developed including Automated Diffraction Tomography (ADT)[135], Rotation Electron Diffraction (RED)[136,137] and Micro-Electron Diffraction (MicroED)[138,139,140,141]. Electron crystallography methods have been used to solve crystal structures for proteins[142,143], peptides, small molecules,[141] zeolities,[144] MOFs,[27,145] and COFs.[146] These structures are beam sensitive and collecting the data under cryogenic conditions is often ideal for preventing damage.[146] For example, using RED, the first single crystal COF structure was reported in 2013 (Figure 5 i) with a resolution of 1.5 Å. [147] The RED datasets were collected at both 298°K and 89°K and showed that cooling the sample reduced beam damage and enabled higher resolution reconstructions. MicroED has been used to determine atomic structures of mammalian prion protein nanocrystals (Figure 5 iii).[148] By merging diffraction data from multiple crystals, 0.75 Å resolution structures were solved which showed features that are critical to understanding structural stability and that were invisible in X-ray structure determination.[148] Host-guest interactions play an important role in the application of many MOF materials, and it is important to understand the location of binding sites within the MOF framework. Continuous RED was used to identify the positional of guest molecules in cobalt MOF Co-CAU-36 and identify all non-hydrogen framework positions from the structure solution (Figure 5 ii).[149] Future developments in the automation of electron crystallography data collection and analysis will result in a versatile tool for the analysis of crystalline assemblies.

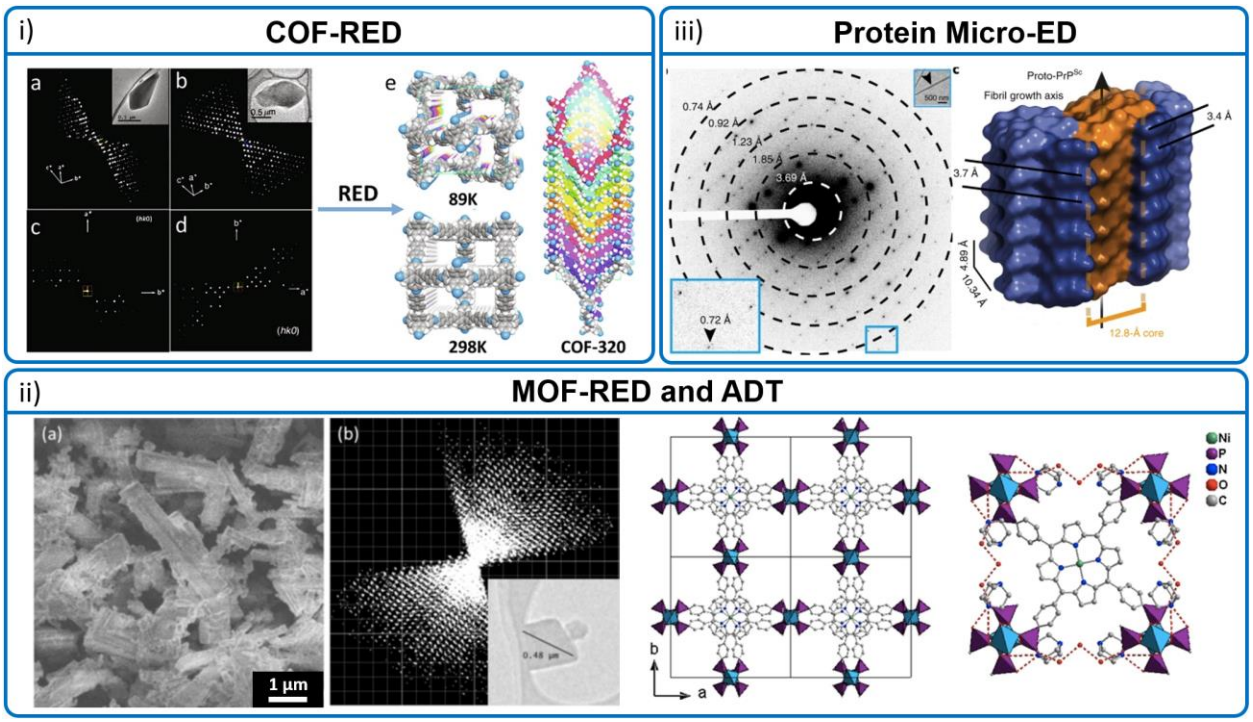

Figure 5: Electron diffraction to elucidate crystalline structures. i) Reconstructed reciprocal lattice of COF-320 from RED data at 298°K including models of COF-320 at different temperatures. Reproduced with permission from ref ([147]). Copyright 2013 American Chemical Society. ii) SEM image for Co-CAU-36. The crystals are generally rod-like, and the diameters of the rods are usually less than 1 µm. (b) Reconstructed 3D reciprocal lattice of Co-CAU-36 from cRED data processed using the REDp software (b, c) The framework structure of Co-CAU-36 viewed along [001] (b) and [010] (c). The inorganic building units consist of corner-sharing CoO_4 and PO_3. Reproduced with permission from ref ([149]). Copyright 2018 Wiley and Sons. iii) Single MicroED image showing strong diffraction to 0.72 Å (inset). A second inset shows a proto-PrP^{Sc} crystal probed by MicroED (arrow). Reproduced with permission from ref ([148]). Copyright 2018 Springer Nature.

3.5 Electron tomography and single particle analysis

TEM images are 2D projections of 3D structures; however, any 3D structure can be fully reconstructed from an infinite number of 2D projections.[150] This fundamental principle has been applied in TEM to obtain 3D reconstructions by two methods: single particle analysis (SPA) and electron tomography (ET). Single particle analysis refers to a suit of methods developed in the structural biology community to obtain atomic resolution reconstructions of biomolecules by imaging a large number of identical copies.[151–153] TEM images of organic and beam sensitive materials are often recorded with low signal to noise. Aligning and summing several images of individual objects with an identical protection angle can provide high resolution structural information not visible in any single particle – 2D class averaging. Imaging many different particles under many different orientations enables collection of all required orientations for 3D reconstruction.[154] Single particle analysis has been mostly used in conjunction with cryoTEM (section 3.2) and has become a dominant method for solving protein structures. CryoTEM is preferred because the vitrification process preserves the native structure of the assemblies and reduces electron beam damage (Figure 6 i, section 7.4).[155] The method has also been used to obtain 3D reconstructions of self-assembled structures made from DNA,[24,156–158] dendronized polymers,[155] and dendro-calixarene micelles.[152] Figure 6 ii shows the 2D projection images and resulting 3D reconstructions of DNA tetrahedra, dodecahedra, buckeyballs, and icosahedra,[159,160] as well as the helical assembly of the dendronized polymers.[155]

In contrast to single particle analysis, electron tomography enables the 3D reconstruction of a single unique object, which is necessary for the analysis of samples containing particles with structural variations.[161–165] Electron tomography works by taking several images of a single object at different angles, accomplished by tilting the sample inside the microscope. Compared to single particle analysis, electron tomography typically results in lower resolution reconstructions due to the reduced number of projections which can be collected.[166] The main physical limitation of

electron tomography is imposed by the stage and sample holder which typically restrict the tilt angles +/- 70º. This results in a wedge shaped region of missing information in Fourier space commonly called the “missing-wedge”.[167] To overcome this distortion, tilt acquisition schemes such as dual-axis tomography[168] are utilized to improve the reconstruction, and cylindrical specimens can be prepared that allow for full rotation and complete elimination of the “missing-wedge” problem.[169] For beam sensitive materials, the resolution of electron tomography is typically dose limited (section 7.4). Thus, electron tomography of molecular assemblies requires low dose imaging procedures and sensitive cameras, such as direct electron detectors.[166] In addition, electron tomography is often performed with cryoTEM to prevent drying-induced changes and minimize beam damage.

Electron Tomography is commonly used to provide 3D reconstructions of proteins[170], peptides[171], DNA[23], block copolymers,[172–176] dendrimers,[175,177–179] polymeric materials for membranes,[128,180–182] and organic solar cells.[183,58] For assemblies with structural complexity, electron tomography is essential for understanding the relationships between assembly parameters such as polymer structure, solvent composition, temperature, and internal structural features such as pore size and connectivity (Figure 6 iii-iv).[184–186] For example, cryo electron tomography (cryoET) has been used to determine the complex internal structure formed from the assembly of amphiphilic double-comb diblock copolymers.[187] The cryoET data revealed the internal structure is composed of an interpenetrating network of bicontinuous structures where hydrophobic segments are separated by channels containing the hydrated polymer.[187] In the case of triblock copolymers, cryoET was used to show the assembled structure was a multicompartment micelle and also quantify the distribution of the different domains within the structure.[174] CryoET was also used to study 3D nanoparticle architectures of DNA tubules with gold nanoparticles attached.[188] The images revealed that the DNA tubules have left-handed chirality, this was explained by the tendency of right-handed DNA helices to organize into left-handed supercoils upon assembly. Electron

tomography has also been used to determine defects in vesicular hexesomes of block copolymers.[189]

Despite the overwhelming success of single particle analysis, electron tomography continues to be essential for capturing 3D structures of molecular self-assemblies due to their structural heterogeneity. A promising development in electron tomography is so-called “Brownian Tomography”. This method involves using LPTEM (section 3.3) and the imaging of structures as they rotate in solution.[190–192] Like cryoET, this method does not require dehydration but has potential advantages over cryoET. First, it overcomes the stage rotation limitation and, therefore, removes the missing-wedge artefacts. Second, it allows data acquisition in a period of seconds (compared to minutes and hours for cryoET).[193] Brownian tomography has many challenges including the development of sample preparation methods where particle rotation is controlled, and also quantifying electron-sample interactions. However, continued development of this method could enable self-assembly mechanisms of unique 3D objects to be studied with nanometer or even atomic resolution.

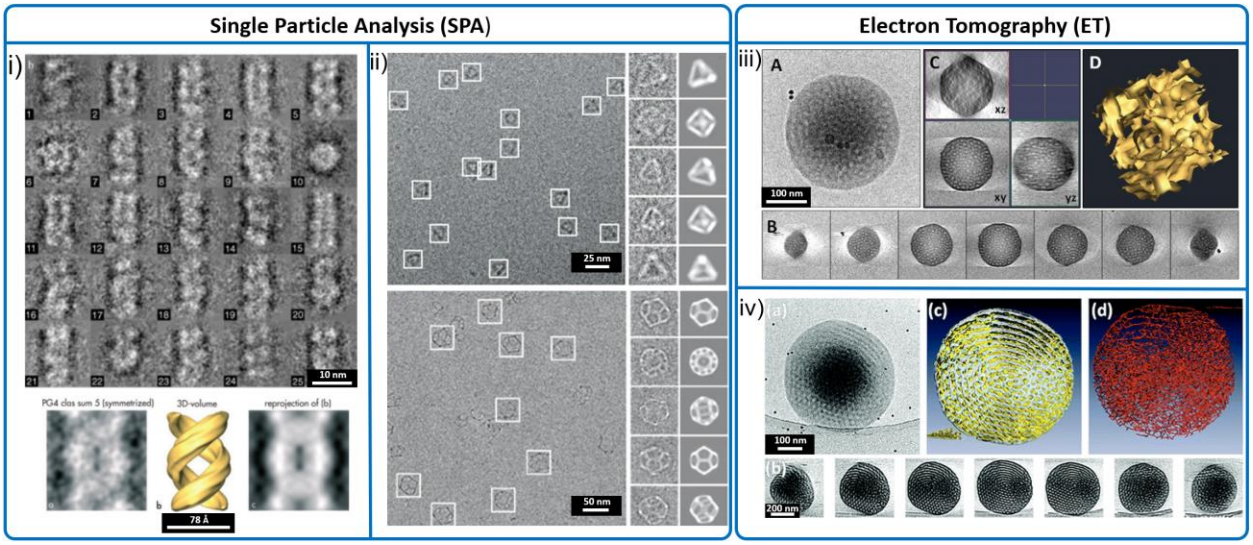

Figure 6: Single particle analysis and tomographic analysis of self-assembled structures. **i)** Class sum images obtained from different fiber motifs along with the 3D volume reconstruction of the

fibers. Reproduced with permission from ref ([155]). Copyright 2015 Wiley and Sons. **ii)** A representative cryoTEM image where the white boxes indicate the DNA particles. The side panel represents the raw cryoTEM images of individual particles and the corresponding projections of the DNA tetrahedron 3D structure reconstructed from the cryoTEM images. Reproduced with permission from ref ([159]). Copyright 2008 Springer Nature. **iii)** Analysis of a PB2 (PEO52-b-PBMA86) aggregate: (A) cryoTEM image of a bicontinuous nanosphere, showing the internal phase separation; (B) gallery of z slices showing different cross sections of a 3D SIRT reconstruction of a tomographic series recorded from the vitrified film in part A; (C) the xy, xz, and yz slices from the center of the aggregate; (D) computer generated isosurface of a segmented volume made from the aggregate shown in part A (the yellow represents the surface between the two phases). Scale bars represent 100 nm. Reproduced with permission from ref ([185]). Copyright 2013 American Chemical Society. **iv)** EM analysis of PEO_{39}-*b*-$PODMA_{17}$ aggregates: (a) cryoTEM image of a vitrified film at 4 °C; (b) gallery of *z* slices showing different cross sections of a 3D SIRT reconstruction of a tomographic series recorded from the vitrified film in (a); (c) computer-generated 3D visualization showing only an inner section of the whole structure, where all the channels and compartments are visible (the yellow surface is outside of the polymer, the surface in contact with the water); (d) skeletonization of (c), showing only a small section emphasizing that the structure is interconnected and therefore bicontinuous. Reproduced with permission from ref ([186]). Copyright 2010 American Chemical Society.

3.6 Analytical TEM

Analytical TEM refers to the chemical mapping of the specimen via signals generated from inelastic scattering of electrons. The most common methods for chemical mapping are energy dispersive X-ray spectroscopy (EDX) and electron energy loss spectroscopy (EELS).[194,195] These methods are commonly performed in STEM mode which enables chemical information to be obtained for each pixel in the image (Section 7.3). EDX is a well-established method that provides the elemental composition of a sample by measuring the characteristic wavelengths of X-rays emitted after inner-shell electron ejection caused by the electron beam and high energy electron relaxation.[196] EELS is a more recent development that measures the characteristic energy loss from electron-sample interactions that include plasmon excitations, inner shell ionization, and excited state transitions.[194] EELS provides elemental composition, bonding information, and enables vibrational spectroscopy to be performed at high resolution.[197] EDX and EELS are complementary in that EDX is typically used for thick samples made up of high atomic number elements, and EELS is used for thinner samples composed of low atomic number elements like carbon, nitrogen and oxygen.[198]

EDX and EELS are useful for multicomponent molecular self-assemblies that contain organic and inorganic components,[199] and for materials with phase separated molecules that contain different elemental compositions,[200,201] such as polymer nanoparticle composites which are used in catalysis, plasmonics, and diagnostics. For example, STEM and TEM were used to investigate the self-assembly of amphiphilic block-copolymers in the presence of iron oxide nanoparticles (Figure 7 iii).[202] The arrangement of the nanoparticles was examined by STEM-EDX to obtain Fe intensity line scans of the magneto core-shell structures. Quantifying the distribution of Fe aided the 3D interpretation of the 2D projection images and enabled the authors to conclude that they had assembled at least four different types of composite structures.

Functionalized-induced self-assembly is a nanoparticle synthesis method that involves the modification of a soluble block copolymer to induce self-assembly. In one example with trifluorophenyl functional group as the solvophobic block as the functional handle, enabled elemental mapping of the solvophobic blocks within the self-assembled structures.[201] The introduction of fluorine was deliberate for probing the functionalization as other atoms (carbon, oxygen, and hydrogen) are abundant in all parts of the self-assembled structures. Additionally, a combination of STEM-EDX and STEM-EELS has been used to investigate post synthetic exchange methods in the synthesis of metal-organic frameworks as seen in Figure 7 i.[203] This study discovered the formation of a metal oxide shell on the MOF surface rather than previously reported post synthetic exchange of metal atoms through the MOF crystal.

Combined STEM-EELS and bright field TEM has been used to determine the morphology and chemical composition of self-assembled gold nanoparticles on the surface of boron nitride nanotubes (Figure 7 ii).[204] STEM-EELS was used to measure the sp^2 hybridization characteristics on graphene by utilizing the electron beam to produce transitions in the sample from the internal energy level 1s to unoccupied higher energy states. This analysis makes it possible to know the degree of C-C bonds to C-H bond conversion by quantifying the sp^2 hybridization.[205] In the composite graphene/polymer field, EELS has been used as a mapping tool to determine the distribution of polyaniline on the surface of individual graphene polyaniline sheets.[206] Elemental mapping has also been used in the case of GaN@ZIF-8 a to show a uniform background of ZIF-8 with small Ga NPs embedded throughout the crystal.[207] One of the main challenges with EELS and EDX is beam damage and sample drift from the long exposure times required for obtaining high signal to noise spectra. However, recent techniques such as “aloof” EELS provide damage free methods to obtain chemical information.[208] We expect such methods will increase the use of elemental mapping for the study of self-assembled materials. This will be an important step

forward in connecting molecular chemistry with the emerging nanoscale structure that occurring during molecular self-assembly.

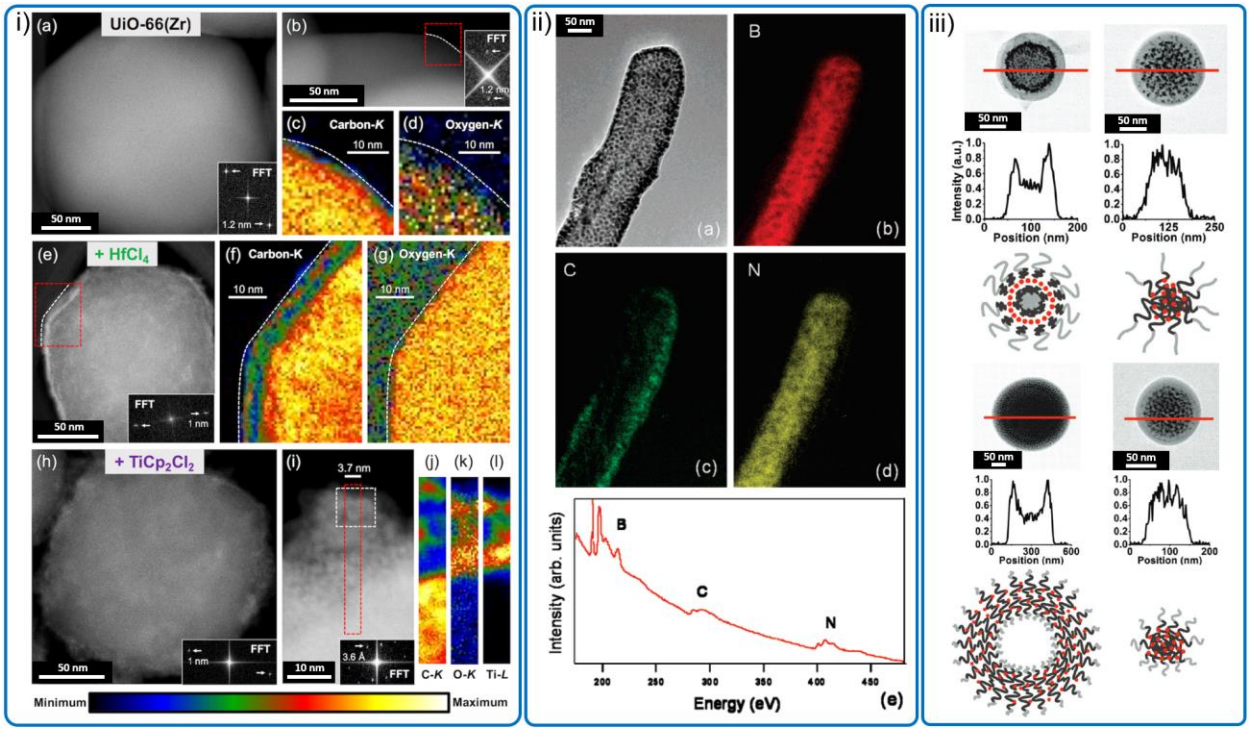

Figure 7: Analytical TEM used to understand molecular organization within self-assembled structures. **i)** STEM-EELS characterization of UiO-66(Zr) MOFs. STEM-EELS elemental maps display the placement of carbon and oxygen within the MOF structure. Reproduced with permission from ref ([203]). Copyright 2018 American Chemical Society. **ii)** (a) Bright-field TEM image of DMAP−Au nanoparticles self-assembled at the surface of MPA-BNNTs, (b) elemental mapping of B present in part a, (c) elemental mapping of C present in part a, (d) elemental mapping of N present in part a, and (e) EEL spectrum of materials in (a). Reproduced with permission from ref ([204]). Copyright 2007 American Chemical Society. **iii)** Structural characterization of 3 different self-assembled structures by changing solvent ratios. Reproduced with permission from ref ([202]). Copyright 2011 American Chemical Society.

3.7 4D-STEM

4-dimensional scanning transmission electron microscopy (4D-STEM) is a scanning-probe electron diffraction technique (see section 3.4) in which a converged electron beam scans across the sample generating a 2D image where each pixel contains a 2D diffraction pattern, resulting in a 4D dataset.[209,210] This technique can be used to obtain a wide range of structural information including nanoscale variation in crystal orientation,[211] structural order,[212] grain boundaries,[213] and material phase.[214,215] For example, it is possible to produce an orientation map of a specific region within a sample by assigning each pixel of the raster scan to a crystalline orientation based on the directionality and features in each diffraction pattern (Figure 8 i). 4D- STEM has been used to study polymers[216–218], biomolecules[211,219], and porous frameworks.[214,220] One benefit of 4D-STEM is the ability to finely control electron flux and cumulative dose through careful selection of electron current, probe size, probe dwell time, and inter-probe position distance.[221] Beam-sensitive materials are typically prepared in the vitreous state[222] or imaged at cryogenic temperatures to reduce electron beam damage and improve the signal to noise of Bragg's reflections.[223]

4D-STEM has been applied to soft matter primarily to probe local nanoscale variation in lattice orientation or defects, in contrast to bulk scattering techniques which look at ensemble structure. For example, 4D-STEM was used to quantify the size and orientation of crystalline domains before and after annealing an organic semiconductor thin-film of poly[2,5-bis(3-tetradecylthiophen-2-yl)thieno[3,2-b]thiophene] (PBTTT).[224] Annealing is a common processing step that is used to improve organic semiconductor device performance by altering thin-film morphology. However, it has been challenging to directly visualize the structural effects of annealing on complex polycrystalline materials. Here, pi-pi stacking along the polymer backbone in the film resulted in directional diffraction peaks, which made it possible to determine the real-space polymer orientation at each probe location with nanoscale spatial resolution (Figure 8 i).

The study showed a transition from small (nm), randomly oriented domains to larger mesoscale domains, which directly corresponds to improvements in charge transport properties. 4D-STEM has also been used to characterize nanoscale lattice variation within single peptide crystals.[211] The electron beam was scanned across a 3 um x 3 um area with a converged spot size of approximately 6 nm and an inter-probe distance of 20 nm. The resulting diffraction patterns were indexed with unsupervised classification using a library of simulated patterns to produce a 2D orientation map of the scan area, providing nanoscale domain information. (Figure 8 ii). 4D-STEM was also used to locate and characterize defect nano-domains in a UiO-66 MOF system.[214] Diffraction analysis was able to distinguish between the fcu and reo phases, and suggested a "blocky lamellar" morphology of the nano-domains, which form preferentially in specific orientations (Figure 8 iii). This study provided new information for defect cluster modeling and demonstrated the effectiveness of 4D-STEM studies for defect engineering.

The two main challenges for 4D-STEM experiments are data collection speed and data interpretation. The scan speed of a 4D-STEM experiment is typically limited by the framerate of the detector because each probe location requires the collection of a diffraction pattern. Slow scan speeds can result in imaging artifacts because thermal fluctuations during imaging can cause significant sample drift.[221] However, progress has been made by the recent adoption of direct electron detectors which are ideal for rapidly collecting diffraction patterns,[225] with some detectors achieving framerates of 87,000 frames per second (11 microseconds per frame).[226] Another significant challenge is user-friendly data analysis and visualization to enable non-experts to interpret datasets. Several python packages[209,227] and a growing body of methodology literature is addressing this challenge, including efficient processing pipelines which rapidly provide user feedback on data quality.[228] As the hardware and software for 4D- STEM continues to improve, we expect this technique to become a standard method for characterizing molecular self-assembly.

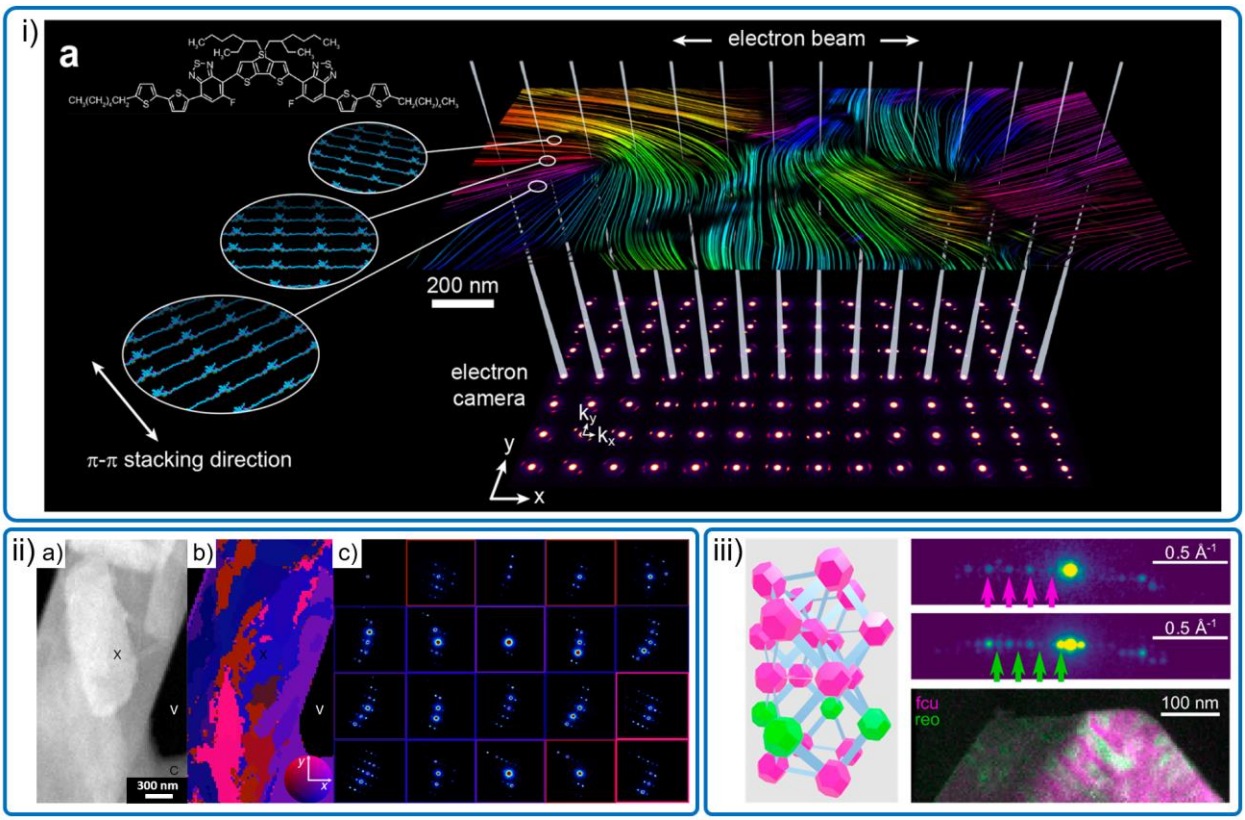

Figure 8: 4D-STEM analysis of self-assembled materials. **i)** Orientation map of thin-film PBTTT, where colored lined represent the direction along the conjugated backbone. The direction of the pi-pi stacking can be determined by the directionality of the diffraction pattern, which can then be used to determine the polymer orientation. Reproduced with permission from ref ([221]). Copyright 2021 American Chemical Society. **ii)** (a) HAADF image of peptide nanocrystal and (b) nanocrystal orientation map generated by unsupervised classification of diffraction patterns. (c) average diffraction patterns shown in (b), with box outline color denoting the region. Reproduced with permission from ref ([211]). Copyright 2019 Springer Nature. **iii)** 4D-STEM analysis of defect nanodomains in the UiO-66 MOF system. Magenta is used to denote the fcu phase while green is used to denote the reo defect phase, with representative diffraction patterns shown. Reproduced with permission from ref ([214]). Copyright 2021 American Chemical Society.

4. Combined and correlative methods

4.1 Scattering methods

Scattering techniques provide structural information by irradiating samples with radiation of known wavelength and measuring the scattered radiation as a function of angle and/or time. Scattering experiments commonly determine features of the sample such as: morphology, molecular weight, radius of gyration, hydrodynamic radius, particle interactions, and lattice constants. The choice of scattering technique is generally determined by the length scales of the probed structure, as scattering techniques perform best when the wavelength of the radiation is approximately equal to the size of the structures. The most common scattering techniques used in self-assembly studies are static and dynamic light scattering (SLS and DLS), wide and small angle X-ray scattering (WAXS/SAXS), and small angle neutron scattering (SANS). Scattering techniques provide ensemble information (typically >10^10 particles) and are particularly useful for studying self-assembly because the experiments can be performed in the native environment of the samples. Thus, a combination of TEM and scattering data can be used to address the statistics and environment challenges encountered with TEM (Section 2.1). In general, the scattering data is used to validate the TEM images. However, scattering data can also provide additional information or more accurate mean size values, which are not readily obtainable by TEM. The reader is directed to the following text for more information on light, X-ray, and neutron scattering.[229,230]

Light Scattering

DLS is commonly combined with TEM to provide evidence that the TEM images are representative of the ensemble by means of comparing the particle size distributions from both methods. Although DLS is an important validation, the user should be aware that, in the vast majority of cases, the particle size distributions by TEM and DLS will not look the same. DLS measures the fluctuations of light intensity due to the particle Brownian motion and allows the

determination of the diffusion coefficient (D), which relates to the hydrodynamic radius (R_h) of the particle through the stokes-Einstein equation.[231] The hydrodynamic radius is the theoretical radius of a hard sphere which moves with the same translational diffusion coefficient as the structures being measured. The value of R_h is not equal to the radius of the particle unless the particle is a perfect hard sphere. Furthermore, DLS provides z-weighted averages unlike TEM data which is typically used to calculate the number average. Therefore, samples with even a small amount of dispersity will have different particle radius values. Combined DLS/cryoTEM was used to study the assembly of block copolymers in ionic liquids.[232] This was one of the earliest cryoTEM studies on ionic liquids, and the authors noted the samples were sensitive to the electron beam, making the validation of the cryoTEM images with DLS even more important. DLS and cryoTEM were used to study the self-assembly of Janus cylinders with compartmentalized corona (Figure 9 i).[233] By combining the methods, the size of the cylinders could be determined with respect to sonication time. Unlike DLS which measures the intensity of scattered light at one angle, SLS experiments use multiple angles, and it can provide the radius of gyration, molecular weight, and the second virial coefficient. Although cryoTEM images can be used to calculate the aggregation number of micelle assemblies by assuming the density of the core is representative of the bulk polymer, SLS can be used to validate the cryoTEM images.[231] Combined DLD/SLS can be used get information about particle morphology, which is reflected by the R_g/R_h ratio.[234,231] Combined TEM, DLS and SLS was used to study poly(ferrocenyldimethylsilane)-b-poly-(dimethylsiloxane) micelles.[235] TEM revealed a cylindrical morphology, and DLS/SLS was employed to determine the molecular weight, R_H, and R_g, which concluded that the cylindrical micelles were very flexible in solution.

X-ray and Neutron Scattering

X-ray and Neutron Scattering have higher resolution than light scattering methods due to x-rays and neutrons having smaller wavelengths than photons. In addition to measuring molecular

weight, particle sizes and morphological information they can obtain details about the molecular level ordering of the assemblies.[236] SAXS, in particular, can characterize the evolution of nanoparticle morphologies and of particle/aggregate diameters. When evaluating the polymerization-induced self-assembly (PISA) of benzyl methacrolate (BzMA) in mineral oil, SAXS revealed new mechanistic insight into the vesicle formation by providing exact dimensions of the growing nanoparticles. [237] In addition, the kinetics of the BzMA polymerization could be observed using SAXS, but the data had to be normalized due to a faster rate being observed with SAXS compared to under normal laboratory conditions. TEM experiments were then combined with the SAXS experiments which enabled a phase diagram to be established to better understand the thermodynamics driving each morphology. Combined SAXS and cryoTEM was used to monitor the growth of micelle size and of amphiphilic block copolymers as a function of cosolvent removal.[238] In the SAXS experiments, they monitored the change in the position of the primary peak to give insight into the micelle size and compared these results to the calculated micelle size at different cosolvent concentrations (Figure 9 ii).[239] From these experiments, the free energy landscapes that govern the assembly mechanisms and, thus, the final micelle sizes could be determined as a function of cosolvent concentrations. WAXS can be used to measure structural features such as beta sheets and pi-stacking, and in combination with TEM, it can be used to link these structural features to the nanoscale morphologies (Figure 9 iii). [240, 241]

Although X-rays are much less damaging than high energy electrons at high enough fluxes, X-rays can still damage samples.[242] Small angle neutron scattering (SANS) has a larger penetration depth than X-rays and does not cause radiation damage. SANS experiments probe structures from nano- to micrometer resolution and are much more sensitive to light elements. In addition, contrast SANS can be utilized to monitor self-assembly formation by isotope labeling to gain a better understanding of organic and biological systems.[242,243] Combined cryoTEM/SANS were used to monitor the growth of the micelle core for polyelectrolyte block copolymers as a function

of the addition of salt concentration (Figure 9 iv).[244] The combined methods determined that while micelle parameters were not altered at low salt concentrations, high salt concentrations (>0.1 mol/L) altered the micelle structures due to an increase in the ionic strength of the solution. In addition, SANS was able to confirm corona phase separation resulting in a high density inner shell and low density outer shell. In a different study, four diblock copolymers were synthesized to form polymersomes and were evaluated using cryoTEM and SANS. [245] While SANS determined polymer packing behavior, cryoTEM was used to determine the shapes of the assembled structures. Both methods were also used to evaluate membrane thicknesses, which demonstrates that although thickness measurements can be obtained using both methods, the values will rarely be exact. The main challenge with combined TEM and scattering experiments is related to the extrapolation of single particle data to the ensemble average of any given system. This is discussed in more detail in the outlook.

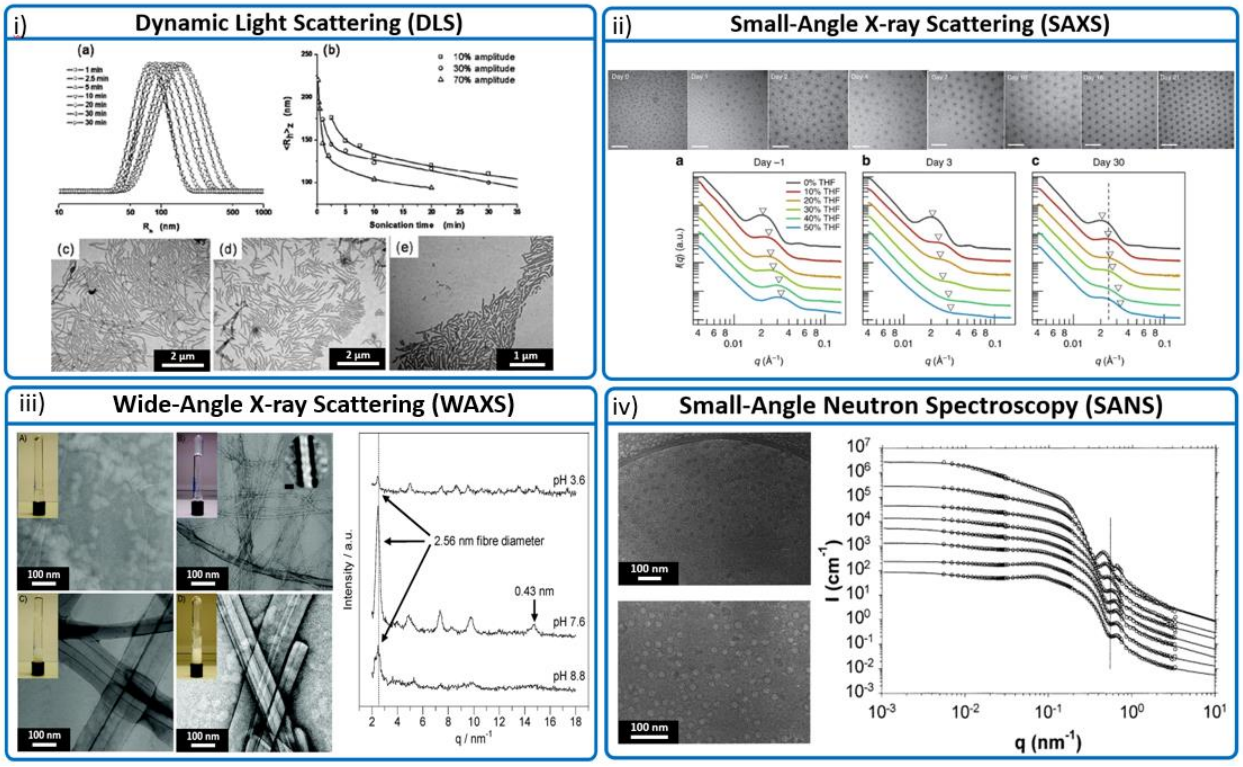

Figure 9: Examples of combined use of TEM and scattering techniques. **i)** DLS and TEM used to monitor the size evolution of Janus cylinders in response to sonication. Reproduced with permission from ref ([233]). Copyright 2009 American Chemical Society. **ii)** CryoTEM and SAXS used to monitor micelle size over a 30 day period. Reproduced with permission from ref ([238]). Copyright 2014 Springer Nature. **iii)** TEM and WAXS used to visualize and quantity the evolution of crystalline fibers at varying pH. Reproduced with permission from ref ([241]). Copyright 2009 American Chemical Society. **iv)** CryoTEM and SANS combined to visualize and quantify the effect of salt concentration to the micelles in solution. Reproduced with permission from ref ([244]). Copyright 2002 American Chemical Society.

4.2 Optical microscopy

The most common combined TEM/optical microscopy studies are performed with confocal scanning laser microscopy (CSLM) and polarized optical microscopy (POM). Optical microscopy can image a sample in its native environment and temporally resolve phenomena occurring in fields of view ranging from microns to millimeters. Materials can be differentiated based on their optical response rather than electron density, which can be an advantage when performing a combined TEM study. For more general information on optical microscopy, the reader is directed to the following texts.[246–252]

<u>Fluorescence Microscopy</u>

CSLM is a scanning technique which produces an image from the fluorescent response of a sample with an x,y resolution of ~250 nm and z resolution of ~550 nm.[253] CSLM is commonly combined with TEM to study the uptake and release of drugs (or fluorescent analogues) in MOFs[254,255], block copolymers[256], peptides[257], oligosaccharides[258], small molecules[259], and DNA[260]. Materials containing molecules with different excitation wavelengths can be distinguished and overlaying this information with TEM images provides complementary high spatial resolution

information. This is commonly done with fluorescent particles and fluorescently stained cell membranes (Figure 10 ii). [261,262] For example, fluorescein was used as a hydrophobic small molecule model for the anticancer drug camptothecin to demonstrate drug encapsulation and drug delivery in ZIF-8 MOFs.[261] TEM was used to determine ZIF-8 spherical morphology, narrow size distribution, and monitor structural stability in different pH environments, while fluorescent microscopy was used to determine MOF encapsulation effectiveness and fluorescein uptake in MCF-7 breast cancer cells. In another study, a peptide derivate was developed to selectively self-assemble in the presence of liver cancer cells.[263] Fluorescence microscopy revealed nanoparticle self-assembly in the presence of extracellular alkaline phosphatase (ALP) which then diffused into the cell where intracellular glutathione triggered gelation. TEM showed spherical nanoparticles present in the cell after 30 minutes and nanofibrils present in broken cells after 4 hours, confirming nanostructure transition.

Several CSLM/TEM studies have used fluorescent dyes such as Nile Red or BODIPY to distinguish the hydrophobic regions in vesicles[264–266] or dendrimersomes[267], while some studies have tracked self-assembly in systems which dynamically fluoresce upon micelle aggregation[268] or amphiphile gelation.[269] Other combined studies have researched self-assembly of fluorescent surfactants[25] and amphiphilic small molecules,[26] or have incorporated dyes into block copolymers to study cylindrical micelles[272] and colloidosomes.[273] For example, crystallization-driven self-assembly was used to sequentially add fluorescent micelle blocks to existing cylindrical micelles to produce unique and controllable fluorescent nanostructures.[274] TEM was used to determine the nanoscale morphology of the micelles while CLSM revealed the unique emission of each micelle block (Figure 10 i). Another study used fluorescently labeled amphiphiles which fluoresce upon self-association to track liquid-crystal defect driven self-assembly.[275] Fluorescence microscopy showed self-association only occurred in defects rather than liquid-crystal bulk, while TEM enabled the characterization of liquid-crystal nanostructure of the resulting assemblies.

Polarized Optical Microscopy

POM produces an image from the interaction of light with a sample placed between two perpendicular polarizers. Contrast is generated from birefringent materials, which are optically anisotropic and alter the phase of the light allowing it to pass through the second polarizer.[252] This is particularly usefully for studying macroscopically aligned materials such as liquid crystals[276–278], aligned hydro gels[279–281], and fibrils.[39,282,283] For example, nanoporous films were produced by first aligning liquid crystal via mechanical rotation in a magnetic field then photo-crosslinking the structure (Figure 10 iii).[284] Stained TEM revealed well-ordered hexagonally packed pores and uninterrupted nanochannels, while polarized optical microscopy confirmed this property in the bulk film which demonstrated optical extinction when channels were parallel or perpendicular to the polarizers (Figure 10 iii). Another study used POM to demonstrate macroscopically aligned domains of peptide-containing monodomain gels, and TEM to characterize nanoscale structure and fibril spacing. This information revealed a formation pathway for peptide-based structures in physiologically relevant conditions, which may be relevant for specific human diseases.[285]

One obvious challenge of combined or correlative TEM/CLSM studies is that non-fluorescent molecular assemblies cannot be imaged without incorporating dyes into the structure or fluorescently tagging the molecules. There are several methods of preparing fluorescently labelled nanoparticles,[286] but it must be considered that fluorescent labeling will affect the self-assembly behavior. In addition, the resolution discrepancy generally limits optical microscopy studies to micron scale structures, which can be challenging when trying to correlate the optical and TEM images. Several modern techniques such as structured illumination microscopy (SIM), stimulated emission depletion (STED), and single-molecule localization microscopy (SMLM) have improved optical microscopy resolutions well past the diffraction limit to a reported 5 nm[287] and

have been used to study lipids and DNA oragmi.[253,288] These advanced methods are ideal for future combined studies with optical microscopy and TEM.

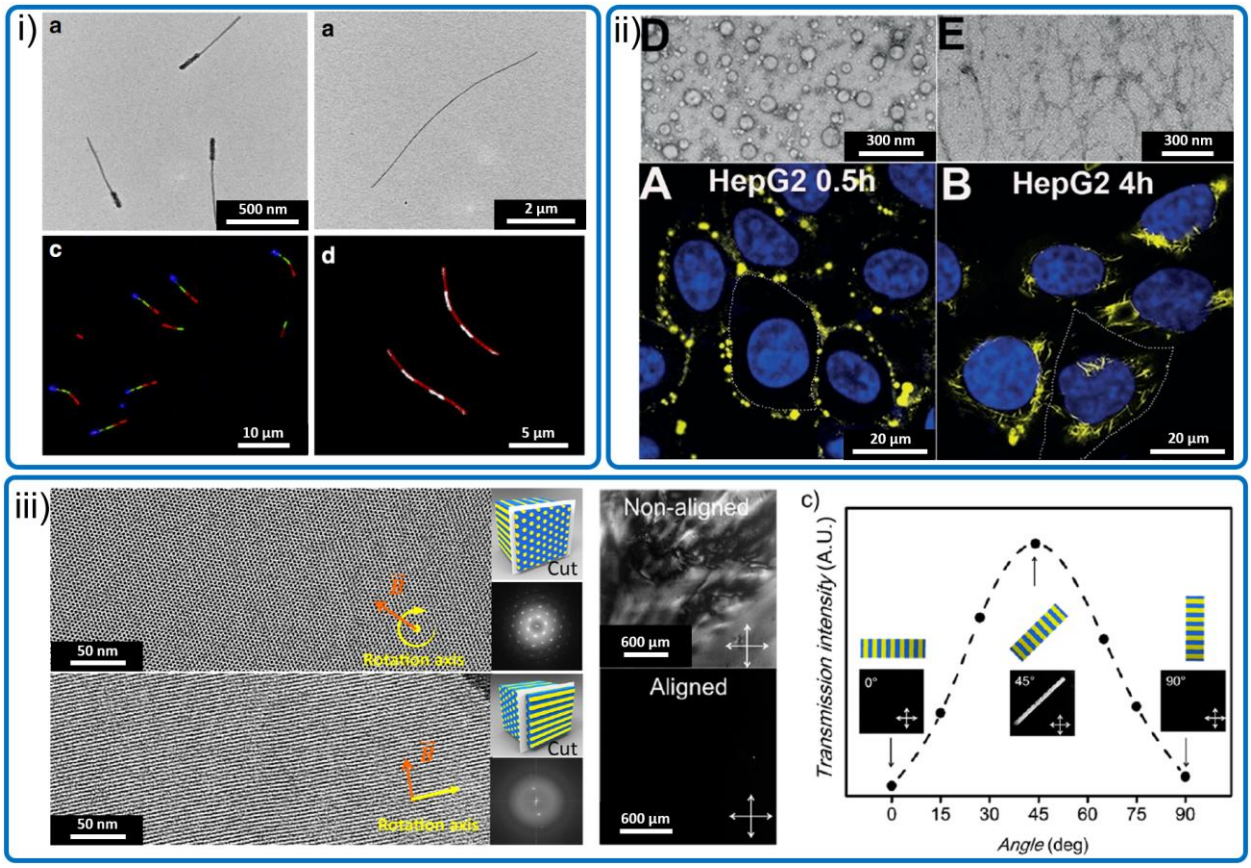

Figure 10: Examples of combined optical microscopy/TEM studies. i) TEM images and corresponding confocal fluorescence microscopy images of asymmetric triblock co-micelles with RGB nanopixels. Reproduced with permission from ref ([274]). Copyright 2014 Springer Nature. ii) TEM images and corresponding merged fluorescence microscopy images of cell culture medium after 30 minutes (left) and 4 hours (right) of incubation. Reproduced with permission from ref ([263]). Copyright 2018 Wiley and Sons. **iii)** (left) Stained TEM images of crosslinked liquid crystals perpendicular (top) or parallel (bottom) to the rotational axis, and corresponding FFT image. (center) Polarized optical microscopy image of nonaligned liquid crystal membrane (top) vs aligned membrane (bottom). (right) Transmission intensity of aligned film as a function of rotation

angle. When the aligned axis is parallel or perpendicular to the polarizer, optical extinction occurs. Reproduced with permission from ref ([284]). Copyright 2014 American Chemical Society.

4.3 Scanning electron microscopy

Scanning electron microscopy (SEM) uses a focused beam of electrons to scan across a sample surface and image surface topology, chemical composition, and crystalline structure. SEM typically operates with an acceleration voltage between 1-30 KeV (for comparison TEM is ~100-300 KeV) which results in a maximum resolution of approximately 1-5 nm.[289,290] Upon irradiation, elastic and inelastic scattering occurs which results in backscattered and secondary electrons. Backscattered electron detection provides is strongly dependent on atomic number and provides compositional information, while the secondary electron detection provides topography information.[291] Soft materials are often difficult to image due to low contrast, beam damage, charge accumulation, and sensitivity to vacuum.[292,293] Sample preparation techniques such as sputter coating,[291,294] cryoSEM,[295] and environmental SEM (ESEM)[296] are often used to minimize these effects for various types of samples. For more information on SEM and polymer sample preparation the reader is directed to the following texts.[291,297–299] The key advantage of SEM is the ability to image features of the samples surfaces that are unavailable with conventional TEM and are extremely difficult to obtain with electron tomography.[300,301] The combination of TEM and SEM provides high resolution information of both the internal structure and surface morphology.

SEM and TEM are often combined to study the self-assembly and stimulus response of supramolecular gels for applications in drug delivery[302–305], tissue-engineering[306–310], and light harvesting[311–313]. For example, combined cryoTEM/cryoSEM was used to study the reversible gelation properties of perylene diimide based system.[314] CryoTEM was used to estimate fiber thickness and characterize the crystalline structure of the gel, which is clearly evident in the FFT image (Figure 11 ii). SEM revealed a 3D nanoporous gel with large domains of “whirls” and “microstreams” and tracked a thermally driven shrinkage of the network. In another example, graphitic carbon nitride was incorporated into a peptide hydrogel during the self-assembly process to hybridize the fibrils and increase photoactivity for biomimetic photosynthesis.[311] SEM revealed

the fiber thickness and density increased with the graphitic carbon nitride ratio, while TEM showed the peptide nanofibers were well hybridized by the graphitic carbon nitride.

MOF crystals are often studied with both SEM and TEM to relate surface morphology to internal structure for application in molecular encapsulation, catalysis, and more (section 5.3).[25,315] Early MOF studies demonstrated small molecule confinement, but producing MOF crystals with pores suitable for large molecules was challenging.[316,317] A combined SEM/TEM study was used to characterize the first large-aperture pore MOF.[318] The pores on the MOF were imaged using SEM, while TEM was able to quantify the pore size and show continuous hexagonally packed channels throughout the bulk of the material (Figure 11 i). SEM is commonly used to study growth kinetics by imaging at different times during MOF formation.[319,320] For example, lanthanide-doped up conversion nanoparticles were incorporated into a MOF structure during self-assembly.[199] Time-resolved SEM images characterized growth kinetics of the composite formation, and then STEM, EDX analysis, and TEM tomography revealed the particles were only incorporated at the sample surface (Figure 11 iii). A second MOF layer was grown epitaxially and confined the nanoparticles for applications in anticounterfeiting and luminescence-monitored drug delivery. Nonionic block copolymer coacervates have been used to prepare self-assembled structures that range from nanometers up to millimeters in size.[301] To cover the entire size range, a combination of SEM and cryoTEM was used. The combined study revealed that the coacervate size determined the size of the final self-assembled structure.

Combined TEM/SEM studies can be challenging due to the difference in sample preparation. For example, sputter coating a sample in conductive material can add several nanometers of thickness to features.[291] Furthermore, TEM and SEM operate at significantly different accelerating voltages. Therefore, the beam-sample interaction needs to be understood and minimized under both conditions (section 7.4). Furthermore, resolution discrepancy can make it difficult to correlate features; however, this can also be a strength for performing multi-scale analysis.

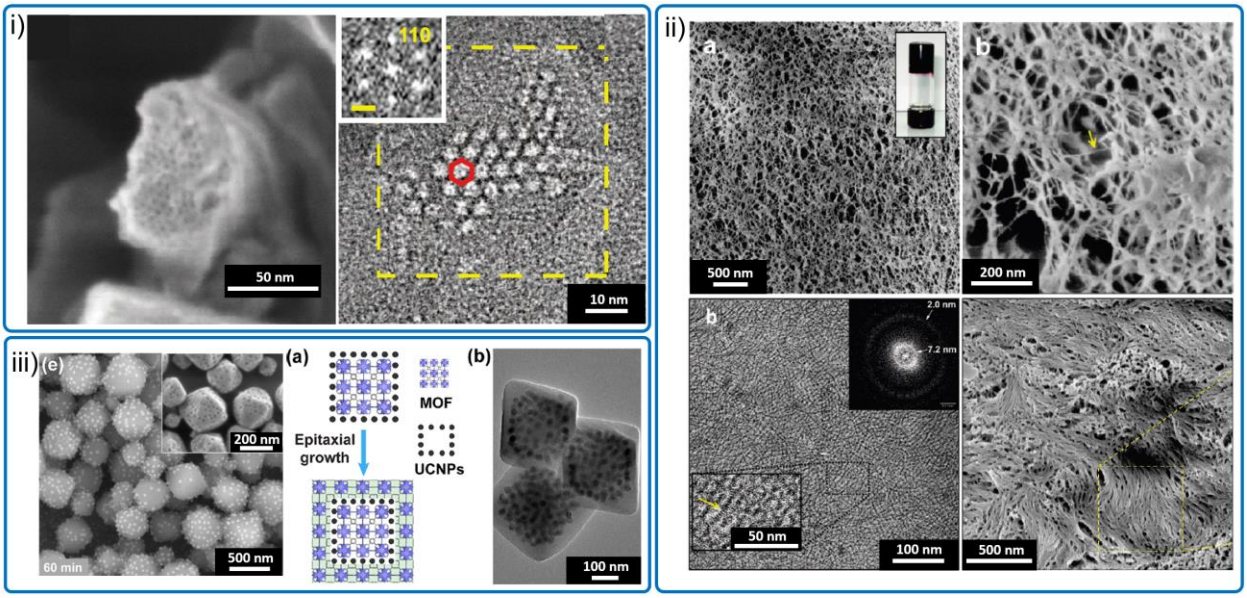

Figure 11: Example of combined SEM/TEM studies. **i)** SEM and TEM image of a large aperture MOF. The inset shows the FFT diffraction pattern. Inset scalebar .2 nm^{-1}. Reproduced with permission from ref ([318]). Copyright 2012 AAAS. **ii)** (top) SEM image of PP2b showing 3D porous network of nanofibers. (bottom left) TEM image of PP2b aggregated solution with FFT inset showing fibrous structures with uniform spacing. (bottom right) SEM image of thermally shrunken gel. Reproduced with permission from ref ([314]). Copyright 2009 American Chemical Society. **iii)** SEM image of intermediate stages of MOF nanocomposite formation after 60 minutes with inset showing MOF after hydrochloric acid treatment. (center) Schematic illustration of the epitaxial growth of another MOF layer on the MOF nanocomposites. (right) TEM images of MOF nanocomposites showing sandwiched nanocomposite layer. Reproduced with permission from ref ([199]). Copyright 2018 American Chemical Society.

4.4 Atomic force microscopy

Atomic force microscopy (AFM) is a scanning probe technique that generates an image through the interaction of a physical probe with the surface of a sample. AFM is predominantly used to characterize sample topology, surface morphology, and mechanical properties. With the use of functional tips, it is possible to image the sample conductivity[321], magnetic fields[322], and chemical composition.[323] AFM can also be performed in a liquid environment, [324–327] which has been used to study a range of molecular self-assemblies from MOFs[328] to amyloid fibrils.[329] Single-molecule force spectroscopy measures the attractive and repulsive forces experienced by the AFM tip while approaching the surface of the sample. With the force response, the inter- and intra-molecular forces can be calculated,[330–332] and is often used to characterize protein unfolding and cell adhesion.[333–335] AFM can also be used for nanoindentation experiments to make elastic modulus and stiffness measurements.[336] For more information on AFM of soft materials, the reader is directed to the following texts. [325,326,330,331,335–338] Compared to TEM, AFM provides extremely high resolution in the z direction (sub-angstrom) while the resolution in the x, y direction is typically limited by the probe-feature convolution (Figure 12 i). [326,337,339] The combination of TEM and AFM is particularly powerful for determining 3D structural information by using the high resolution information in the x,y domain obtained by TEM and the high resolution information in the z domain obtained by AFM. [296,340–342]

In the case of a vesicle, AFM provides an accurate surface profile to show the structure is convex, while TEM can provide information about the interior structure to show the structure is hollow and also determine membrane thickness (Figure 12 i).[290,343,343–346] Polymer vesicles are often used as a model system for biomembranes due to their similar properties and increased stability over liposomes.[347] Ideally, the vesicles should mimic structural features, such as size and membrane thickness, as well as mechanical properties, such as structural rigidity and surface fluidity.[348] Combined CryoTEM and AFM were used to evaluate the structural and mechanical properties of

a polydimethylsiloxane and polystyrene based block copolymer vesicle system.[343] CryoTEM determined the membrane thickness of the assemblies and revealed multilamellar vesicles, while AFM measured vesicle stiffness and topology, which was then compared to biomembranes of interest. Using information from both techniques, they concluded polydimethylsiloxane was a better model system than popular polystyrene based systems for biomedical applications due to superior stability and mechanical behavior (Figure 12 ii). Studying the relationship between the peptide formula and the resulting assembled structure is essential for creating peptide based materials.[39,349–356] For example, for a short β-sheet forming peptides, a study found that inserting a polar residue in the peptide chain increased intermolecular chain interactions directing the formation of broad ribbons which could stack face-on. TEM was used to determine ribbon widths, and AFM was used to measure the stack heights (Figure 12 iii). When the polar residue was replaced with a non-polar residue, TEM showed the formation of long, thin nano-fibrils while AFM showed the nano-fibrils were left-handed and had unique pitches.[357]

Several challenges should be considered when performing a combined/correlative AFM-TEM study, such as sample-substrate interactions. Many studies have shown vesicles deflating and flattening due to surface interactions[296,340,358] and, in some cases, substrate induced self-assembly can occur.[359] If two separate preparation methods and substrates are used, the difficulty in data interpretation can increase. Using the same substrate is preferable and enables correlative studies on individual objects (Figure 12 i). For example, graphene and graphene oxide substrates are both thin and smooth, and thus, they are suitable for both techniques.[290] Tip convolution is also important to consider when comparing images, which can cause features to appear swollen in AFM images.[339] Traditionally, AFM has been performed at slow scanning speeds (frames per minute); however, recent progress has increased the scanning speed to 20 frames per second,[360] which has enabled in-situ liquid phase AFM measurements of self-assembly mechanisms.[361] We believe a great opportunity exists for the combined use of in-situ LPTEM and AFM to study self-

assembly mechanisms where the combination would reveal both the 3D evolution and mechanical properties of self-assembled materials.

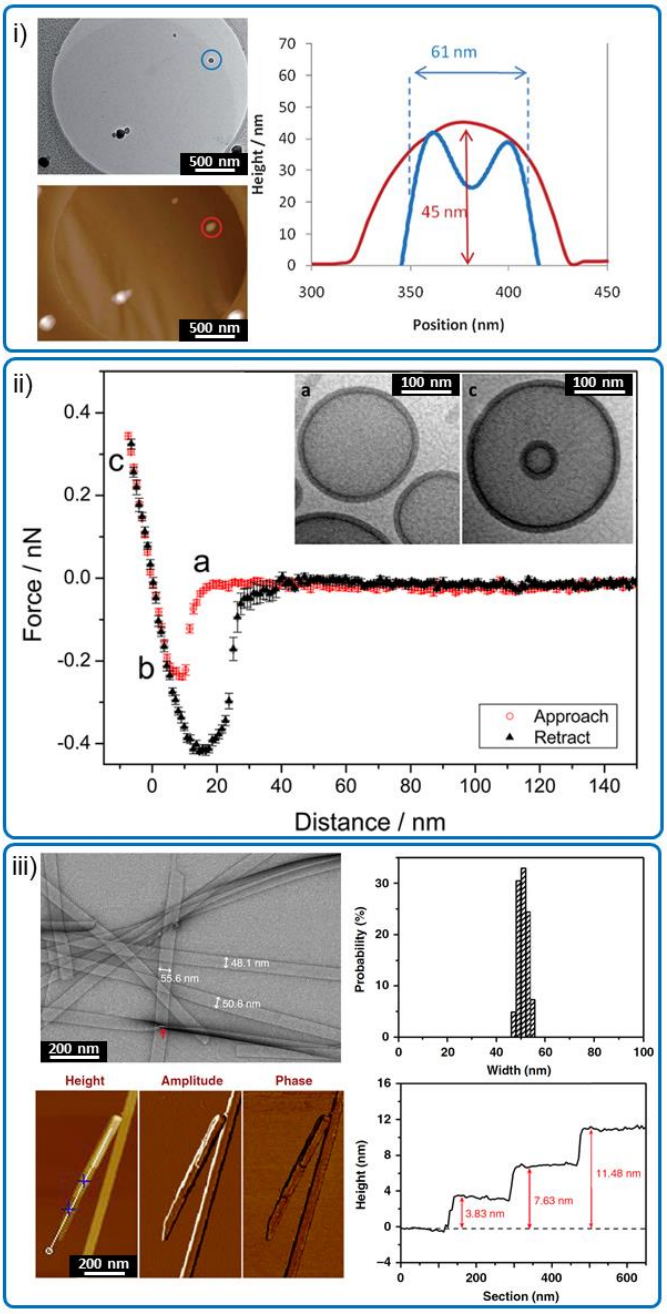

Figure 12: Examples of combined AFM/TEM studies. **i)** Comparison of AFM height profile (red) and TEM intensity profile (blue) of block copolymer polymersome on graphene oxide substrate.[290] **ii)** Force vs distance data obtained on a single PDMS-b-PMOXA polymersome. Inset shows

cryoTEM image with multilamellar vesicle and internal membrane clearly visible. Reproduced with permission from ref ([343]). Copyright 2018 Springer Nature. **iii)** (top) TEM micrograph of peptide nanoribbons with corresponding width histogram and (bottom) tapping-mode AFM image and height profile along ribbon axis. Reproduced with permission from ref ([357]). Copyright 2012 American Chemical Society.

4.5 Theoretical and computational methods

A wide range of theoretical and computational methods are used to investigate self-assembly processes including molecular dynamics (MD), dissipative particle dynamics (DPD), self-consistent field theory (SCFT), Brownian dynamics (BD), and Monte Carlo (MC). They can be broadly grouped into all-atom simulations, where each atom of the molecule and solvent is individually represented, or coarse grained simulations where multiple atoms are represented as a bead.[362] Simulations can be used to both guide experiments and interpret TEM data. The details of each method are beyond the scope of this review; however, method selection is extremely important as it dictates what type of information can be obtained for a self-assembly process such as kinetic or thermodynamic information, as well as the temporal/spatial resolution. More information on simulations of molecular self-assembly can be found in the following texts. [6,363–366] The combination of TEM and computational/theoretical methods have been used to predict and test the outcome of self-assembly processes[367], determine self-assembly mechanisms[102,368], differentiate between thermodynamic and kinetic self-assembly pathways,[100,369] and correlate experimental results.[267] Combining simulation and TEM studies is beneficial because both methods can provide information at the level of an individual particle. This combination enables the study of complex morphologies and dynamic processes that are not amenable to analysis by ensemble averaging methods.

Molecular Dynamics

Virus capsids are ordered proteins shells which encapsulate genetic material and are studied for development of antiviral drugs.[370,371] MD simulations have been used to investigate capsid-drug interaction dynamics, but such studies require detailed knowledge of the capsid structure. [372,373] In a capsid study, SPA cryoTEM (section 3.5) was used to determine the structure of the tubular HIV-1 capsid-protein assembly.[374] The cryoTEM electron density maps provided the starting positions of all-atom MD simulations of the protein assemblies, enabling future studies and therapeutic design (Figure 13 i). Additionally, atomic structures resolved from MD are often compared against TEM images to validate simulations of supercoiled DNA,[375] block copolymers,[75,104] peptide nanofibers,[376–378] polypeptoids,[73–75] amphiphilic cyanide dyes,[379] and MOFs.[380] Conversely, MD can aid in interpretation of TEM images. For example, block copolymers peptoid vesicles were studied with both methods to establish a relationship between block ratio and resulting membrane morphology.[75] CryoTEM images were classified and averaged to produce a high signal to noise images of different morphologies existing in the vesicle membrane, while MD was used to model the system at different ratios (Figure 13 iii). From the resulting atomic positions in the MD data, a TEM image was simulated for comparison with the experimental images. MD simulations can also be used to identify polymers likely to self-assemble into hierarchical structures.[6] For example, coarse grained MD was used to screen 8,000 tripeptide combinations and predict sequences most likely to assemble into hydrogels, which were then assembled and imaged with TEM to compare the predicted and experimental structure.[367]

Dissipative particle dynamics

DPD is a coarse grained simulation technique that enables large systems to be simulated efficiently, which is often required for self-assembly simulations.[381] For example, LPTEM and DPD were used to study block copolymer micelle fusion dynamics (Figure 13 iii and section 3.3).[102] The efficiency of DPD enabled simulations of micelle fusion processes which provided a much

stronger conclusion than LPTEM data alone. In this case, both the TEM and DPD indicated that the fusion event pathway depends on the relative sizes of the initial particles and that fusion results in the increase in internal water content and internal structural complexity. DPD was also used to simulate the self-assembly pathway of Janus hyperbranched polymers, revealing the polymer first formed a disorganized aggregate before transitioning into a lamella structure and eventually a vesicle with a membrane thickness of 9.2 nm.[368] TEM was used to confirm the morphology and determine an average vesicle wall thickness of 9.8 ± 0.8 nm (Figure 13 iv). While the timescale of the simulation did not match the experiment, the resulting membrane thickness was within experimental error suggesting the simulation pathway was valid.

The main challenges with combined simulation and TEM studies are related to the large discrepancies in spatial and temporal scale. In the peptide hydrogel example described previously, one MD simulation initially disagreed with the experimental result. When the simulation timescale was extended from 1,200 ns to 4,800 ns, the assembly was correctly predicted.[367] There is also a large discrepancy in timescales accessible by all-atom simulations (nanosecond to microsecond) and those probed by LPTEM (seconds to minutes).[6,382] Reducing the complexity of the interaction model can allow for longer (or larger) simulations but can decrease the accuracy of the simulations. One future direction for combined TEM simulation studies would be to use dynamic data on assembly processes in a closed feedback loop. The TEM data could be used to set boundary conditions for the simulation data, reducing the number of computations and allowing optimized model to be produced more efficiently. The optimized models could be used to predict new assembly processes, which can in turn be experimentally tested with TEM.

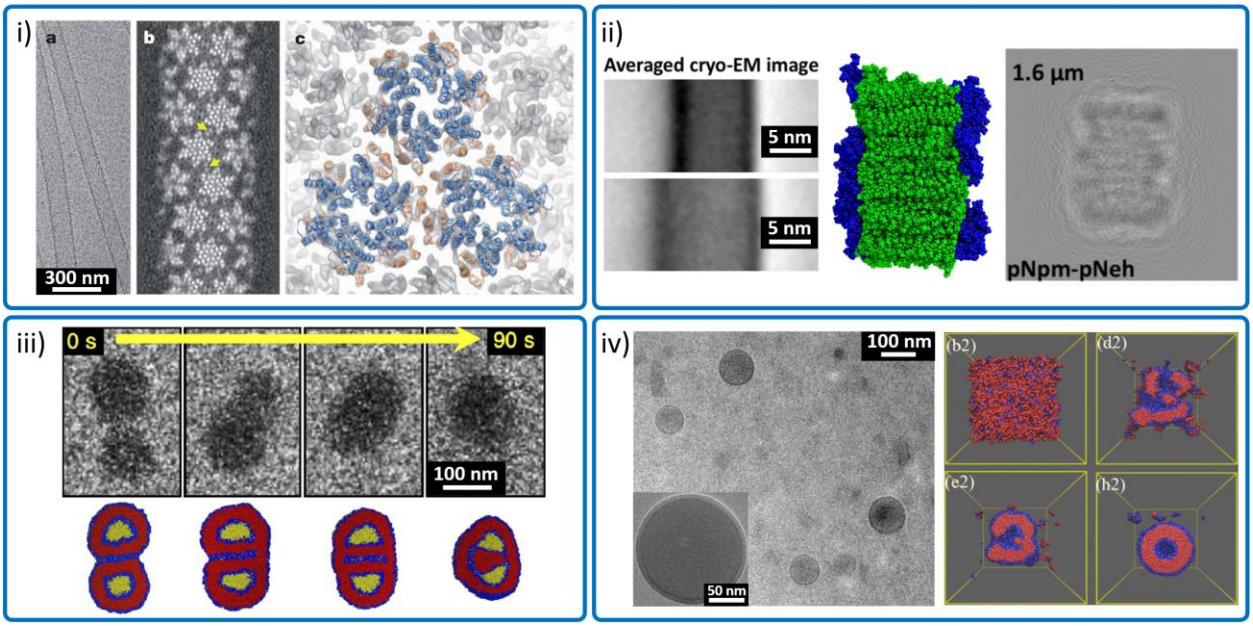

Figure 13: Examples of combined simulation/TEM studies. **i)** CryoTEM image of HIV-1 CA tubular assembly. Electron density map of a tubular assembly with helical symmetry. MD flexible fitting model of capsid assembly superimposed with electron density map. Reproduced with permission from ref ([374]). Copyright 2013 Springer Nature. **ii)** (left) Averages cryoTEM images of two classes from polypeptide block copolymer vesicles. (center) MD simulation of relaxed vesicle membrane. (right) Simulated TEM image from MD model obtained at 1.6 um defocus. Reproduced with permission from ref ([75]) Copyright 2019 American Chemical Society. **iii)** LPTEM time-lapse images of fusion-relaxation process for two block copolymer micelles. DPD simulation of fusion event. Reproduced with permission from ref ([102]). Copyright 2017 American Chemical Society. **iv)** cryoTEM images of Janus

hyperbranched polymer vesicles and cross section view of DPD simulations of the self-assembly. Reproduced with permission from ref ([368]). Copyright 2013 American Chemical Society.

TEM of different material classes

4.6 Biomolecules

Biomolecules such as peptides,[352] proteins,[383] nucleic acids,[384,385] viruses,[386] enzymes,[387] and lipids,[388] can assemble to produce nanostructured materials. Assembled biomolecules are used for surface modification[389,390], biomineralization,[391] tissue engineering,[392] and drug delivery.[303,393,394] TEM is capable of directly probing the interactions that govern these assemblies as well as the final assembled structures. However, monitoring these self-assembly mechanisms with TEM can be challenging, due to the weak binding among biomolecules which can be easily damaged by the electron beam,[395] as well as poor sample contrast.[396] Many TEM methods are developed or benchmarked on biological samples, for example staining to improve contrast,[397] cryoTEM to enhance sample stability,[398,399] electron tomography for 3D reconstruction,[150] and EELS (Section 3.1-3.6) to provide details on elemental arrangements in biomolecules.[400] All biological functions occur in hydrated environments making cryoTEM and LPTEM essential techniques for obtaining a full understanding biomaterials structure-property relationships. Using electron microscopy methods, biomolecule self-assembly has been studied for structure determination, characterization of nanoscale morphology, and self-assembly mechanisms.[24]

Structure determination

Once exclusive to crystallography and spectroscopic techniques, atomic resolution reconstructions of biological materials can now be obtained using cryoTEM (section 3.2) and electron crystallography (section 3.4). SPA (Section 3.5), which averages multiple images of the same sample, has become a popular technique for structural determination of biological samples (Figure 14 i).[399,401] This technique has been proven advantageous for determining the structure of proteins, such as the canonical transient receptor potential (TRPC3) protein, which are challenging to analyze with crystallography techniques due to crystallization difficulties. Using SPA techniques on TRPC3, cryoTEM was able to achieve the first 3D model of the protein at 15

Å resolution.[402] They were able to determine structural information on intracellular and transmembrane domains to gain information pertaining to activation ability. SPA has also been performed to obtain 3D reconstruction of viruses such as with the human adenovirus virion.[403] By achieving a 3.6 Å resolution of the virion, the study was able to gain insight into which amino acids dictated specific protein interactions. SPA has proven to be particularly useful in Alzheimer's research by imaging the structure of amyloid fibrils to gain insights of the structure and function of these peptides. Using cryoTEM, high resolution images were obtained through real-space reconstruction of a a β(1-42) peptide to develop an accurate model of the complex structure [404] In addition, images of peptide fibrils from AL proteins have been reconstructed to reveal rhombic building blocks with face-to-face packing of peptide dimers.[405] This information was able to relate the fibril formation to peptide microcrystals containing steric zippers, which provides important insight into peptide self-assembly.

Nanoscale morphology

Biomolecules can assemble into to a wide variety of nanoscale morphologies including nanofibers,[406] nanospheres,[407] vesicles,[408] nanotubes,[409] coacervates,[410] and hydrogels.[411] TEM provides visualization and quantification of the nanoscale morphologies enabling the design of biomaterials with finely tuned structural features. For example, conventional TEM has been used to study the nanoscopic structure of peptide assemblies where an in-depth analysis could be performed to analyze the width and length of the nanoribbons.[412] Linear striations of flat ribbons could be observed, and it was determined that the ribbons consisted of packed single peptide fibrils with widths ranging from 35-38 Å. The combination of cryoTEM and staining techniques revealed essential details on the morphology of a peptide amphiphile.[38] The positive stain was used to selectively stain the acidic groups revealing their surface location and providing key insights into peptide packing. In addition, by combining the techniques, a correlation between peptide amphiphile concentration and fiber structure was made, revealing that higher

concentrations result in packed flat ribbons. TEM techniques such as conventional TEM, electron tomography, and cryoTEM have frequently been used to understand and characterize DNA structures.[21,413,414] Designing molecular structures using DNA, referred to as DNA origami, has become a popular research field (Figure 14 iii). [384,385] Characterization of these nanostructures is critical in DNA origami, as the structures can have intricate internal morphologies that can only be characterized by direct visualization. By using a DNA tripod, wireframe polyhedral with 100 nm edges can be designed.[415] The study used a three-arm junction tile with a molecular weight of 5 megadaltons to construct various polyhedra, including a triangular prism, tetrahedron, a cube, a pentagonal prism, and a hexagonal prism. The characterization of such structures is only possible by visualization, making TEM the ideal instrument for this experiment.

Self-Assembly Mechanisms

Electron microscopy can be used to study the various mechanistic pathways and interactions that govern the self-assembly formation.[416] Time-resolved cryoTEM is often used to monitor self-assembly due to its ability to provide atomic detail into the assembly interactions and biomolecule conformations that occur throughout the assembly process.[417] For example, cryoTEM has been used to observe the self-assembly of cytochrome in the presence of zinc and copper, and it was discovered that metal-coordination occurs on the protein surface during the formation process. [418] It was also revealed that changing the pH could be used to control the self-assembly mechanism. In a separate study using the same metal ions, the assembly of 2D protein lattices with varying point mutations were studied with cryoTEM, which provided evidence for the various intermolecular interactions driving each mechanism.[419]

During self-assembly, some biological systems can undergo liquid-liquid phase separation (LLPS) (Figure 14 ii).[420] [421] Understanding how systems form through LLPS is essential to understanding basic biological functions such as cellular growth as well as treatment of various diseases.[422] Time-resolved cryoTEM can be used understanding self-assembly mechanisms (Section 3.2), as

demonstrated in a study where an amphiphilic amino self-assembly consisting of short peptide chains forms supramolecular polymers through an intermediate LLPS.[423] These results suggest that the formation of the LLPS of a solute-rich phase aids in a lower nucleation barrier to produce the final nanofibrils. Overall, the use of cryoTEM allowed for further insight into the complex assembly pathway that drives formation of amyloid fibrils. Additionally, LPTEM has also been used to visualize the dynamics of biomolecules providing unique insight into the formation of biomolecule assemblies by directly observing the phase transitions that occur throughout the assembly process.[108,114] For example, LPTEM has been used to observe the formation of a model protein into microdroplets through a LLPS mechanism.[420] The study produced a phase diagram which provides insight into the nucleation and growth mechanisms that dictate each final structure. Protein crystallization through amorphous precursor has also been visualized using LP-TEM.[111]

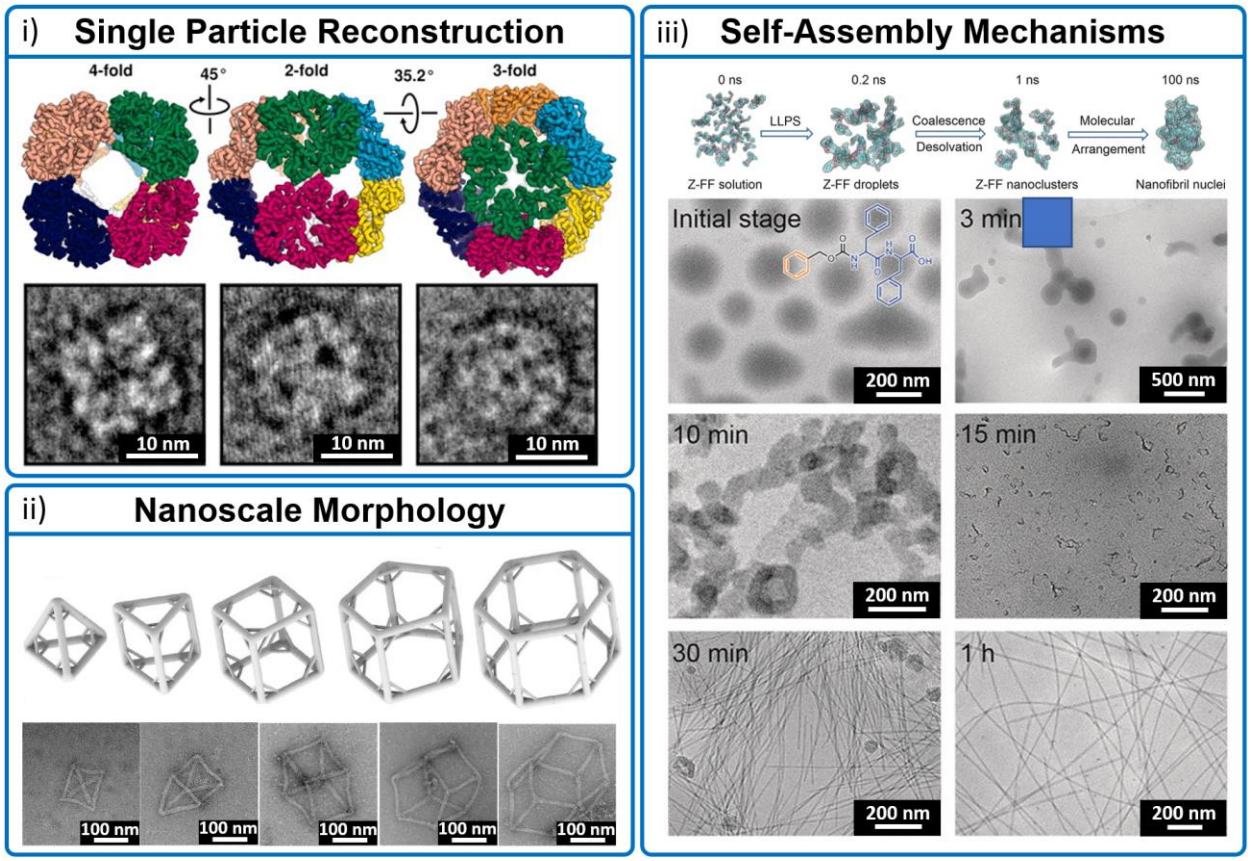

Figure 14: The versatile applications of cryoTEM in molecular self-assembly. **i)** Model and reconstructed images of O3-33 demonstrating its four-fold, two-fold, and three-fold rotational axes. . Reproduced with permission from ref ([401]). Copyright 2012 AAAS. **ii)** CryoTEM images illustrating the self-assembly mechanism of nanofibrils which proceed through LLPS. . Reproduced with permission from ref ([423]). Copyright 2019 Springer Nature. **iii)** DNA tripods assembled into various wireframe polyhedral including a tetrahedron, triangular prism, cube, pentagonal prism, and hexagonal prism. Reproduced with permission from ref ([424]). Copyright 2014 AAAS.

4.7 Porous frameworks

Crystalline porous materials such as metal-organic frameworks (MOFs) and covalent-organic frameworks (COFs) encompass a broad class of materials that find application in catalysis, separation science, sensors, energy storage, and medicine.[425,426] They are formed via the self-assembly of a wide range of building blocks including metal-ligand complexes, and organic molecules.[427] With these building blocks, various crystal morphologies, topologies, crystal structures, and chemical properties can be achieved.[426,428] In addition, these materials have high porosity,[429] surface area,[430] and crystallinity.[431] However, porous frameworks are extremely beam sensitive,[25,432] which has traditionally limited the scope and application of TEM. Recent advancements in camera technology and low-dose imaging methodologies have overcome this limitation (see section 1.2). These advancements have enabled determination of crystal structures,[25,433] morphologies,[434] local defects,[27,435,436] encapsulation of guests,[437] self-assembly mechanisms,[438,439] and dynamics of porous frameworks.[113,433] The majority of the TEM work on crystalline porous materials has been performed on MOFs, however the fundamental principles can be applied to any porous crystalline materials.

Crystal Structure Determination

MOF crystal structures are typically resolved with single crystal X-ray diffraction. However, they can also be determined with electron crystallography techniques (see section 7.2).[440] The advantage of electron diffraction tomography is that it can be used on small nanoscale crystals, whereas single crystal X-ray diffraction requires micron sized crystals. This is due to the fact that electrons interact with matter more strongly than x-rays.[25440,441] Using electron crystallography techniques many crystal structures have been resolved including UiO-66,[442] PCN-415 ($[Ti_8Zr_2,O_{12}(CH_3COO)_{16}(bdc)_6]$ and PCN-416 ($[Ti_8Zr_2,O_{12}(CH_3COO)_{16}(ndc)_6]^{23}$, MFU-4*l*,[443] Ti(IV)-based COK-47,[444] and CAU-7.[445] Electron crystallography techniques are extremely useful for MOF and COF research where growing large crystals can be the rate determining steps, or where

multiple polymorphs can exist in a single sample. In addition to electron crystallography TEM can directly image structural features such as grain boundaries and lattice fringes.[446] For example, lattice resolution images of COF-5 and COF-10 particles determined how a seeded growth synthetic process affected the crystalline properties such as fringe spacing of each COF (Figure 15 ii).[447] Crystal structure analysis is an essential part of MOF and COF analysis. TEM provides crystal structure information at the level of a single particle which is important for understanding self-assembly processes and the interfacial structures.[448,449]

Encapsulation of guest species

Porous materials are ideal for the encapsulation of guest species such as small molecules,[450] polymers,[451] biomolecules,[436,452,453] and nanoparticles.[454] TEM can be used to locate the position and orientation of the encapsulant within the framework and investigate the interactions between the frameworks and the encapsulant.[27] For example, the encapsulation of CO_2 in ZIF-8 has been imaged using CryoTEM (Figure 15 iii).[63] The low temperature was used to prevent CO_2 desorption; however, the crystals were not embedded in an ice layer which enables the high-resolution imaging. The images revealed that CO_2 has two sites within the ZIF-8 pores and that the unit cell increased in size by ~3% upon binding. Additionally, the encapsulation of proteins into MOFs is of great interest as an immobilization strategy.[452] Conventional TEM has been used to image the intermediate and final crystals for a cytochrome c-ZIF-8 MOF, [455] revealing small cavities (5-20 nm) throughout the composite, indicating that the enzyme is embedded into the MOF rather than just adsorbed to the surface. Introduction of guest species such as water and organic molecules can also initiate structural rearrangement of porous crystalline materials as reported with COF-300.[433] Using cryo-electron diffraction tomography (Section 3.4), it was observed that the COF-300 structure contracted after encapsulation of water molecules whereas the structure expanded when an organic molecule was encapsulated.

Self-assembly mechanisms

The self-assembly of MOFs is known to proceed via a wide range of mechanisms[456] that are dependent on the specific metal and ligand, the metal to ligand ratios, the precursor concentration, and the solution conditions.[438] Due to the vast chemical space for preparing MOFs, it is essential to gain an understanding of the fundamental formation mechanisms to optimize these materials.[457] Conventional TEM,[458] electron diffraction,[458] cryoTEM (Figure 15 i),[438] and LPTEM[99,459] have all been used to visualize MOF self-assembly. LPTEM was used to observe the growth of ZIF-8 in methanol, providing direct observation of the single particle growth kinetics and morphological evolution of the crystals.[99] This study only possible through careful optimization of the imaging conditions to minimize the electron-sample interactions. CryoTEM, was used to study the self-assembly in ZIF-8 in water revealing that, in contrast to the synthesis in methanol, there are long-lived pre-nucleation species (Figure 15 i).[438] The Zn and 2-methylimidazole precursor first forms ~10 nm amorphous particles before aggregating to form a liquid-like amorphous phase. The ZIF-8 nucleation occurs inside the amorphous phase which acts as a reservoir for crystal growth by monomer-addition. In the same study, the encapsulation of bovine serum albumin (BSA) into ZIF-8 by in-situ immobilization method was studied.[438] Two different mechanisms were determined according the molar ratio of ligand to metal used in the synthesis. At high ratios the ZIF-8 crystal nucleates according to the ZIF-8 only mechanism described above. Concurrently, BSA aggregates with Zn and 2-methylimidazole to form a second type of amorphous particle phase. The BSA particles undergo a solid-state transformation at the growing ZIF-8 crystal surface, restricting the encapsulation of the protein to the crystal surface. At low ligand to metal ratios the Zn and 2-methylimidazole precursor particles are unable to rapidly aggregate and bovine serum albumin promotes ZIF-8 nucleation directly, resulting in its incorporation throughout the crystal.

Post Synthetic Methods

Crystalline porous materials can be highly tunable based on formation conditions. In addition, recent studies have shown that this tunability extends even after the final crystal has been formed through processes such as polymorph switch and post synthetic exchange/modification.[460] Extensive characterization of these dynamic properties and final crystal structures allows further expansion of the functionality of crystalline porous material systems. A study on Zr6 based MOFs was completed to monitor polymorphic phase transition between the microporous, kinetic product (NU-906) and the mesoporous, thermodynamic product (NU-1008), as shown in Figure 15 iv.[113] In this study, the dissolution of NU-906 was initiated by the introduction of formic acid which then induced the formation of NU-906 through a dissolution, reprecipitation mechanism and monitored with *in situ* variable temperature LPTEM and lattice resolution TEM. Here, LPTEM enabled the visualization of morphological transformation between two polymorphs which otherwise is only characterized by studying the final products. Using these electron microscopy techniques along with variable temperature PXRD, it was observed that the polymorph transformation occurred through a concomitant dissolution-reprecipitation process. In a different study, post synthetic exchange (PSE) of metal ions and ligands was performed on UiO-66 where extensive STEM-EELS and EDX analysis (section 3.6) provided new information on a previously report system.[461] Rather than previously reported PSE of metal sites within the system, ligand-based PSC occurred with the formation of a metal oxide shell around the MOF. This study emphasizes the need for thorough characterization of MOF systems and the ability for electron microscopy to provide unique insight into material characterization

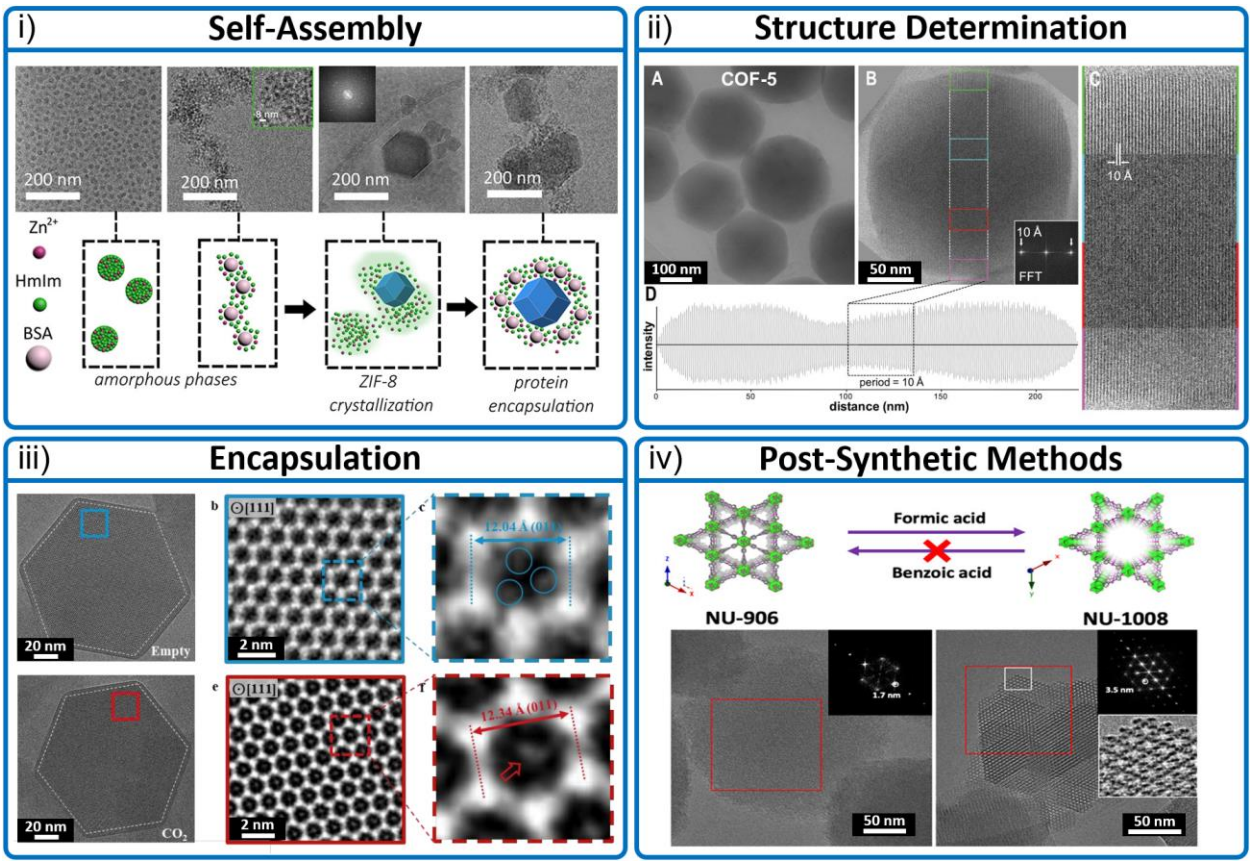

Figure 15: Various analysis of porous frameworks using TEM. **i)** TEM images and schematic of the nonclassical nucleation mechanism of ZIF-8 when at high HmIm:Zn ratios. Reproduced with permission from ref ([438]). Copyright 2020 American Chemical Society. **ii)** Lattice characterization of COF-5 particles using low-dose TEM. Reproduced with permission from ref ([447]).Copyright 2017 AAAS. **iii)** CryoTEM images of ZIF-8 without (top images) and with (bottom images) encapsulated CO_2 molecules. Reproduced with permission from ref ([63]). Copyright 2019 Elsevier. **iv)** Polymorph transformation of NU-906 to NU-1008 upon addition of formic acid. Reproduced with permission from ref ([113]). Copyright 2020 American Chemical Society.

4.8 Small molecules and polymers

Small molecules and polymers encompass a broad class of materials which includes amphiphiles,[462] surfactant-like molecules,[463] peptide-amphiphiles,[107,464–466] polypeptoids,[73–75,467–472] ionic liquids,[473,474] host guest complexes,[475–477] dendrimers[267,478,479] and block copolymers.[480–485] Unlike biomolecules and porous frameworks, these materials are typically disordered which eliminates methods such as single particle analysis or electron crystallography for structure determination. However, it should be noted that single particle analysis has been applied to several small molecule assemblies (Section 3.5). Characterization by TEM becomes more important with increasingly disordered assemblies as these structures are more difficult to analyze by ensemble methods such as spectroscopy and scattering. Small molecule and polymer assemblies can be challenging to image by TEM due to electron beam damage sensitivity and low contrast. Phase contrast TEM, and the used of phase plates, can significantly improve contrast for organic materials.[486] Moreover, modern electron detectors and low dose imaging methods help overcome these obstacles.[487] TEM is commonly used to determine nanoscale morphologies,[481,488] 3D structures,[175,489] topological defects,[189] and self-assembly mechanisms,[86,100,490] of small molecules and polymeric systems.

Nanoscale Morphology Determination

CryoTEM is often the best option for imaging the nanoscale morphology as it reduces electron beam damage, preserves structures in their native environment. However, conventional TEM is still widely used due to its accessibility and ease of use. CryoTEM and conventional TEM are commonly used for emulsions,[491–494] coacervates,[495,496] polymer composites,[497] and helical assemblies.[498,499] Crystallization driven self-assembly is a powerful method for forming well defined anisotropic assemblies, which can be achieved by controlling the growth of micelle seeds into block co-micelles. TEM has been essential for understanding this process as it can be used to visualize the seeds, the block co-micelles structure, and quantify the distribution in the block

lengths (Figure 16 iii). [19] TEM also revealed that polymer addition resulted in seed growth, rather than the nucleation of new particles. Furthermore, supramolecular polymers are often used to create nanoscale helical structures.[500] Helical structures are best characterized by cryoTEM where morphological information can provide insight on the mechanisms of self-assembly process. For example, by investigating the shapes and sizes of assemblies formed from polymers with varying ionic character, a study found that the length of helical structures could be controlled by tuning the attractive and repulsive interactions of the precursors. TEM can also be used to obtain information on multiphase nanoemulsions, which have gained interest for solubilization applications and particle templates.[491,501] The different phases of these droplets can be easily observed and differentiated with TEM (Figure 16 i). By studying the geometries of the phases with TEM, information pertaining to surface interactions, such as interfacial tensions, can be obtained.

3D structure characterization.

Many small molecule and polymer assemblies form structures with complex 3D morphologies.[488,502] For example, block copolymer assemblies form a variety of complex structures including micelles, vesicles, cylindrical micelles, inverse micellar phases, compound vesicles, and bicontinuous structures.[184,503] Differentiating these structures using 2D images can be challenging. However, electron tomography (Section 3.5) enables 3D visualization and can provide insight on the pore size, location, and connectivity, enabling a definitive morphological assignment. Poly(ionic liquid) nanoparticles can also form complex 3D structures which can be manipulated by varying the length of the alkyl sidechains.[161] 2D images revealed that the nanoparticles change in the shape and internal structure, but cryoET was required to differentiate “onion-like” and “spaghetti ball” morphologies (Figure 6 iii). Additionally, tomography has been used to characterize topological defects in self-assembled hexosomes.[189] The study discovered hexosomes contained noncircular hoops compared to traditional hexosomes which have inverse

hexagonal internal structure. The defects were explored in detail by STEM-tomography of Au-labeled samples. Based on the results of the study, the defects were hypothesized to be potential anchor points for targeting ligands or biomolecules on the surface of these nanoparticles (Figure 16 ii).

Self-assembly mechanisms

Polymer and small molecule self-assembly can proceed via a wide range of mechanisms.[475,480,504] Many factors including molecular interactions, solvent composition, temperature, pH, and precursor concentration can alter the self-assembly mechanism and the resulting morphologies. Understanding how these variables affect the mechanisms is essential to optimizing the properties of these materials. Conventional TEM,[20] cryoTEM,[184] and LPTEM[91,505] have been used to study assembly mechanisms of polymer and small molecule based systems. For example, cryoTEM has been used to study the assembly mechanism of perylene diimide amphiphiles.[86] The study revealed self-assembly proceeds in 4 stages: amorphous aggregation (I), nucleation and growth of fibril structures (II and III), and fusion of these structures to form final morphologies (IV). The study determined that hydrogen-bonding networks initiate the initial aggregation followed by desolvation, which determines the final ordering of the molecules. Additionally, peptide amphiphiles have been monitored with cryoTEM to visualize the formation of helical ribbons.[506] The helical ribbons were observed to have a twisted precursor and the morphological transition was directed by a more stable molecular packing.

Using LPTEM, block copolymers were discovered to undergo liquid-liquid phase separation (LLPS) during the formation of vesicles (Figure 16 iv).[100] The LPTEM data was used to quantify vesicle size, membrane thickness (Figure 16 iv) and contrast which was directly related to the processes of unimer insertion and chair stretching. Combining the LPTEM data with SCF (Section 4.5) revealed that vesicle size and membrane thickness were determined during the conversion of the liquid precursor droplets into the solid phase membrane through the onset of a kinetic trap.

Following this study, further block copolymer systems were discovered that self-assembled through LLPS or formed stable coacervates.[189,301] The liquid precursor phases were exploited to control the formation of nano- and micro-particles as well as macroscopic porous membrane and polymer fibers. While liquid phase precursors are well-known to occur in the formation of crystalline materials, they had not previously been considered as precursor to amorphous assemblies.[121] LPTEM has also revealed fusion[102] and encapsulation[507] mechanisms of block copolymer structures,[86] these advancements show the important role LPTEM can have in polymer research.

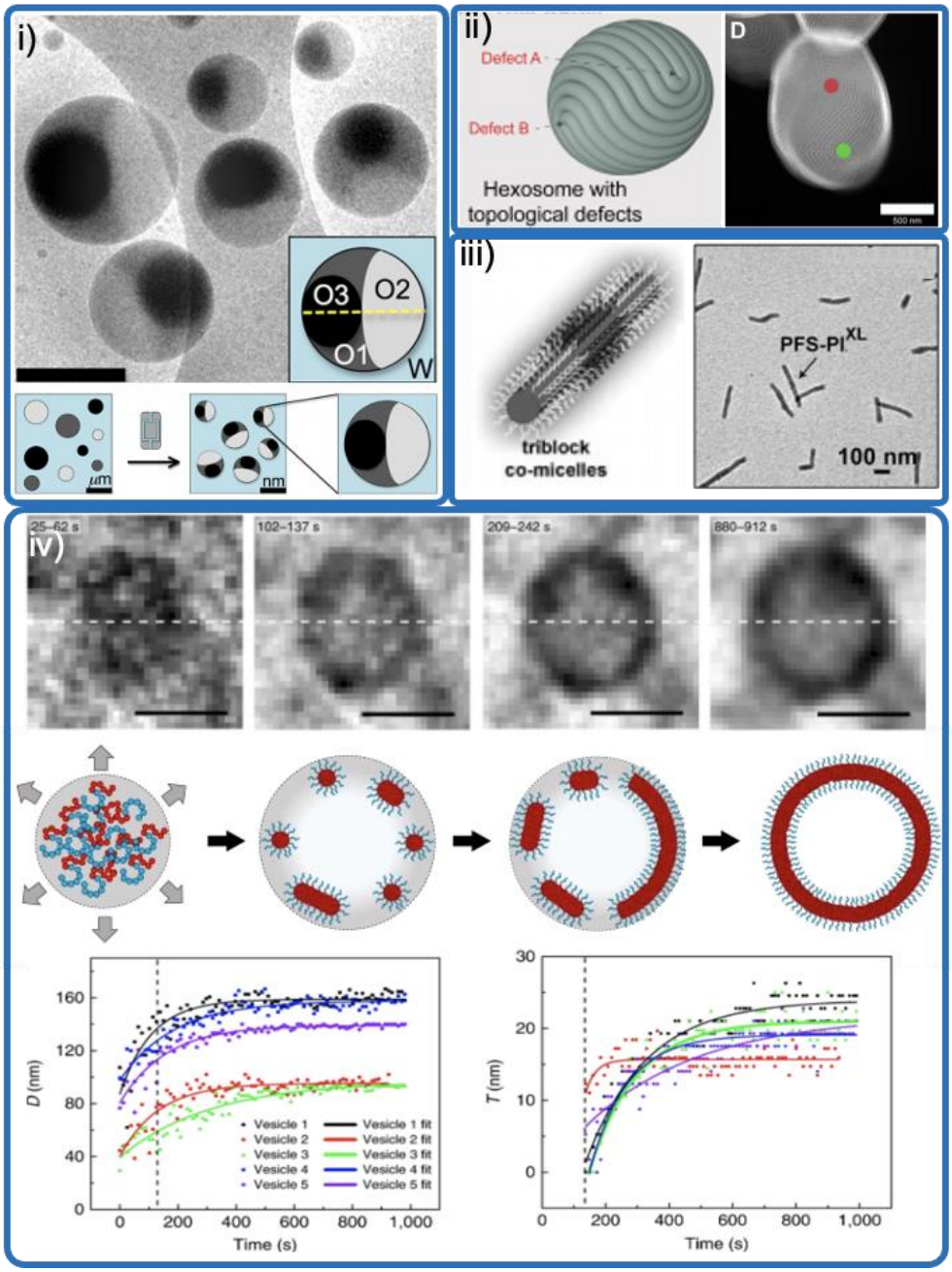

Figure 16: Various TEM applications for polymers and small molecule systems. **i)** CryoTEM of cerberus nanoemulsions produced by multidroplet flow. Different intensity regions depict different oils found within each droplet. Reproduced with permission from ref ([501]). Copyright 2013 American Chemical Society. **ii)** Topological defects in vesicular hexosomes visualized via TEM. Reproduced with permission from ref ([189]). Copyright 2020 American Chemical Society. **iii)** Cylindrical co-micelles of block copolymers characterized using conventional TEM. Reproduced

with permission from ref ([19]). Copyright 2007 AAAS. **iv)** Vesicle formation visualized in real-time using LP-TEM. The time series and schematic show the formation of a phase separated droplet (LLPS) prior to the vesicle formation. (bottom left) The evolution of vesicle diameter vs. time. (bottom right) The evolution of membrane thickness vs. time. Reproduced with permission from ref). Copyright 2019 Springer Nature.

5. Outlook

A complete understanding of molecular self-assembly is still very far away. Many phenomena still need to be discovered, visualized, and quantified. Transmission Electron Microscopy will continue to play a key role in improving our understanding of molecular self-assembly, enabling the design and development of novel materials. Modern TEM methods are so powerful that all researchers in molecular self-assembly would benefit from their utilization. However, most researchers in molecular self-assembly are not TEM experts. Therefore, we believe the most important TEM developments are those that improve accessibility, automation, and data integration. This is in addition to the continued developments to improve resolution.

Accessibility: Many researchers do not have access to modern TEM facilities due to the high cost of the instruments, expert staff, service contracts, and maintenance. Historically, TEM development has focused on improving the resolution, with minimum attention given to producing affordable, robust microscopes. More recently, lower-cost cryoTEMs with reduced service contracts have emerged as well as tabletop TEMs,[508,509] which do not require service contracts. The tabletop TEMs have limited functionality but can be excellent tools for performing simple imaging tasks. In addition, tabletop TEMs provide an affordable platform for all researchers, and the simple operation makes them great teaching microscopes at the undergraduate level. Continued developments in the functionality of tabletop TEM and reduced cost of conventional TEMs are essential for improving accessibility. The collection of high quality TEM data requires a significant amount of expertise and training, further limiting the accessibility of TEM. While maintaining a community of TEM experts is essential, the development of automated microscopes that enable non-experts to routinely collect high quality data is equally essential to expanding the accessibility of TEM.

Automation: Most of the TEM methods discussed in this review are considered routine for highly trained electron microscopists. The training of researchers to perform complicated but highly

repetitive tasks such as sample preparation[510,511], microscope operation[512] and data analysis[513,514] is a significant waste of resources, especially considering recent advancement in the automation of these tasks. While research into automation already exists, automated routines are not widely used. This is in part due to the fact they only work well for a limited number of specific tasks and are often expensive. To address this problem, we need to improve open-source intelligent automation that can deal with many different tasks, as well as develop task specific microscopes for the most important and routinely applied experiments. In our opinion, the technology already exists to develop fully automated, low-cost microscopes that can perform 2D conventional and cryogenic TEM. If these microscopes were widely available to the molecular assembly community, an unprecedented increase in self-assembly knowledge would occur. We believe the development of intelligent microscopes will be enabled by machine learning.[515] Ideally machine learning enabled microscopes will require minimal service and knowledge to operate, and improvements in their capabilities can be achieved by software upgrades rather than a complete microscope upgrade every few years. Importantly, these automated microscopes will likely be separate products from the traditional microscopes used by expert microscopists to develop new methods. The development of new methods is still an essential task, especially in the areas of liquid-phase TEM, analytical TEM, electron tomography, analytical TEM, and 4D-STEM which are still in their infancy compared to conventional TEM and cryoTEM. This development can be aided by automation but will also require a significant amount of highly skilled manual development.

Data Integration: Although it is widely recognized that multiple theoretical and analytical methods are needed to fully understand complex processes, the data from each method is typically summarized qualitatively. For example, a recent review of mechanistic studies on MOF nucleation and growth revealed that at least eight separate papers have been published in the past seven years on the time-resolved, mechanistic studies of ZIF-8 with almost identical synthetic conditions.[516] The ZIF-8 system has been studied with many different techniques including

electron microscopy, light and x-ray scattering techniques, molecular dynamics simulation and NMR spectroscopy. The summation of this data was qualitatively summarized in their review article to provide our 'best current description' of the formation process; this is our standard method for collating and interpreting data. Intuitively, we know this is not the most rigorous way of using this large amount of data. However, if instead we could quantitatively merge datasets together after they are published, we could create a single 'best' description that can evolve with every new publication. This would enable researchers to benchmark new data and new TEM methods against existing datasets prior to publication. More importantly it would significantly enhance the information from combined and correlative studies. A key feature of this integration will be combining the typically nanoscale structural information from TEM with chemical and bonding information from molecular dynamics simulations or more common chemical analytical tools such as NMR, IR, Raman and Mass Spectrometry. This integration is going to be essential for providing a link between molecular chemistry the emergence of supramolecular structural dynamics. Data integration will be enabled by the advancement in automation as described above, as automation will enable the collection of precisely labelled TEM data. However data integration will also require the development of open source data storage and computational frameworks that enable users to seamlessly combine multiple types of data,[513] to provide an evaluation that is greater than the sum of its parts.

Resolution: Understanding molecular self-assembly requires TEM methods that can probe the appropriate time and space domains.[517] Improvements in temporal and spatial resolution enable the study of new structures and dynamic processes. TEM methods applied to molecular self-assembly are typically not limited by the microscope but are limited by beam sensitivity of the samples – dose limited resolution. This is especially true for electron tomography, liquid-phase TEM and elemental mapping. For example, atomic-resolution electron tomography of beam sensitive materials could be considered a grand challenge. Improving the resolution of dose

limited imaging requires a better fundamental understanding of the electron-sample interactions as well as optimizing every electron-sample interaction. For example, electron pulsing,[107,518,519] and sub-sampling[520] has been shown to significantly reduce electron-beam damage. Improving our understanding of this phenomena and our ability to precisely control how the beam is applied to our sample will result in significant improvements in resolution. Direct electron detectors are already capable of single electron counting,[521] and while detection improvements are possible, it is unlikely to generate a step function increase in capability. A more promising alternative is to use these detectors more effectively. Typically, TEM experiments on molecular assemblies only collect a fraction of the possible data, for example collecting either bright field or dark field images. However, there is great potential in developing detection systems that collect multiple types of information simultaneously.[209] This greatly increases the information content of each exposure and ultimately increases the resolution for dose limited experiments.

Conclusion: TEM has made an enormous contribution to the field of molecular self-assembly by enabling the discovery, visualization and quantification of structures and dynamic processes. Conventional TEM is the most accessible and high throughput method and is suitable for materials that are stable to high vacuum. CryoTEM is the preferred method for imaging solvated structures at high resolution, and LPTEM is the preferred method for understanding dynamic processes. SPA and Electron Crystallography can be used to determine the 3D structure of atomically precise materials, and electron tomography enables 3D reconstructions of unique objects. Elemental and bonding information can be obtained using EELS and EDX. This suit of methods encompasses essentially all of our required knowledge about self-assembled systems. Continued improvements in TEM methods will help to bridge our self-assembly knowledge gaps. The most important developments for the application of TEM to molecular self-assembly will focus on improving the accessibility and automation of TEM experiments. The ability to routinely perform a suit of TEM methods when designing and developing new self-assembled materials will have a

profound impact on the field of molecular self-assembly. TEM has revealed that molecular self-assembly is more complex than we previously thought. Within a single experiment, it is common for multiple phase changes to occur and for the final structures to be determined by multiple pathways occurring simultaneously. Resolving these complex mechanisms requires quantitatively combining data from multiple TEM methods and complementary analytical and computation methods. With this combined data in hand, we will finally be able to embrace the complexity of self-assembly and re-design our synthetic methods to create new materials with improved and unique functions.

6. Addendum

The following addendum provides text which covers some information that may benefit the reader. Additional references are also provided for readers that are further interested. While these sections do not always directly relate to molecular self-assembly, understanding how the TEM operates in different modes and the knowledge of its limitations is essential to study molecular self-assembly using the TEM.

6.1 Microscope components

The transmission electron microscope (TEM) consists of 3 essential components: (1) an electron gun, which produces the electron beam, (2) a series of electromagnetic lens systems which are used to align and project the electron beam, and (3) a camera which detects the transmitted or scattered electrons and records the image (Figure 17).[10] These components are located within a vertical microscope column that is under high vacuum to prevent scattering from gas molecules. Traditionally, TEM electron guns were made of thermoionic tungsten or lanthanum hexaboride (LaB6) filaments. However, most modern TEMs are built with field emission guns (FEG) which

provide greater coherence and brightness. Most electron guns accelerate electrons ranging from 40-300 keV; however, higher voltages can be used for imaging thicker samples.

Three electromagnetic lens systems are arranged below the electron gun: the condenser, objective, and protector lens systems. Each system will have one or more lenses, deflectors, stigmators, and apertures. All electromagnetic lenses are convex lenses and are used to focus the electron beam to a focal point. Deflectors and stigmators impose a weak electromagnetic field on the electron beam; thus, their role is to manipulate the angle (deflectors) or shape (stigmators) of the beam. Apertures are typically circular holes in thin metal sheets and are used to isolate different parts of the electron beam. The role of the condenser lens system is to direct the electron beam towards the sample. The user can control the brightness and convergence angle of the beam incident upon the sample. The sample, contained in a specimen holder, is inserted in a specimen chamber located below the condenser lens system. Within the chamber, the specimen location and tilt angle can be adjusted to view different locations and orientations. The specimen chamber can be found between two pole pieces of the objective lens. After the electron beam transmits through the sample, the objective lens system forms the image or diffraction pattern. There are several imaging modes available in a TEM which provide different information about the sample (see section 7.3). In short, image mode obtains real-space information by focusing the image plane onto the detector while diffraction mode obtains reciprocal space information by focusing the back focal plane onto the detector. In addition, the magnification of both the real-space image and diffraction pattern can be adjusted through the projector lenses with the magnification being described as camera length in the diffraction mode. Similar to the condenser lens, the objective lens also has apertures of various sizes that can be inserted to filter unscattered or scattered electrons for producing dark field images or enhancing contrast in bright field images respectively.

While a phosphorous screen is typically used for viewing a sample, various detectors exist for capturing real-space images and diffraction patterns. The most common detectors are, charge

couple devices (CCD), complementary metal oxide semiconductor (CMOS) and direct electron detectors (DED).[522,523] CCD and CMOS cameras use scintillators to convert the detected electrons into photons that are then transferred to the final detector. DED can directly detect electrons and do not require scintillators. DED have a greater detective quantum efficiency and are 10-100 times more sensitive to electrons compared to CCD cameras; thus, they are favorable for low electron dose experiments such as in cryoTEM (see section 3.2). DED also are capable of high framerates, which is ideal for LPTEM (see section 3.3) and 4D-STEM (see section 3.7). Like other lens-based microscopes, TEM also suffers from aberrations and astigmatisms that can reduce image quality. Spherical aberration is typically reduced through the insertion of apertures to block the electrons on the periphery of the electron beam. For high resolution studies, spherical aberration correctors, which consists of two hexapoles and two round-lens, can be used to reduce the aberrations in the objective lens even further.[524] Chromatic aberrations also reduce image quality and can be reduced by using monochromators or in-column energy filters to decrease the electron energy spread. Energy filters can also be used to improve contrast or perform elemental mapping by selecting electrons of specific energies.

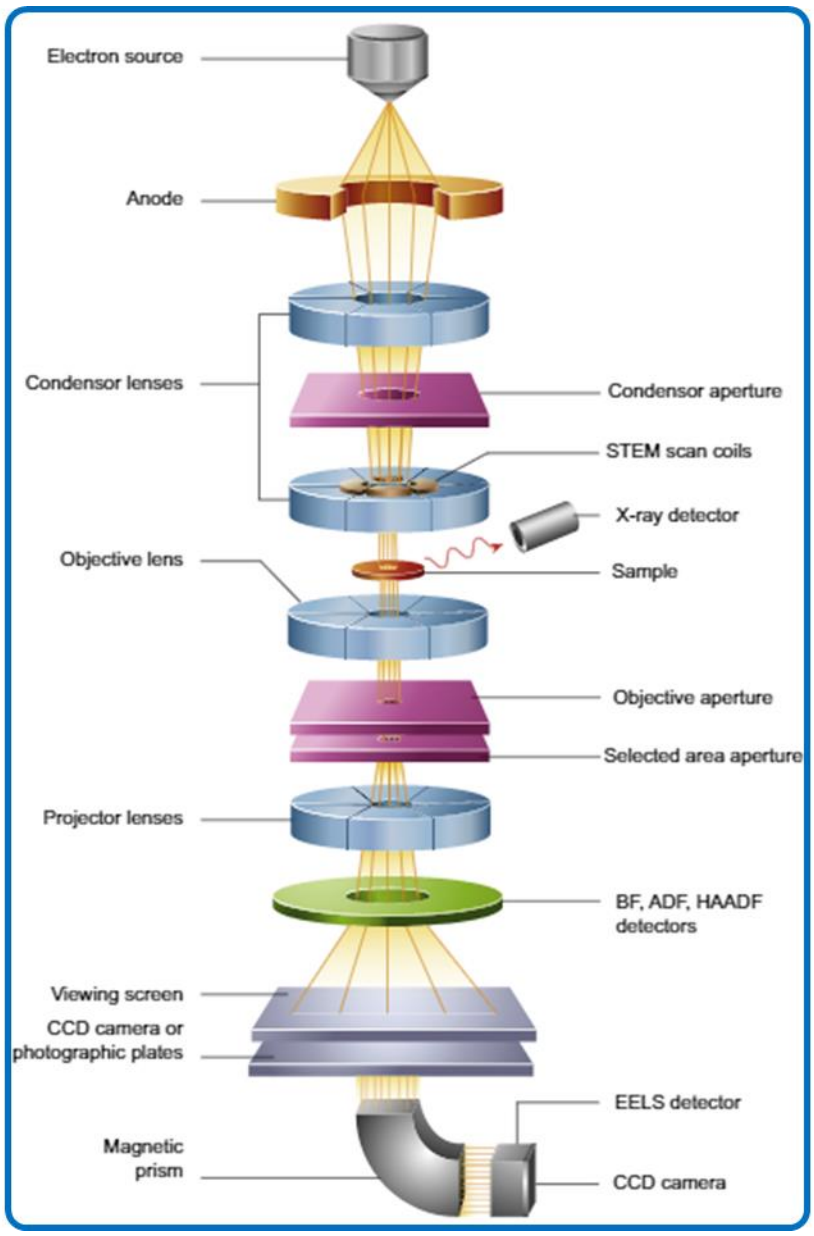

Figure 17: Simplified schematic of a transmission electron microscope. Reproduced with permission from ref ([298]). Copyright 2016 Elsevier.

6.2 Sample Preparation

Proper sample preparation is essential to extracting useful information from TEM images. While nanoscopy methods cannot observe structures in their truly native state, better representations

of the native state can be obtained by using methods that minimize artefacts and structural rearrangement during sample preparation. The most important considerations for sample preparation are sample volatility, thickness, scattering power, and density on the grid. The vacuum of the microscope requires that volatile compounds are removed (conventional TEM), vitrified (cryoTEM), or contained using specialized holders (LPTEM). Structures that are < 1 micron thick can be deposited on TEM grid without prior processing.[60] Structures that are > 1 micron thick require an extra thinning step, such as microtomy or a focused ion beam milling,[525] which can be performed after dehydration or under cryogenic conditions.[526] To obtain useful information, samples must have sufficient scattering power compared to the background or substrate. For organic specimens, heavy metal stains are commonly added to increase the scattering difference between the object and the background.[396,527,528] Positive stains selectively bind to the object, and negative stains selectively bind to the background.[528] However, staining can induce artifacts that lead to false interpretation.[529] Another approach is to use substrates such as graphene or graphene oxide that have very low scattering power.[16,530,531] The low scattering power of these substrates increases the scattering difference between the object and the background removing the need for staining. These substrate can also be used in combination with cryoTEM to obtain thin ice layers.[532]

The ideal TEM grid contains a high density of objects that are not overlapping. Overlapping objects significantly increase the difficulty of visualization and image analysis. Grids with a very low density of objects requires significantly more imaging time to obtain the required statistics. Optimizing the density of objects on the grid depends on the specific sample preparation method; however, the particle concentration in solution is the most important factor to optimize.

The most common way to prepare samples for conventional TEM is by drop casting a solution onto a TEM grid and letting it evaporate. For some materials, the evaporation process can damage or alter the assembled structures limiting the scope of conventional TEM.[529] The standard TEM grid is a 3 mm disc made from a support material such as copper, gold, and silicon, and the

grid can be coated with a thin film such as amorphous carbon, graphene, graphene oxide, or silicon nitride. The grids are divided into sections where the number of sections is given by the mesh size. The thin films can be continuous or porous (also known as holey or lacy).

The most common method used to prepare cryoTEM samples is referred to as “plunge freezing”.[398,525] The TEM grid is treated with plasma to clean and make the grid surface more hydrophilic. The sample is then deposited on to the grid by pipetting ~3 μL of solution. The excess solution is then blotted off using a filter paper, and the pressure and the blotting time will determine the thickness of the vitrified ice layer. Once the sample is blotted, it is plunged into a cryogenic agent, such as ethane or propane, for vitrification. This process is now widely performed using automated instruments to increase the sample quality and reproducibility. Overall, controlling the rate of vitrification is essential to avoiding artefacts such as crystalline ice, which forms as a result of slow vitrification. The environment, specifically the humidity and temperature, should also be carefully monitored throughout the plunge freezing process to prevent sample evaporation. Thus, the sample application, blotting, and plunging are performed in a controlled environment vitrification system (CEVS).[57] After sample preparation, the sample can then be transferred to a cryo-holder, which maintains cryogenic conditions during imaging. Although cryoTEM is ideal for preventing drying artefacts, care should be taken while interpreting images because the shear forces which are applied to the sample during blotting are sufficient to reorganize assembled structures.[60,533,534] Furthermore, confinement within the thin liquid layers prior to vitrification can result in size sorting effects.[535,536]

LPTEM can be performed by three different methods: 1) enclosing the liquid within a cell, also known as Liquid cell TEM.[537,538] 2) using a differential pumping system to create a high pressure around the sample, also known as environmental TEM (ETEM),[539] and 3) using non-volatile liquids as the reaction media.[473,474] Although the non-volatile liquid method is the simplest, it is limited to solvents such as ionic liquids. The ETEM method can be used to image liquids,[539] but it is more commonly used to image in the gas phase due to limitations in pressure range. Liquid

cell is most commonly performed by enclosing samples inside a silicon nitride microchip[540] or a graphene cell.[541] The advantage of the silicon nitride cell is that they are fabricated with micro-electro-mechanical systems (MEMS) technology, which is inherently scalable. MEMS technology also enables controlled flow,[128] electrochemistry,[542] and heating,[113,117,128] experiments to be performed inside the microscope with modern holders. The advantage of the graphene cell is that the thin layer of graphene provide minimal background scattering which enables higher resolution imaging,[541,543] and the conductivity of the graphene reduces beam damage.[106,541] While used widely, graphene cells are usually limited to small imaging areas (typically limited to 20 x 20 microns) which limits the size of structures studied within them.

When designing LPTEM experiments, sample concentration and microchip surface are important to consider. High sample concentrations can cause viewing area to be completely blocked, which ends an experiment. However, with low concentration samples, dynamics are less likely to occur in the viewing area.[92] The cleanliness of the silicon nitride cells is essential for preparing LPTEM samples. The surface of the microchips should be plasma cleaned and observed using an optical microscope for any impurities. The plasma charges the surface of the microchips, which can influence the motion of particles within the cell. The ideal liquid cell has surface charges that are optimized to control particle motion such that the dynamics can be imaged with an appropriate temporal resolution. Although surface charges are known to effect motion within the cell, there are currently no demonstrations that dynamics can be controlled or predicted based on a specific surface treatment method. Additionally, the thickness of the cell must be thin enough to obtain the desired resolution.[544]

6.3 Imaging modes

Contrast can be defined as the difference in measured intensity of an object with respect to the background.[9] Contrast is generated by three mechanisms: mass-thickness contrast, diffraction

contrast, and phase contrast. TEM images are formed from a combination of all mechanisms. However, depending on the sample and imaging mode, one or more mechanisms may be dominant. Mass-thickness contrast refers to the difference in sample thickness or electron density; samples with greater thickness and/or electron density will scatter more electrons and have greater contrast. Heavy metal stains can be implemented to improve contrast to molecular self-assemblies, which is an exploitation of mass-thickness contrast.

Diffraction contrast refers to the contrast generated when electrons undergo Bragg scattering. Diffraction contrast is typically used for the collection of diffraction patterns; however, it can also significantly contribute to the contrast in real-space TEM images.[545] Diffraction contrast makes quantitative interpretation of the real-space images challenging,[546] but it can aid in qualitative interpretation of a sample. For example, if the sample shows clear diffraction contrast, it must be a crystalline sample, but lack of diffraction contrast does not prove the sample is amorphous.

Phase contrast occurs because most scattering events result in a phase shift of the electrons. This can result in constructive or destructive interference at the electron detector and can enhance the difference in detected intensity between the object and the background. Phase contrast is most dominant in bright field images at higher magnifications and for thin, low atomic number samples that do not significantly scatter electrons such as most molecular assemblies. Phase contrast can be difficult to quantitatively interpret, requiring knowledge of the contrast transfer function.[547] Consideration and correction of the contrast transfer function is essential for high-resolution TEM images and is common in single particle analysis[548] and electron tomography[549]. In addition, the defocus value can be used to finely tune the contrast transfer function and, therefore, phase contrast. Increasing the defocus value increases phase contrast but results in lower spatial resolution. For a single image, the user must decide on this trade-off depending on the goal of the image. However, high resolution, high contrast images can still be obtained through the use of phase plates[550], or exit wave reconstruction[547].

TEM can be operated in an array of imaging modes including TEM and Scanning TEM (STEM).[551] TEM is performed by using the condenser lens system to direct a parallel electron beam through a small area of the sample, perpendicular to the sample plane (section 7.1). Once the beam transmits through the sample, the information in each pixel is collected simultaneously. As the electron beam is circular and the detectors are square or rectangular, the area of sample exposed to electrons is typically larger than the imaging area, which is important when interpreting electron-sample interactions or performing low-dose or controlled-dose imaging (section 7.4). STEM imaging is performed by using the objective lens system to focus the electron beam to a small point on the sample. In addition, STEM uses scanning coils to raster the beam across the sample where the information in each pixel is collected sequentially. The electron-sample interactions are limited to the imaging area; however, the interactions can be more complicated due to spatial-temporal inhomogeneity in the collection of the image.

TEM and STEM can further operate in either bright-field or dark-field imaging settings. Bright-field imaging refers to the collection of transmitted electrons (i.e. electrons that are not scattering by the specimen). In bright-field images, the areas of the grid that scatter electrons the least, such as the substrate or holes in the substrate, appear bright, whereas areas that scatter electrons the most, typically the sample, appear dark. Dark-field imaging refers to the collection of only the scattered electrons, so contrast is inverted compared to bright field images. Dark-field TEM imaging is typically performed by either moving the objective aperture away from the optical axis (i.e. low-resolution approach) or by tilting the beam (i.e. high-resolution approach). Using either approach, only a fraction of the scattered electrons will be collected, so the images may have significantly lower signal to noise than bright-field images. Dark-field images can also be collected using annular detectors, which is the preferred method for performing dark-field STEM. The transmitted beam passes through the center of the detector and the annular detector collects all of the scattered electron at a given scattering angle. For example, High Angle Annular Dark Field

(HAADF) imaging is the collection of electrons at angles > 50 mrad. The advantage of HAADF imaging is that only the inelastically scattered electrons are collected which greatly simplifies the image contrast mechanisms. HAADF images are often referred to as Z-contrast images because the contrast is directly proportional to the local electron density. In this review, we typically do not specify the imaging mode and use “TEM” as the umbrella term unless there is a specific reason to do otherwise.

6.4 Electron-sample interactions

Electron-sample interactions are essential for TEM imaging, as the elastic and inelastic scattering of electrons produces the features in the TEM image.[552] Furthermore, interaction effects like emitted X-rays, secondary electrons, or energy losses of inelastic electrons are essential for performing analytical TEM (Figure 7, section 3.6). Interaction effects can slow the primary electrons, produce secondary electrons, and/or emit x-rays which can be used in analytical TEM to gain additional information about the sample. Electron-sample interactions can also damage the sample, resulting in images that are not representative of the undamaged sample. The damaged images can lead to incorrect interpretation of the self-assembly process and should be avoided where possible. In the discussion of electron-sample interactions, the term “low-dose” is frequently used; however, it can have several definitions. One definition is that the total number of electrons per unit area of sample (often referred to as total or cumulative dose) during imaging is below a certain threshold, for example 1 $e^{-}A^{-2}$. In methods such as LPTEM, low-dose is also used to refer to a dose rate threshold (number of electrons per unit area per unit time). Imaging below given thresholds can be a useful guideline for well-established methods (e.g. cryoTEM of proteins); however for each imaging mode, different samples and sample preparation methods will have different electron-sample interactions. Therefore, for unestablished methods, imaging modes, and samples, it is essential to perform electron-sample interaction studies (discussed below). Another definition for the term low-dose is that an imaging procedure was used such that

the sample was only exposed to electrons during the acquisition of the image, and the sample was not exposed to the electron beam during microscope alignment, locating the sample, or focusing. This is often referred to as the “low-dose” procedure. The challenge with this definition is that the images collected could still not be representative of the undamaged sample if the electron dose is sufficient to damage the sample. A better term for this procedure might be “controlled-dose”.

We believe that electron-sample interactions should be defined as being either useful or harmful and as either significant or insignificant. Importantly, this definition can only be made with respect to a specific goal and through a quantification of the result of the interaction. For example, if the user has the goal of measuring the size of a nanoparticle, and the electron-sample interactions result in an increase in the size of the nanoparticle, the interaction is defined as harmful. However, if the size increase is < 1% then this could be considered an insignificant interaction. When the interaction is harmful but insignificant with respect to the goal, the image can be considered a “low-dose” image. On the other hand, when the interaction is harmful and significant with respect to the goal, the image can be defined as “beam damaged”. To definitively assign an image as being low-dose, it is important to define the goal of image collection. For example, if during the collection of an image of a crystalline nanoparticle, several atoms are displaced from their original position (knock-on damage, see below), the image would be considered “beam damaged” with respect to the atomic structure. However, no significant nanoparticle size change from the image would be considered “low-dose” with respect to the nanoparticle size. This distinction becomes especially important for methods such as LPTEM where it is common to use the electron beam to initiate and control solution chemistry,[129] enabling observation of the resulting chemical dynamics and self-assembly processes. For example, a LPTEM study has shown that the electron beam can be used to control the solution ionic strength to induce self-assembly of ligand functionalized nanoparticles.[553] In this study, it was essential to show that electron interactions

were not displacing the organic ligands on the surface of the nanoparticles.[554] Whether the goal is to perform low-dose imaging or to use the electron beam as a stimulus, it is necessary to have a fundamental understanding of how electrons interact with matter and the experimental methods used to quantify these interactions. Here, we will provide an overview of these topics. The reader is directed to the following text for more information.[13,129,555]

Electron-sample interaction mechanisms: Electrons interact with matter through elastic and inelastic scatting events. In an elastic scattering event, the total kinetic energy is conserved, but the direction of propagation is altered. This is responsible for electron diffraction which can used to determine crystal structures (section 3.4). In an inelastic scattering event, the total kinetic energy is not conserved. Inelastic events are useful for spectroscopic methods like EELS (section 3.6) which allows elemental mapping and vibrational spectroscopy of the specimen being imaged. Elastic and inelastic electron-sample interactions can produce three main products: radiolysis, knock-on damage, and electrostatic charging. Radiolysis is a result of inelastic scattering of primary electrons. During radiolysis, the electrons from the TEM excite the specimen, which quickly loses energy without returning to its original ground state, resulting in bond scissions and permanent change in structure. Knock-on damage is a result of elastic collisions that often involve small angles and minimal energy transfer; however, at large angles these collisions can transfer several eV of energy to the nuclei and eject atoms from the specimen. Electrostatic charging occurs when the irradiation area accumulates charge during imaging. This accumulation of charge can deflect incident electrons introducing artefacts. The damage mechanism at play is determined by the electrical conductivity of the specimen and the temperature dependence of the damage.[552] Conductive materials have minimal radiolytic damage as the high charge mobility can quench excited species. However, most of molecular assemblies are not conductive, so radiolysis is typically the dominant damage mechanism.[556]

Measuring electron-sample interactions: While several methods are used to quantify electron-sample interactions, the basic principle is that multiple measurements should be made as a function of total dose or dose rate where any changes in the measurement can be considered a result of the electron-sample interactions. Quantifying these changes enables the user to define a given threshold for an acceptable change. Quantifying the changes as a function of different parameters (e.g. electron voltage, beam diameter, sample composition, sample thickness) provides detailed information on how to minimize the electron-sample interactions (discussed in more detail below). For crystalline particles, these measurements are most commonly performed in diffraction mode.[557,558] Diffraction mode is useful because it enables the collection of high resolution, high signal to noise information at relative low doses compared to real space imaging. Diffraction images of crystalline samples display sharp peaks, which will blur and decrease in intensity as the electron beam damages the crystallinity. Damage always propagates from high resolution information to low resolution information; therefore, the outermost spots in the diffraction pattern are affected first. A critical dose is typically defined when intensity of particular diffraction spots or rings drops to 1/e of the maximum value.[559] This method can also be applied to amorphous or semi-crystalline samples that display diffraction rings, rather than discrete spots.[560] Electron-sample interactions can also be quantified by analyzing changes in the real-space images, which can be related to changes in sample size, shape, or contrast due to material being lost or deposited.[560] Electron-sample interactions can also be measured using EELS or EDS (section 3.6) as damage can cause a change in the local elemental composition and bonding.[13]

Strategies to minimize electron-samples interactions: Several strategies can prevent sample damage; the simplest of which is to reduce the number of electrons that interact with the sample. The consequence of this is that the resulting images will have lower signal to noise. While low

signal to noise images are difficult or impossible to visually interpret, they can contain equally high-resolution information. As automated data analysis improves, especially for real-time analysis, our need for high signal to noise images will decrease. This has been demonstrated through the application of subsampled/compressed sensing TEM.[561–564]

The electron accelerating voltage is an important variable for minimizing damage; however, care should be taken to correctly diagnose the problem. While lower voltages can be used to get below the knock-on damage threshold, lower voltages increases damage from radiolysis.[565] As radiolysis is the dominant mechanism for non-conducting samples, damage is typically minimized at higher voltages. Radiolysis effects can be minimized by lowering the specimen temperature. For example, in cryoTEM, the ice layer around the sample also acts as an additional protective layer.[13,566] Staining is another common method to minimize damage, but this strategy can introduce artifacts. Pulsed electron beams with femto or pico second pulses can also be used to reduce damage if “healing” can occur between pulses.[13,518,567,568]

Consideration for LPTEM: Electron-sample interactions for liquids have been widely discussed, and is an area of active and much needed research.[91,555] The electron beam is known to partially decompose all liquids,[537] and the dominant mechanisms are thought to be radiolysis[555] and charging.[129,569,570] Charging occurs when the incident electron interacts with non-bonding electrons within the sample, and the result of that interaction is charge accumulation. While radiolysis generates reactive species, charging results in the redistribution of charged species. The result of both effects is that the composition of the liquid being imaged will not be the same as the composition which was loaded into the cell. This presents a significant challenge for interpreting LPTEM data and performing low dose imaging. Typically, LPTEM experiments are performed to observe a dynamic process, i.e. the conversion of a starting material to a product. One approach is to perform the electron-sample interaction studies on the starting materials and/or final products.[99] This can be a useful guide for optimizing imaging conditions to perform

low dose studies, but it is important to remember that the electron-sample interactions of the intermediates could be very different from either the starting materials or products. Another approach is to perform so called “postmortem” analysis which involves tearing apart the liquid cell and drying the sample. This enables other analysis methods that may not be possible to perform inside the microscope or the liquid state.[107] Another approach is to perform the dynamic studies at multiple doses and to analyze the data as a function of the total dose or dose rate.[102] This can enable the extrapolation of dynamic data to “zero-dose” conditions.[571] A final approach is to perform combined studies and look for consistent behavior across multiple methods such as molecular simulation and scattering experiments. Molecular dynamics is an extremely important approach here as it can also be used to obtain dynamics at the single particle level.[102] While these approaches are informative, none of them are sufficient to definitively prove that the data collected was “low-dose,” so we should remain open to the possibility that the dynamics in the absence of the electron beam may be different. Although electron-sample interactions in LPTEM are not yet fully understood (section 3.3), a great deal can still be learned about the self-assembly dynamics.

Figure 18: Interaction of incoming primary electrons with specimen. **i)** Different signals produced

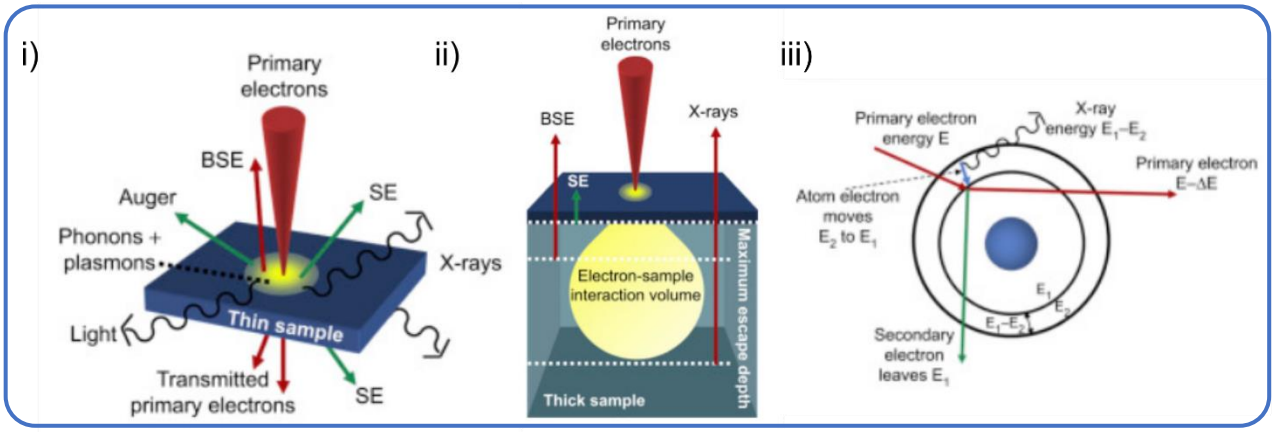

by electron-sample interactions in a thin sample. **ii)** Absorption of electrons in thick samples limits the depth from which these scattered electrons can escape. **iii)** Schematic of secondary electron

and back scattered electron generation. Reproduced with permission from ref ([298]). Copyright 2016 Elsevier.

6.5 Image analysis

A TEM image is a 2D representation of a real object. The object is represented by a matrix of pixels, where each pixel has an x, y coordinate and a corresponding intensity value. High intensity values (lighter pixels) correspond to regions of the detector that interacted strongly with electrons, and low intensity values (darker pixels) correspond to regions that interacted weakly or not at all. Signal is typically captured and digitalized with an electron detector (see sections 7.1) which introduces noise into the image. Poisson noise (shot noise) is signal-dependent and results from the discrete arrival of electron at the detector, while Gaussian noise (white noise) is signal-independent and results from the electronic components of the detector.[572] Signal to noise in TEM is often defined as the average image intensity divided by the standard deviation of the intensities.[573] High signal to noise images are the easiest to visually and computationally analyze. However, many TEM methods applied to molecular self-assembly are dose-limited (Section 7.4). To extract the most information from dose-limited experiments, the images should be collected at the signal to noise limit. Low signal to noise images typically requires image processing, which involves mathematically manipulating the intensity values of the image to aid in visualization or image analysis. Subsequently, image analysis involves extracting quantitative information, such as r measuring the diameter of a particle. Most image processing and analysis methods are not specific to TEM images but are consistent across all types of imaging methods. Several open source and commercial software packages are available for image processing and analysis. ImageJ-FIJI is a popular open source, user-interface based platform with researchers often contributing plugins alongside publications for advanced functionality.[574–577] Additional user-interface platforms include Nion Swift,[578] Gatan DigitalMicrograph, MIPAR,[579] and Relion 3.[580] MATLAB and Python are commonly used for programmatic image processing and have vast

libraries of filters,, segmentation routines, and analysis toolsets. For more information on image processing and analysis, the reader is directed to the following texts.[581–584] Here, we will briefly describe common image processing and analysis methods.

When displaying one-dimensional data, it is important to define y-axis boundaries that enable visualization of the relevant features of the data. The same is true for images, where a colormap with contrast boundaries must be assigned to the data before viewing it. Perceptually linear colormaps should always be used to avoid false boundaries in the image and ensure consistent interpretation.[585] In a typical TEM image, a grayscale colormap will be assigned to the data, with the largest intensity value of the image assigned to a pure white pixel and the smallest intensity values assigned to a pure black pixel. Every intermediate value is assigned a shade of gray based on the linear position between the highest and lowest intensity value. As displayed in Figure 19 i,[586] this method of boundary assignment can result in an image with low object contrast because a small number of outlier pixels (often caused by noise) can cause the majority of the object information to be represented in a small portion of the color axis. In most software, contrast boundaries can be defined manually or adjusted with brightness and contrast. In Figure 19 ii the upper and lower contrast boundaries are defined closer to the mean of the histogram which better highlights the object. However, any information above or below these boundaries is now lost and represented as pure white or pure black pixels. No universal method exists for determining the best contrast boundaries for displaying an image. Most image analysis software includes an auto contrast function which attempts to determine and display the maximum amount of useful information in an image, but ultimately the user must consider which features are highlighted and which are lost upon assigning contrast boundaries.

Image processing is defined as a series of mathematical operations used to highlight features of an image. This is often achieved by filtering the image via matrix convolution. Matrix convolution is accomplished by taking the dot product of a small matrix, called the kernel or convolution matrix,

with every location of the original image to produce a new image. For example, a Sobel filter highlights object edges by identifying intensity gradients via matrix convolution. TEM images are often processed with filters such as the mean filter, median filter, Gaussian filter, and Weiner filter.[587–589]

Images can also be transformed to aid in visualization and analysis. An image transformation involves redefining features of the image on a new set of axes. For example, the Fourier transform (FT) translates the image into frequency space, where periodic features are expressed as bright pixels. This method is commonly used to highlight uniform features present in directional or crystalline materials (see Figure 10 iii and Figure 11 ii).[284] It is also common to apply filters in Fourier space such, as a low pass filter which eliminates high frequency features from the image (such as random noise).[589] Other noteworthy transforms include the Euclidian (distance) transform[590], Hough transform[591], and polar transform[100].

Image analysis is the procedure of extracting quantitative information from a raw or processed image. A common example is to extract the size distribution of objects, for example, the diameter of spherical particles. A basic method is to use line drawing tools, which are common in programs such as ImageJ, and to manually draw a line across each particle of interest. The advantage of this method is that it is quick and easy for measuring a few particles. However, the challenges with this method are that it is time consuming to apply to many particles and that the selection of which particles to measure and where to draw the line is subjective. Another, more quantitative method is to create an intensity profile for each particle and then calculate the diameter based on the full width half maximum (FWHM) of the resulting profile. This method removes the subjectivity of how the diameter is defined but is still time consuming, and particle selection remains subjective. Another approach is to use object segmentation to define which pixels represent object and which pixels represent the background. Once segmented, the user can perform a variety of image analysis procedures on each individual object such as calculating the area of each sphere

and converting this to a diameter, which uses information from the entire object rather than a single slice. Object segmentation can be achieved by a variety of techniques such as Otsu-method thresholding,[588,592] k-means clustering,[590] and active contouring [593–595]. The advantage of segmentation is that it can be fully automated and is therefore less subjective and less time-consuming for large datasets.[586,596] Precise segmentation can be challenging with low signal to noise images,[597] touching or overlapping objects,[598] and/or severe gradients in background illuminations; these scenarios require more complex image processing pipelines before analysis.[599,600] Accurate object segmentation enables data analysis that would be inaccessible with manual techniques, for example, quantifying particle motion,[601,602], particle orientation[130], and particle geometry.[102,103]

At its core, TEM image processing and analysis is a computer vision task, and the techniques described above use traditional algorithms to accomplish these tasks. However, in recent years, Deep Neural Networks (DNN) obtained via Machine Leaning (ML) have successfully produced task-specific models which outperform traditional routines in almost all computer vision tasks.[603] Most ML has been applied to natural images; however, there are some example of TEM specific models for defect characterization[604,605], super-resolution reconstructions[606], and object segmentation.[607–609] Specifically, the U-net model has demonstrated superior object segmentation in inorganic LPTEM self-assembly datasets, with a closed loop process for simulating labeled image data to train the model.[130] ML becomes more useful as the complexity of the objects under investigation increases. Therefore, we expect the continued development of ML models for TEM image analysis to have a great impact on the application of TEM to understanding complex molecular self-assembly.

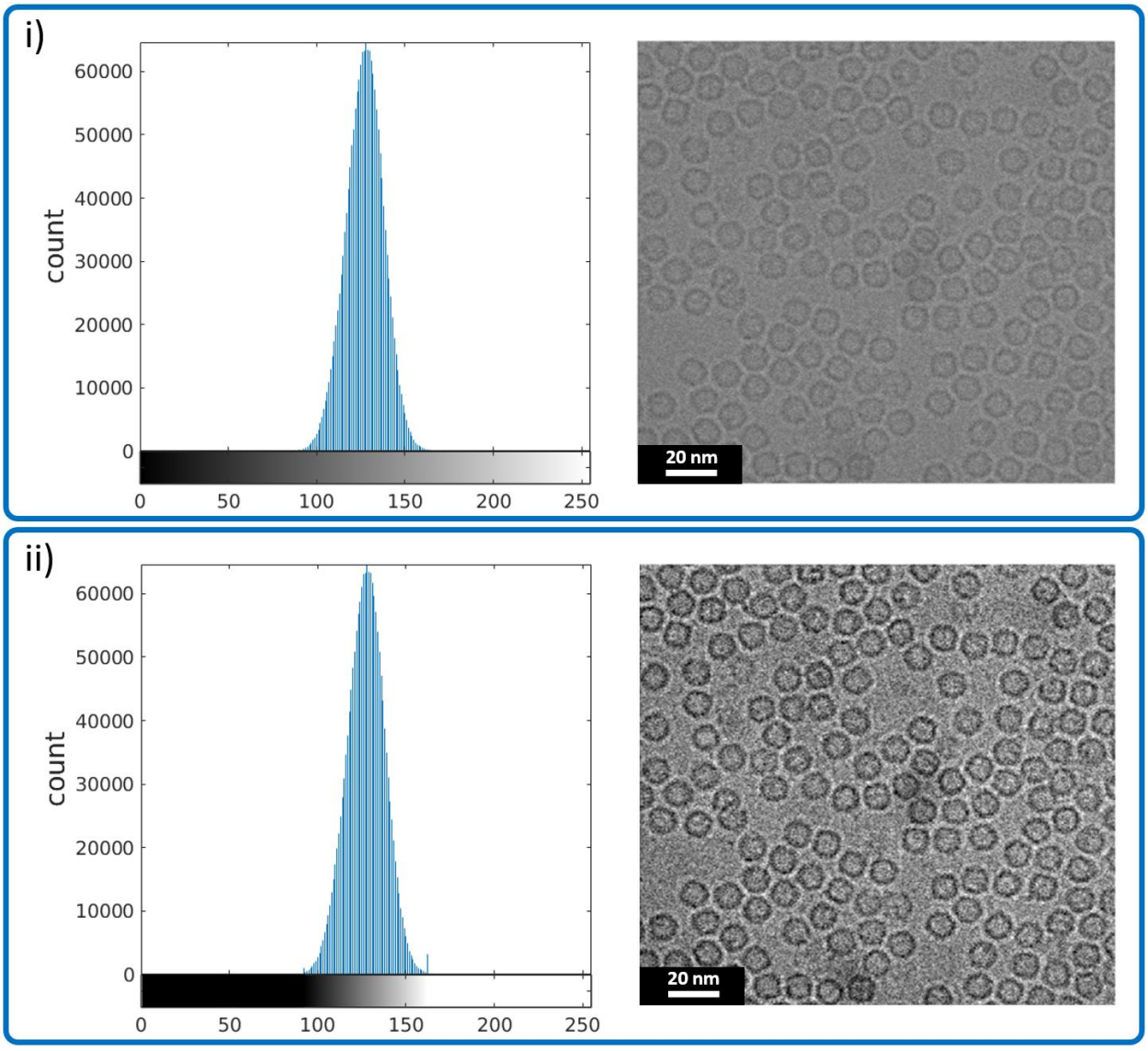

Figure 19: Applying two different sets of contrast boundaries to the same image of virus particles. Reproduced with permission from ref ([586]). Copyright 2019 Springer Nature. **i)** Intensity histogram and resulting image when contrast colormap is scaled linearly between 0 and 255. The majority of the object information is represented in a small portion of the colormap. **ii)** Intensity histogram and resulting image when contrast colormap is scaled linearly between 90 and 160. Every intensity value below 90 is represented as pure black, and every intensity above 160 is pure white.

AUTHOR INFORMATION

Corresponding Author

***** patters3@uci.edu

ACKNOWLEDGMENTS

J.T.M acknowledges the donors of The American Chemical Society Petroleum Research Fund. B.P.C and R.T were supported by the University of California Cancer Research Coordinating Committee grant C21CR2080

Author Biography

Aoon Rizvi: Aoon Rizvi received his B.S. in chemistry at the University of Illinois at Urbana Champaign in 2018 where he worked with Steve Zimmerman to develop stimuli responsive polymeric materials. He is currently a PhD candidate working with Prof. Joseph Patterson at the University of California Irvine. His research interests include studying soft-matter self-assembly using liquid phase TEM, liquid-liquid phase separation in amphiphilic systems and the self-assembly of block copolymers.

Justin T. Mulvey: Justin Mulvey received his B.S. in materials science and engineering from the University of California, Davis in 2019. He is currently a second year PhD student in materials science engineering at the University of California, Irvine, where he is studying molecular self-assembly with Prof. Joseph Patterson. His research interests include block copolymer self-assembly, liquid cell transmission electron microscopy, and quantitative image analysis.

Brooke P. Carpenter: Brooke Carpenter received her undergraduate degree in Polymer Science from the University of Southern Mississippi in 2018. At USM, she worked under Professor Sarah Morgan where her research focused on synthesizing polymers via controlled radical polymerizations for determination of structure/binding interactions with food-based proteins. She is now a third-year chemistry Ph.D. candidate working under the advisement of Prof. Joseph Patterson. Her current research interests include investigating the fundamental mechanisms of protein-metal-organic frameworks for catalytic applications.

Rain Talosig: Rain Talosig received her Bachelor of Science in chemistry from Ithaca College in 2019. She is currently enrolled in the PhD program at the University of California, Irvine under the supervision of Prof. Joseph Patterson. Her research interests involve the nucleation and growth mechanisms of protein-metal-organic frameworks and gaining a better understanding of the factors that lead to polymorph control in MOF systems.

Joseph P. Patterson: Joe Patterson is an Assistant Professor in the Department of Chemistry at the University of California, Irvine. He received his PhD degree in polymer chemistry and self-assembly from the University of Warwick, UK. He completed postdoctoral research at the University of California, San Diego. He also worked in the Laboratory of Materials and Interface Chemistry at the Eindhoven University of Technology, The Netherlands. His research includes the development of new materials through a deep understanding of their structural dynamics. His awards include the Domino/MacroGroupUK Young Polymer Scientist of the Year in 2011, the 2013 Jon Weaver PhD Prize,a Marie Skłodowska-Curie Individual Fellowship in 2017, A Beall Innovation Award in 2020 and an ACS PRF Doctoral New Investigator Award

REFERENCES

(1) Whitesides, G. M.; Grzybowski, B. Self-Assembly at All Scales. *Science* **2002**, *295*, 2418–2421. https://doi.org/10.1126/science.1070821.

(2) Lehn, J.-M. Toward Self-Organization and Complex Matter. *Science* **2002**, *295*, 2400–2403. https://doi.org/10.1126/science.1071063.

(3) Mattia, E.; Otto, S. Supramolecular Systems Chemistry. *Nat. Nanotechnol.* **2015**, *10*, 111–119. https://doi.org/10.1038/nnano.2014.337.

(4) Wales, D. J.; Bogdan, T. V. Potential Energy and Free Energy Landscapes. *J. Phys. Chem. B* **2006**, *110*, 20765–20776. https://doi.org/10.1021/jp0680544.

(5) Palermo, V.; Samorì, P. Molecular Self-Assembly across Multiple Length Scales. *Angew. Chem. Int. Ed.* **2007**, *46*, 4428–4432. https://doi.org/10.1002/anie.200700416.

(6) Frederix, P. W. J. M.; Patmanidis, I.; Marrink, S. J. Molecular Simulations of Self-Assembling Bio-Inspired Supramolecular Systems and Their Connection to Experiments. *Chem. Soc. Rev.* **2018**, *47*, 3470–3489. https://doi.org/10.1039/C8CS00040A.

(7) Barbee, M. H.; Wright, Z. M.; Allen, B. P.; Taylor, H. F.; Patteson, E. F.; Knight, A. S. Protein-Mimetic Self-Assembly with Synthetic Macromolecules. *Macromolecules* **2021**, *54*, 3585–3612. https://doi.org/10.1021/acs.macromol.0c02826.

(8) Whitesides, G. M.; Boncheva, M. Beyond Molecules: Self-Assembly of Mesoscopic and Macroscopic Components. *Proc. Natl. Acad. Sci.* **2002**, *99*, 4769–4774.

(9) Franken, L. E.; Grünewald, K.; Boekema, E. J.; Stuart, M. C. A. A Technical Introduction to Transmission Electron Microscopy for Soft-Matter: Imaging, Possibilities, Choices, and Technical Developments. *Small* **2020**, *16*, 1906198. https://doi.org/10.1002/smll.201906198.

(10) Williams, D. B.; Carter, C. B. The Transmission Electron Microscope. In *Transmission Electron Microscopy: A Textbook for Materials Science*; Williams, D. B., Carter, C. B., Eds.; Springer US: Boston, MA, 2009; pp 3–22. https://doi.org/10.1007/978-0-387-76501-3_1.

(11) Transmission Electron Microscopy for Chemists. *Acc. Chem. Res.* **2017**, *50*, 1795–1796. https://doi.org/10.1021/acs.accounts.7b00318.

(12) Zhou, W.; Kapetanakis, M. D.; Prange, M. P.; Pantelides, S. T.; Pennycook, S. J.; Idrobo, J.-C. Direct Determination of the Chemical Bonding of Individual Impurities in Graphene. *Phys. Rev. Lett.* **2012**, *109*, 206803. https://doi.org/10.1103/PhysRevLett.109.206803.

(13) Egerton, R. F. Radiation Damage to Organic and Inorganic Specimens in the TEM. *Micron* **2019**, *119*, 72–87. https://doi.org/10.1016/j.micron.2019.01.005.

(14) Hargittai, B.; Hargittai, I. Quasicrystal Discovery—From NBS/NIST to Stockholm. In *Science of Crystal Structures: Highlights in Crystallography*; Hargittai, I., Hargittai, B., Eds.; Springer International Publishing: Cham, 2015; pp 137–142. https://doi.org/10.1007/978-3-319-19827-9_15.

(15) Thomas H. Epps, I. I. I.; K. O'Reilly, R. Block Copolymers: Controlling Nanostructure to Generate Functional Materials – Synthesis, Characterization, and Engineering. *Chem. Sci.* **2016**, *7*, 1674–1689. https://doi.org/10.1039/C5SC03505H.

(16) P. Patterson, J.; M. Sanchez, A.; Petzetakis, N.; P. Smart, T.; Thomas H. Epps, I. I. I.; Portman, I.; R. Wilson, N.; K. O'Reilly, R. A Simple Approach to Characterizing Block Copolymer Assemblies: Graphene Oxide Supports for High Contrast Multi-Technique Imaging. *Soft Matter* **2012**, *8*, 3322–3328. https://doi.org/10.1039/C2SM07040E.

(17) Shen, H.; Eisenberg, A. Control of Architecture in Block-Copolymer Vesicles. *Angew. Chem. Int. Ed.* **2000**, *39*, 3310–3312. https://doi.org/10.1002/1521-3773(20000915)39:18<3310::AID-ANIE3310>3.0.CO;2-2.

(18) Li, T.; Nowell, C. J.; Cipolla, D.; Rades, T.; Boyd, B. J. Direct Comparison of Standard Transmission Electron Microscopy and Cryogenic-TEM in Imaging Nanocrystals Inside Liposomes. *Mol. Pharm.* **2019**, *16*, 1775–1781. https://doi.org/10.1021/acs.molpharmaceut.8b01308.
(19) Wang, X.; Guerin, G.; Wang, H.; Wang, Y.; Manners, I.; Winnik, M. A. Cylindrical Block Copolymer Micelles and Co-Micelles of Controlled Length and Architecture. *Science* **2007**, *317*, 644–647. https://doi.org/10.1126/science.1141382.
(20) Luo, L.; Eisenberg, A. Thermodynamic Size Control of Block Copolymer Vesicles in Solution. *Langmuir* **2001**, *17*, 6804–6811. https://doi.org/10.1021/la0104370.
(21) Hong, F.; Zhang, F.; Liu, Y.; Yan, H. DNA Origami: Scaffolds for Creating Higher Order Structures. *Chem. Rev.* **2017**, *117*, 12584–12640. https://doi.org/10.1021/acs.chemrev.6b00825.
(22) Douglas, S. M.; Dietz, H.; Liedl, T.; Högberg, B.; Graf, F.; Shih, W. M. Self-Assembly of DNA into Nanoscale Three-Dimensional Shapes. *Nature* **2009**, *459*, 414–418. https://doi.org/10.1038/nature08016.
(23) Lei, D.; Marras, A. E.; Liu, J.; Huang, C.-M.; Zhou, L.; Castro, C. E.; Su, H.-J.; Ren, G. Three-Dimensional Structural Dynamics of DNA Origami Bennett Linkages Using Individual-Particle Electron Tomography. *Nat. Commun.* **2018**, *9*, 592. https://doi.org/10.1038/s41467-018-03018-0.
(24) Andersen, E. S.; Dong, M.; Nielsen, M. M.; Jahn, K.; Subramani, R.; Mamdouh, W.; Golas, M. M.; Sander, B.; Stark, H.; Oliveira, C. L. P.; Pedersen, J. S.; Birkedal, V.; Besenbacher, F.; Gothelf, K. V.; Kjems, J. Self-Assembly of a Nanoscale DNA Box with a Controllable Lid. *Nature* **2009**, *459*, 73–76. https://doi.org/10.1038/nature07971.
(25) Wiktor, C.; Meledina, M.; Turner, S.; Lebedev, O. I.; Fischer, R. A. Transmission Electron Microscopy on Metal–Organic Frameworks – a Review. *J. Mater. Chem. A* **2017**, *5*, 14969–14989. https://doi.org/10.1039/C7TA00194K.
(26) Li, P.-Z.; Su, J.; Liang, J.; Liu, J.; Zhang, Y.; Chen, H.; Zhao, Y. A Highly Porous Metal–Organic Framework for Large Organic Molecule Capture and Chromatographic Separation. *Chem. Commun.* **2017**, *53*, 3434–3437. https://doi.org/10.1039/C7CC01063J.
(27) Liu, L.; Zhang, D.; Zhu, Y.; Han, Y. Bulk and Local Structures of Metal–Organic Frameworks Unravelled by High-Resolution Electron Microscopy. *Commun. Chem.* **2020**, *3*, 1–14. https://doi.org/10.1038/s42004-020-00361-6.
(28) Shi, Y.; Pan, L.; Liu, B.; Wang, Y.; Cui, Y.; Bao, Z.; Yu, G. Nanostructured Conductive Polypyrrole Hydrogels as High-Performance, Flexible Supercapacitor Electrodes. *J. Mater. Chem. A* **2014**, *2*, 6086–6091. https://doi.org/10.1039/C4TA00484A.
(29) Chuang, V. P.; Gwyther, J.; Mickiewicz, R. A.; Manners, I.; Ross, C. A. Templated Self-Assembly of Square Symmetry Arrays from an ABC Triblock Terpolymer. *Nano Lett.* **2009**, *9*, 4364–4369. https://doi.org/10.1021/nl902646e.
(30) Hest, J. C. M. van; Delnoye, D. a. P.; Baars, M. W. P. L.; Genderen, M. H. P. van; Meijer, E. W. Polystyrene-Dendrimer Amphiphilic Block Copolymers with a Generation-Dependent Aggregation. *Science* **1995**, *268*, 1592–1595. https://doi.org/10.1126/science.268.5217.1592.
(31) Shim, J.; Bates, F. S.; Lodge, T. P. Superlattice by Charged Block Copolymer Self-Assembly. *Nat. Commun.* **2019**, *10*, 2108. https://doi.org/10.1038/s41467-019-10141-z.
(32) Khandpur, A. K.; Foerster, S.; Bates, F. S.; Hamley, I. W.; Ryan, A. J.; Bras, W.; Almdal, K.; Mortensen, K. Polyisoprene-Polystyrene Diblock Copolymer Phase Diagram near the Order-Disorder Transition. *Macromolecules* **1995**, *28*, 8796–8806. https://doi.org/10.1021/ma00130a012.
(33) Foerster, S.; Khandpur, A. K.; Zhao, J.; Bates, F. S.; Hamley, I. W.; Ryan, A. J.; Bras, W. Complex Phase Behavior of Polyisoprene-Polystyrene Diblock Copolymers Near the Order-Disorder Transition. *Macromolecules* **1994**, *27*, 6922–6935. https://doi.org/10.1021/ma00101a033.

(34) Harris, P. J. F. Transmission Electron Microscopy of Carbon: A Brief History. *C* **2018**, *4*, 4. https://doi.org/10.3390/c4010004.
(35) Haedler, A. T.; Meskers, S. C. J.; Zha, R. H.; Kivala, M.; Schmidt, H.-W.; Meijer, E. W. Pathway Complexity in the Enantioselective Self-Assembly of Functional Carbonyl-Bridged Triarylamine Trisamides. *J. Am. Chem. Soc.* **2016**, *138*, 10539–10545. https://doi.org/10.1021/jacs.6b05184.
(36) Cornelissen, J. J. L. M.; Rowan, A. E.; Nolte, R. J. M.; Sommerdijk, N. A. J. M. Chiral Architectures from Macromolecular Building Blocks. *Chem. Rev.* **2001**, *101*, 4039–4070. https://doi.org/10.1021/cr990126i.
(37) Edwards-Gayle, C. J. C.; Hamley, I. W. Self-Assembly of Bioactive Peptides, Peptide Conjugates, and Peptide Mimetic Materials. *Org. Biomol. Chem.* **2017**, *15*, 5867–5876. https://doi.org/10.1039/C7OB01092C.
(38) Hartgerink, J. D.; Beniash, E.; Stupp, S. I. Self-Assembly and Mineralization of Peptide-Amphiphile Nanofibers. *Science* **2001**, *294*, 1684–1688. https://doi.org/10.1126/science.1063187.
(39) Hartgerink, J. D.; Beniash, E.; Stupp, S. I. Peptide-Amphiphile Nanofibers: A Versatile Scaffold for the Preparation of Self-Assembling Materials. *Proc. Natl. Acad. Sci.* **2002**, *99*, 5133–5138. https://doi.org/10.1073/pnas.072699999.
(40) Pashuck, E. T.; Cui, H.; Stupp, S. I. Tuning Supramolecular Rigidity of Peptide Fibers through Molecular Structure. *J. Am. Chem. Soc.* **2010**, *132*, 6041–6046. https://doi.org/10.1021/ja908560n.
(41) Han, D.; Pal, S.; Liu, Y.; Yan, H. Folding and Cutting DNA into Reconfigurable Topological Nanostructures. *Nat. Nanotechnol.* **2010**, *5*, 712–717. https://doi.org/10.1038/nnano.2010.193.
(42) Dietz, H.; Douglas, S. M.; Shih, W. M. Folding DNA into Twisted and Curved Nanoscale Shapes. *Science* **2009**, *325*, 725–730. https://doi.org/10.1126/science.1174251.
(43) Blanazs, A.; Ryan, A. J.; Armes, S. P. Predictive Phase Diagrams for RAFT Aqueous Dispersion Polymerization: Effect of Block Copolymer Composition, Molecular Weight, and Copolymer Concentration. *Macromolecules* **2012**, *45*, 5099–5107. https://doi.org/10.1021/ma301059r.
(44) Blackman, L. D.; Doncom, K. E. B.; Gibson, M. I.; O'Reilly, R. K. Comparison of Photo- and Thermally Initiated Polymerization-Induced Self-Assembly: A Lack of End Group Fidelity Drives the Formation of Higher Order Morphologies. *Polym. Chem.* **2017**, *8*, 2860–2871. https://doi.org/10.1039/C7PY00407A.
(45) Paula Vena, M.; Moor, D. de; Ianiro, A.; Tuinier, R.; P. Patterson, J. Kinetic State Diagrams for a Highly Asymmetric Block Copolymer Assembled in Solution. *Soft Matter* **2021**, *17*, 1084–1090. https://doi.org/10.1039/D0SM01596B.
(46) Deria, P.; Von Bargen, C. D.; Olivier, J.-H.; Kumbhar, A. S.; Saven, J. G.; Therien, M. J. Single-Handed Helical Wrapping of Single-Walled Carbon Nanotubes by Chiral, Ionic, Semiconducting Polymers. *J. Am. Chem. Soc.* **2013**, *135*, 16220–16234. https://doi.org/10.1021/ja408430v.
(47) Petzetakis, N.; P. Dove, A.; K. O'Reilly, R. Cylindrical Micelles from the Living Crystallization-Driven Self-Assembly of Poly(Lactide)-Containing Block Copolymers. *Chem. Sci.* **2011**, *2*, 955–960. https://doi.org/10.1039/C0SC00596G.
(48) Finnegan, J. R.; He, X.; Street, S. T. G.; Garcia-Hernandez, J. D.; Hayward, D. W.; Harniman, R. L.; Richardson, R. M.; Whittell, G. R.; Manners, I. Extending the Scope of "Living" Crystallization-Driven Self-Assembly: Well-Defined 1D Micelles and Block Comicelles from Crystallizable Polycarbonate Block Copolymers. *J. Am. Chem. Soc.* **2018**, *140*, 17127–17140. https://doi.org/10.1021/jacs.8b09861.
(49) Pitto-Barry, A.; Kirby, N.; Dove, A. P.; O'Reilly, R. K. Expanding the Scope of the Crystallization-Driven Self-Assembly of Polylactide-Containing Polymers. *Polym. Chem.* **2014**, *5*, 1427–1436. https://doi.org/10.1039/C3PY01048A.
(50) Yashima, E.; Ousaka, N.; Taura, D.; Shimomura, K.; Ikai, T.; Maeda, K. Supramolecular Helical Systems: Helical Assemblies of Small Molecules, Foldamers, and Polymers with Chiral Amplification

and Their Functions. *Chem. Rev.* **2016**, *116*, 13752–13990. https://doi.org/10.1021/acs.chemrev.6b00354.
(51) Oda, R.; Huc, I.; Schmutz, M.; Candau, S. J.; MacKintosh, F. C. Tuning Bilayer Twist Using Chiral Counterions. *Nature* **1999**, *399*, 566–569. https://doi.org/10.1038/21154.
(52) Blanazs, A.; Madsen, J.; Battaglia, G.; Ryan, A. J.; Armes, S. P. Mechanistic Insights for Block Copolymer Morphologies: How Do Worms Form Vesicles? *J. Am. Chem. Soc.* **2011**, *133*, 16581–16587. https://doi.org/10.1021/ja206301a.
(53) Koshino, M.; Niimi, Y.; Nakamura, E.; Kataura, H.; Okazaki, T.; Suenaga, K.; Iijima, S. Analysis of the Reactivity and Selectivity of Fullerene Dimerization Reactions at the Atomic Level. *Nat. Chem.* **2010**, *2*, 117–124. https://doi.org/10.1038/nchem.482.
(54) Li, Y.; Huang, W.; Li, Y.; Chiu, W.; Cui, Y. Opportunities for Cryogenic Electron Microscopy in Materials Science and Nanoscience. *ACS Nano* **2020**, *14*, 9263–9276. https://doi.org/10.1021/acsnano.0c05020.
(55) Friedrich, H.; Frederik, P. M.; de With, G.; Sommerdijk, N. A. J. M. Imaging of Self-Assembled Structures: Interpretation of TEM and Cryo-TEM Images. *Angew. Chem. Int. Ed.* **2010**, *49*, 7850–7858. https://doi.org/10.1002/anie.201001493.
(56) Patterson, J. P.; Xu, Y.; Moradi, M.-A.; Sommerdijk, N. A. J. M.; Friedrich, H. CryoTEM as an Advanced Analytical Tool for Materials Chemists. *Acc. Chem. Res.* **2017**, *50*, 1495–1501. https://doi.org/10.1021/acs.accounts.7b00107.
(57) Bellare, J. R.; Davis, H. T.; Scriven, L. E.; Talmon, Y. Controlled Environment Vitrification System: An Improved Sample Preparation Technique. *J. Electron Microsc. Tech.* **1988**, *10*, 87–111. https://doi.org/10.1002/jemt.1060100111.
(58) Wirix, M. J. M.; Bomans, P. H. H.; Friedrich, H.; Sommerdijk, N. A. J. M.; de With, G. Three-Dimensional Structure of P3HT Assemblies in Organic Solvents Revealed by Cryo-TEM. *Nano Lett.* **2014**, *14*, 2033–2038. https://doi.org/10.1021/nl5001967.
(59) Kim, K. T.; Zhu, J.; Meeuwissen, S. A.; Cornelissen, J. J. L. M.; Pochan, D. J.; Nolte, R. J. M.; van Hest, J. C. M. Polymersome Stomatocytes: Controlled Shape Transformation in Polymer Vesicles. *J. Am. Chem. Soc.* **2010**, *132*, 12522–12524. https://doi.org/10.1021/ja104154t.
(60) Cui, H.; Hodgdon, T. K.; Kaler, E. W.; Abezgauz, L.; Danino, D.; Lubovsky, M.; Talmon, Y.; Pochan, D. J. Elucidating the Assembled Structure of Amphiphiles in Solution via Cryogenic Transmission Electron Microscopy. *Soft Matter* **2007**, *3*, 945–955. https://doi.org/10.1039/B704194B.
(61) Frederik, P. M.; Sommerdijk, N. Spatial and Temporal Resolution in Cryo-Electron Microscopy—A Scope for Nano-Chemistry. *Curr. Opin. Colloid Interface Sci.* **2005**, *10*, 245–249. https://doi.org/10.1016/j.cocis.2005.09.018.
(62) Dandey, V. P.; Budell, W. C.; Wei, H.; Bobe, D.; Maruthi, K.; Kopylov, M.; Eng, E. T.; Kahn, P. A.; Hinshaw, J. E.; Kundu, N.; Nimigean, C. M.; Fan, C.; Sukomon, N.; Darst, S. A.; Saecker, R. M.; Chen, J.; Malone, B.; Potter, C. S.; Carragher, B. Time-Resolved Cryo-EM Using Spotiton. *Nat. Methods* **2020**, *17*, 897–900. https://doi.org/10.1038/s41592-020-0925-6.
(63) Li, Y.; Wang, K.; Zhou, W.; Li, Y.; Vila, R.; Huang, W.; Wang, H.; Chen, G.; Wu, G.-H.; Tsao, Y.; Wang, H.; Sinclair, R.; Chiu, W.; Cui, Y. Cryo-EM Structures of Atomic Surfaces and Host-Guest Chemistry in Metal-Organic Frameworks. *Matter* **2019**, *1*, 428–438. https://doi.org/10.1016/j.matt.2019.06.001.
(64) Henderson, R.; Baldwin, J. M.; Ceska, T. A.; Zemlin, F.; Beckmann, E.; Downing, K. H. Model for the Structure of Bacteriorhodopsin Based on High-Resolution Electron Cryo-Microscopy. *J. Mol. Biol.* **1990**, *213*, 899–929. https://doi.org/10.1016/S0022-2836(05)80271-2.
(65) Nogales, E. Profile of Joachim Frank, Richard Henderson, and Jacques Dubochet, 2017 Nobel Laureates in Chemistry. *Proc. Natl. Acad. Sci.* **2018**, *115*, 441–444. https://doi.org/10.1073/pnas.1718898114.

(66) Lepault, J.; Booy, F. P.; Dubochet, J. Electron Microscopy of Frozen Biological Suspensions. *J. Microsc.* **1983**, *129*, 89–102. https://doi.org/10.1111/j.1365-2818.1983.tb04163.x.
(67) Böttcher, B.; Wynne, S. A.; Crowther, R. A. Determination of the Fold of the Core Protein of Hepatitis B Virus by Electron Cryomicroscopy. *Nature* **1997**, *386*, 88–91. https://doi.org/10.1038/386088a0.
(68) Yu, X.; Jin, L.; Zhou, Z. H. 3.88 Å Structure of Cytoplasmic Polyhedrosis Virus by Cryo-Electron Microscopy. *Nature* **2008**, *453*, 415–419. https://doi.org/10.1038/nature06893.
(69) Jiang, W.; Baker, M. L.; Jakana, J.; Weigele, P. R.; King, J.; Chiu, W. Backbone Structure of the Infectious E15 Virus Capsid Revealed by Electron Cryomicroscopy. *Nature* **2008**, *451*, 1130–1134. https://doi.org/10.1038/nature06665.
(70) Zhang, X.; Settembre, E.; Xu, C.; Dormitzer, P. R.; Bellamy, R.; Harrison, S. C.; Grigorieff, N. From the Cover: Near-Atomic Resolution Using Electron Cryomicroscopy and Single-Particle Reconstruction. *Proc. Natl. Acad. Sci. U. S. A.* **2008**, *105*, 1867. https://doi.org/10.1073/pnas.0711623105.
(71) Nakane, T.; Kotecha, A.; Sente, A.; McMullan, G.; Masiulis, S.; Brown, P. M. G. E.; Grigoras, I. T.; Malinauskaite, L.; Malinauskas, T.; Miehling, J.; Uchański, T.; Yu, L.; Karia, D.; Pechnikova, E. V.; de Jong, E.; Keizer, J.; Bischoff, M.; McCormack, J.; Tiemeijer, P.; Hardwick, S. W.; Chirgadze, D. Y.; Murshudov, G.; Aricescu, A. R.; Scheres, S. H. W. Single-Particle Cryo-EM at Atomic Resolution. *Nature* **2020**, *587*, 152–156. https://doi.org/10.1038/s41586-020-2829-0.
(72) Hud, N. V.; Downing, K. H. Cryoelectron Microscopy of λ Phage DNA Condensates in Vitreous Ice: The Fine Structure of DNA Toroids. *Proc. Natl. Acad. Sci.* **2001**, *98*, 14925–14930. https://doi.org/10.1073/pnas.261560398.
(73) Xuan, S.; Jiang, X.; Spencer, R. K.; Li, N. K.; Prendergast, D.; Balsara, N. P.; Zuckermann, R. N. Atomic-Level Engineering and Imaging of Polypeptoid Crystal Lattices. *Proc. Natl. Acad. Sci.* **2019**, *116*, 22491–22499.
(74) Jiang, X.; Xuan, S.; Kundu, J.; Prendergast, D.; N. Zuckermann, R.; P. Balsara, N. Effect of Processing and End Groups on the Crystal Structure of Polypeptoids Studied by Cryogenic Electron Microscopy at Atomic Length Scales. *Soft Matter* **2019**, *15*, 4723–4736. https://doi.org/10.1039/C9SM00633H.
(75) Jiang, X.; Spencer, R. K.; Sun, J.; Ophus, C.; Zuckermann, R. N.; Downing, K. H.; Balsara, N. P. Resolving the Morphology of Peptoid Vesicles at the 1 Nm Length Scale Using Cryogenic Electron Microscopy. *J. Phys. Chem. B* **2019**, *123*, 1195–1205. https://doi.org/10.1021/acs.jpcb.8b11752.
(76) Schade, B.; Ludwig, K.; Böttcher, C.; Hartnagel, U.; Hirsch, A. Supramolecular Structure of 5-Nm Spherical Micelles with D3 Symmetry Assembled from Amphiphilic [3:3]-Hexakis Adducts of C60. *Angew. Chem. Int. Ed.* **2007**, *46*, 4393–4396. https://doi.org/10.1002/anie.200604784.
(77) Bai, X.; McMullan, G.; Scheres, S. H. W. How Cryo-EM Is Revolutionizing Structural Biology. *Trends Biochem. Sci.* **2015**, *40*, 49–57. https://doi.org/10.1016/j.tibs.2014.10.005.
(78) Li, Z.; Kesselman, E.; Talmon, Y.; Hillmyer, M. A.; Lodge, T. P. Multicompartment Micelles from ABC Miktoarm Stars in Water. *Science* **2004**, *306*, 98. https://doi.org/10.1126/science.1103350.
(79) Mortensen, K.; Talmon, Y. Cryo-TEM and SANS Microstructural Study of Pluronic Polymer Solutions. *Macromolecules* **1995**, *28*, 8829–8834. https://doi.org/10.1021/ma00130a016.
(80) Jung, H.-T.; Lee, S. Y.; Kaler, E. W.; Coldren, B.; Zasadzinski, J. A. Gaussian Curvature and the Equilibrium among Bilayer Cylinders, Spheres, and Discs. *Proc. Natl. Acad. Sci.* **2002**, *99*, 15318–15322. https://doi.org/10.1073/pnas.242374499.
(81) He, Y.; Li, Z.; Simone, P.; Lodge, T. P. Self-Assembly of Block Copolymer Micelles in an Ionic Liquid. *J. Am. Chem. Soc.* **2006**, *128*, 2745–2750. https://doi.org/10.1021/ja058091t.
(82) Danino, D.; Talmon, Y.; Levy, H.; Beinert, G.; Zana, R. Branched Threadlike Micelles in an Aqueous Solution of a Trimeric Surfactant. *Science* **1995**, *269*, 1420–1421. https://doi.org/10.1126/science.269.5229.1420.

(83) Jain, S.; Bates, F. S. On the Origins of Morphological Complexity in Block Copolymer Surfactants. *Science* **2003**, *300*, 460–464. https://doi.org/10.1126/science.1082193.
(84) Bonini, M.; Rossi, S.; Karlsson, G.; Almgren, M.; Lo Nostro, P.; Baglioni, P. Self-Assembly of β-Cyclodextrin in Water. Part 1: Cryo-TEM and Dynamic and Static Light Scattering. *Langmuir* **2006**, *22*, 1478–1484. https://doi.org/10.1021/la052878f.
(85) High Elongation of Polyelectrolyte Chains in the Osmotic Limit of Spherical Polyelectrolyte Brushes: A Study by Cryogenic Transmission Electron Microscopy | Journal of the American Chemical Society https://pubs.acs.org/doi/10.1021/ja0513234 (accessed 2020 -12 -03).
(86) Tidhar, Y.; Weissman, H.; Tworowski, D.; Rybtchinski, B. Mechanism of Crystalline Self-Assembly in Aqueous Medium: A Combined Cryo-TEM/Kinetic Study. *Chem. – Eur. J.* **2014**, *20*, 10332–10342. https://doi.org/10.1002/chem.201402096.
(87) Ziserman, L.; Lee, H.-Y.; Raghavan, S. R.; Mor, A.; Danino, D. Unraveling the Mechanism of Nanotube Formation by Chiral Self-Assembly of Amphiphiles. *J. Am. Chem. Soc.* **2011**, *133*, 2511–2517. https://doi.org/10.1021/ja107069f.
(88) McKenzie, B. E.; Visser, J. F. de; Portale, G.; Hermida-Merino, D.; Friedrich, H.; Bomans, P. H. H.; Bras, W.; Monaghan, O. R.; Holder, S. J.; Sommerdijk, N. a. J. M. The Evolution of Bicontinuous Polymeric Nanospheres in Aqueous Solution. *Soft Matter* **2016**, *12*, 4113–4122. https://doi.org/10.1039/C6SM00053C.
(89) Yu, S.; Azzam, T.; Rouiller, I.; Eisenberg, A. "Breathing" Vesicles. *J. Am. Chem. Soc.* **2009**, *131*, 10557–10566. https://doi.org/10.1021/ja902869q.
(90) Ruthstein, S.; Schmidt, J.; Kesselman, E.; Talmon, Y.; Goldfarb, D. Resolving Intermediate Solution Structures during the Formation of Mesoporous SBA-15. *J. Am. Chem. Soc.* **2006**, *128*, 3366–3374. https://doi.org/10.1021/ja0559911.
(91) Wu, H.; Friedrich, H.; Patterson, J. P.; Sommerdijk, N. A. J. M.; Jonge, N. de. Liquid-Phase Electron Microscopy for Soft Matter Science and Biology. *Adv. Mater.* **2020**, *32*, 2001582. https://doi.org/10.1002/adma.202001582.
(92) de Jonge, N.; Ross, F. M. Electron Microscopy of Specimens in Liquid. *Nat. Nanotechnol.* **2011**, *6*, 695–704. https://doi.org/10.1038/nnano.2011.161.
(93) Ruska, E. Beitrag zur übermikroskopischen Abbildung bei höheren Drucken. *Kolloid-Z.* **1942**, *100*, 212–219. https://doi.org/10.1007/BF01519549.
(94) Kröger, R.; Verch, A. Liquid Cell Transmission Electron Microscopy and the Impact of Confinement on the Precipitation from Supersaturated Solutions. *Minerals* **2018**, *8*, 21. https://doi.org/10.3390/min8010021.
(95) Moser, T. H.; Shokuhfar, T.; Evans, J. E. Considerations for Imaging Thick, Low Contrast, and Beam Sensitive Samples with Liquid Cell Transmission Electron Microscopy. *Micron* **2019**, *117*, 8–15. https://doi.org/10.1016/j.micron.2018.10.007.
(96) Moser, T. H.; Mehta, H.; Park, C.; Kelly, R. T.; Shokuhfar, T.; Evans, J. E. The Role of Electron Irradiation History in Liquid Cell Transmission Electron Microscopy. *Sci. Adv.* **2018**, *4*, eaaq1202. https://doi.org/10.1126/sciadv.aaq1202.
(97) Schneider, N. M.; Norton, M. M.; Mendel, B. J.; Grogan, J. M.; Ross, F. M.; Bau, H. H. Electron–Water Interactions and Implications for Liquid Cell Electron Microscopy. *J. Phys. Chem. C* **2014**, *118*, 22373–22382. https://doi.org/10.1021/jp507400n.
(98) Parent, L. R.; Bakalis, E.; Proetto, M.; Li, Y.; Park, C.; Zerbetto, F.; Gianneschi, N. C. Tackling the Challenges of Dynamic Experiments Using Liquid-Cell Transmission Electron Microscopy. *Acc. Chem. Res.* **2018**, *51*, 3–11. https://doi.org/10.1021/acs.accounts.7b00331.
(99) Patterson, J. P.; Abellan, P.; Denny, M. S.; Park, C.; Browning, N. D.; Cohen, S. M.; Evans, J. E.; Gianneschi, N. C. Observing the Growth of Metal–Organic Frameworks by in Situ Liquid Cell

Transmission Electron Microscopy. *J. Am. Chem. Soc.* **2015**, *137*, 7322–7328. https://doi.org/10.1021/jacs.5b00817.

(100) Ianiro, A.; Wu, H.; van Rijt, M. M. J.; Vena, M. P.; Keizer, A. D. A.; Esteves, A. C. C.; Tuinier, R.; Friedrich, H.; Sommerdijk, N. A. J. M.; Patterson, J. P. Liquid–Liquid Phase Separation during Amphiphilic Self-Assembly. *Nat. Chem.* **2019**, *11*, 320–328. https://doi.org/10.1038/s41557-019-0210-4.

(101) Touve, M. A.; Figg, C. A.; Wright, D. B.; Park, C.; Cantlon, J.; Sumerlin, B. S.; Gianneschi, N. C. Polymerization-Induced Self-Assembly of Micelles Observed by Liquid Cell Transmission Electron Microscopy. *ACS Cent. Sci.* **2018**, *4*, 543–547. https://doi.org/10.1021/acscentsci.8b00148.

(102) Parent, L. R.; Bakalis, E.; Ramírez-Hernández, A.; Kammeyer, J. K.; Park, C.; de Pablo, J.; Zerbetto, F.; Patterson, J. P.; Gianneschi, N. C. Directly Observing Micelle Fusion and Growth in Solution by Liquid-Cell Transmission Electron Microscopy. *J. Am. Chem. Soc.* **2017**, *139*, 17140–17151. https://doi.org/10.1021/jacs.7b09060.

(103) Early, J. T.; Yager, K. G.; Lodge, T. P. Direct Observation of Micelle Fragmentation via In Situ Liquid-Phase Transmission Electron Microscopy. *ACS Macro Lett.* **2020**, *9*, 756–761. https://doi.org/10.1021/acsmacrolett.0c00273.

(104) Li, C.; Tho, C. C.; Galaktionova, D.; Chen, X.; Král, P.; Mirsaidov, U. Dynamics of Amphiphilic Block Copolymers in an Aqueous Solution: Direct Imaging of Micelle Formation and Nanoparticle Encapsulation. *Nanoscale* **2019**, *11*, 2299–2305. https://doi.org/10.1039/C8NR08922A.

(105) Nagamanasa, K. H.; Wang, H.; Granick, S. Liquid-Cell Electron Microscopy of Adsorbed Polymers. *Adv. Mater.* **2017**, *29*, 1703555. https://doi.org/10.1002/adma.201703555.

(106) Mansfeld, U.; Hoeppener, S.; Schubert, U. S. Investigating the Motion of Diblock Copolymer Assemblies in Ionic Liquids by In Situ Electron Microscopy. *Adv. Mater.* **2013**, *25*, 761–765. https://doi.org/10.1002/adma.201203423.

(107) Touve, M. A.; Carlini, A. S.; Gianneschi, N. C. Self-Assembling Peptides Imaged by Correlated Liquid Cell Transmission Electron Microscopy and MALDI-Imaging Mass Spectrometry. *Nat. Commun.* **2019**, *10*, 4837. https://doi.org/10.1038/s41467-019-12660-1.

(108) Smith, J. W.; Chen, Q. Liquid-Phase Electron Microscopy Imaging of Cellular and Biomolecular Systems. *J. Mater. Chem. B* **2020**, *8*, 8490–8506. https://doi.org/10.1039/D0TB01300E.

(109) DiMemmo, L. M.; Varano, A. C.; Haulenbeek, J.; Liang, Y.; Patel, K.; Dukes, M. J.; Zheng, S.; Hubert, M.; Piccoli, S. P.; Kelly, D. F. Real-Time Observation of Protein Aggregates in Pharmaceutical Formulations Using Liquid Cell Electron Microscopy. *Lab. Chip* **2017**, *17*, 315–322. https://doi.org/10.1039/C6LC01160H.

(110) Wang, C.; Qiao, Q.; Shokuhfar, T.; Klie, R. F. High-Resolution Electron Microscopy and Spectroscopy of Ferritin in Biocompatible Graphene Liquid Cells and Graphene Sandwiches. *Adv. Mater.* **2014**, *26*, 3410–3414. https://doi.org/10.1002/adma.201306069.

(111) Yamazaki, T.; Kimura, Y.; Vekilov, P. G.; Furukawa, E.; Shirai, M.; Matsumoto, H.; Driessche, A. E. S. V.; Tsukamoto, K. Two Types of Amorphous Protein Particles Facilitate Crystal Nucleation. *Proc. Natl. Acad. Sci.* **2017**. https://doi.org/10.1073/pnas.1606948114.

(112) Smith, B. J.; Parent, L. R.; Overholts, A. C.; Beaucage, P. A.; Bisbey, R. P.; Chavez, A. D.; Hwang, N.; Park, C.; Evans, A. M.; Gianneschi, N. C.; Dichtel, W. R. Colloidal Covalent Organic Frameworks. *ACS Cent. Sci.* **2017**, *3*, 58–65. https://doi.org/10.1021/acscentsci.6b00331.

(113) Lyu, J.; Gong, X.; Lee, S.-J.; Gnanasekaran, K.; Zhang, X.; Wasson, M. C.; Wang, X.; Bai, P.; Guo, X.; Gianneschi, N. C.; Farha, O. K. Phase Transitions in Metal–Organic Frameworks Directly Monitored through In Situ Variable Temperature Liquid-Cell Transmission Electron Microscopy and In Situ X-Ray Diffraction. *J. Am. Chem. Soc.* **2020**, *142*, 4609–4615. https://doi.org/10.1021/jacs.0c00542.

(114) Wang, H.; Li, B.; Kim, Y.-J.; Kwon, O.-H.; Granick, S. Intermediate States of Molecular Self-Assembly from Liquid-Cell Electron Microscopy. *Proc. Natl. Acad. Sci.* **2020**, *117*, 1283–1292. https://doi.org/10.1073/pnas.1916065117.

(115) Gnanasekaran, K.; Chang, H.; Smeets, P. J. M.; Korpanty, J.; Geiger, F. M.; Gianneschi, N. C. In Situ Ni2+ Stain for Liposome Imaging by Liquid-Cell Transmission Electron Microscopy. *Nano Lett.* **2020**, *20*, 4292–4297. https://doi.org/10.1021/acs.nanolett.0c00898.

(116) Piffoux, M.; Ahmad, N.; Nelayah, J.; Wilhelm, C.; Silva, A.; Gazeau, F.; Alloyeau, D. Monitoring the Dynamics of Cell-Derived Extracellular Vesicles at the Nanoscale by Liquid-Cell Transmission Electron Microscopy. *Nanoscale* **2018**, *10*, 1234–1244. https://doi.org/10.1039/C7NR07576F.

(117) Scheutz, G. M.; Touve, M. A.; Carlini, A. S.; Garrison, J. B.; Gnanasekaran, K.; Sumerlin, B. S.; Gianneschi, N. C. Probing Thermoresponsive Polymerization-Induced Self-Assembly with Variable-Temperature Liquid-Cell Transmission Electron Microscopy. *Matter* **2021**, *4*, 722–736. https://doi.org/10.1016/j.matt.2020.11.017.

(118) Patterson, J. P.; Parent, L. R.; Cantlon, J.; Eickhoff, H.; Bared, G.; Evans, J. E.; Gianneschi, N. C. Picoliter Drop-On-Demand Dispensing for Multiplex Liquid Cell Transmission Electron Microscopy. *Microsc. Microanal.* **2016**, *22*, 507–514. https://doi.org/10.1017/S1431927616000659.

(119) Stawski, T. M.; Roncal-Herrero, T.; Fernandez-Martinez, A.; Matamoros-Veloza, A.; Kröger, R.; Benning, L. G. "On Demand" Triggered Crystallization of CaCO3 from Solute Precursor Species Stabilized by the Water-in-Oil Microemulsion. *Phys. Chem. Chem. Phys.* **2018**, *20*, 13825–13835. https://doi.org/10.1039/C8CP00540K.

(120) Barnhill, S. A.; Bell, N. C.; Patterson, J. P.; Olds, D. P.; Gianneschi, N. C. Phase Diagrams of Polynorbornene Amphiphilic Block Copolymers in Solution. *Macromolecules* **2015**, *48*, 1152–1161. https://doi.org/10.1021/ma502163j.

(121) Yoreo, J. J. D.; Gilbert, P. U. P. A.; Sommerdijk, N. A. J. M.; Penn, R. L.; Whitelam, S.; Joester, D.; Zhang, H.; Rimer, J. D.; Navrotsky, A.; Banfield, J. F.; Wallace, A. F.; Michel, F. M.; Meldrum, F. C.; Cölfen, H.; Dove, P. M. Crystallization by Particle Attachment in Synthetic, Biogenic, and Geologic Environments. *Science* **2015**, *349*. https://doi.org/10.1126/science.aaa6760.

(122) Israelachvili, J. N.; Mitchell, D. J.; Ninham, B. W. Theory of Self-Assembly of Lipid Bilayers and Vesicles. *Biochim. Biophys. Acta BBA - Biomembr.* **1977**, *470*, 185–201. https://doi.org/10.1016/0005-2736(77)90099-2.

(123) Zhu, Y.; Yang, B.; Chen, S.; Du, J. Polymer Vesicles: Mechanism, Preparation, Application, and Responsive Behavior. *Prog. Polym. Sci.* **2017**, *64*, 1–22. https://doi.org/10.1016/j.progpolymsci.2015.05.001.

(124) Nikoubashman, A.; Schmid, F. The Molecular Lego Movie. *Nat. Chem.* **2019**, *11*, 298–300. https://doi.org/10.1038/s41557-019-0243-8.

(125) He, X.; Schmid, F. Spontaneous Formation of Complex Micelles from a Homogeneous Solution. *Phys. Rev. Lett.* **2008**, *100*, 137802. https://doi.org/10.1103/PhysRevLett.100.137802.

(126) He, X.; Schmid, F. Dynamics of Spontaneous Vesicle Formation in Dilute Solutions of Amphiphilic Diblock Copolymers. *Macromolecules* **2006**, *39*, 2654–2662. https://doi.org/10.1021/ma052536g.

(127) Zhu, G.; Sushko, M. L.; Loring, J. S.; Legg, B. A.; Song, M.; Soltis, J. A.; Huang, X.; Rosso, K. M.; De Yoreo, J. J. Self-Similar Mesocrystals Form via Interface-Driven Nucleation and Assembly. *Nature* **2021**, *590*, 416–422. https://doi.org/10.1038/s41586-021-03300-0.

(128) Omme, J. T. van; Wu, H.; Sun, H.; Beker, A. F.; Lemang, M.; Spruit, R. G.; Maddala, S. P.; Rakowski, A.; Friedrich, H.; Patterson, J. P.; Garza, H. H. P. Liquid Phase Transmission Electron Microscopy with Flow and Temperature Control. *J. Mater. Chem. C* **2020**, *8*, 10781–10790. https://doi.org/10.1039/D0TC01103G.

(129) Woehl, T. J.; Abellan, P. Defining the radiation chemistry during liquid cell electron microscopy to enable visualization of nanomaterial growth and degradation dynamics. *J. Microsc.* **2017**, *265*, 135–147. https://doi.org/10.1111/jmi.12508.
(130) Yao, L.; Ou, Z.; Luo, B.; Xu, C.; Chen, Q. Machine Learning to Reveal Nanoparticle Dynamics from Liquid-Phase TEM Videos. *ACS Cent. Sci.* **2020**. https://doi.org/10.1021/acscentsci.0c00430.
(131) Goodhew, P. J.; Humphreys, J. *Electron Microscopy and Analysis*; CRC Press, 2000.
(132) *X-Ray Crystallography by Gregory S. Girolami*; University Science Books, 2015.
(133) Asadabad, M. A.; Eskandari, M. J. Electron Diffraction. *Mod. Electron Microsc. Phys. Life Sci.* **2016**. https://doi.org/10.5772/61781.
(134) Anstis, G. R.; Liu, Z.; Lake, M. Investigation of Amorphous Materials by Electron Diffraction — The Effects of Multiple Scattering. *Ultramicroscopy* **1988**, *26*, 65–69. https://doi.org/10.1016/0304-3991(88)90378-6.
(135) Kolb, U.; Mugnaioli, E.; Gorelik, T. E. Automated Electron Diffraction Tomography – a New Tool for Nano Crystal Structure Analysis. *Cryst. Res. Technol.* **2011**, *46*, 542–554. https://doi.org/10.1002/crat.201100036.
(136) Gemmi, M.; Mugnaioli, E.; Gorelik, T. E.; Kolb, U.; Palatinus, L.; Boullay, P.; Hovmöller, S.; Abrahams, J. P. 3D Electron Diffraction: The Nanocrystallography Revolution. *ACS Cent. Sci.* **2019**, *5*, 1315–1329. https://doi.org/10.1021/acscentsci.9b00394.
(137) Wan, W.; Sun, J.; Su, J.; Hovmöller, S.; Zou, X. Three-Dimensional Rotation Electron Diffraction: Software RED for Automated Data Collection and Data Processing. *J. Appl. Crystallogr.* **2013**, *46*, 1863–1873. https://doi.org/10.1107/S0021889813027714.
(138) Nannenga, B. L.; Gonen, T. The Cryo-EM Method Microcrystal Electron Diffraction (MicroED). *Nat. Methods* **2019**, *16*, 369–379. https://doi.org/10.1038/s41592-019-0395-x.
(139) Shi, D.; Nannenga, B. L.; de la Cruz, M. J.; Liu, J.; Sawtelle, S.; Calero, G.; Reyes, F. E.; Hattne, J.; Gonen, T. The Collection of MicroED Data for Macromolecular Crystallography. *Nat. Protoc.* **2016**, *11*, 895–904. https://doi.org/10.1038/nprot.2016.046.
(140) Nannenga, B. L.; Shi, D.; Leslie, A. G. W.; Gonen, T. High-Resolution Structure Determination by Continuous-Rotation Data Collection in MicroED. *Nat. Methods* **2014**, *11*, 927–930. https://doi.org/10.1038/nmeth.3043.
(141) Jones, C. G.; Martynowycz, M. W.; Hattne, J.; Fulton, T. J.; Stoltz, B. M.; Rodriguez, J. A.; Nelson, H. M.; Gonen, T. The CryoEM Method MicroED as a Powerful Tool for Small Molecule Structure Determination. *ACS Cent. Sci.* **2018**, *4*, 1587–1592. https://doi.org/10.1021/acscentsci.8b00760.
(142) Shi, D.; Nannenga, B. L.; Iadanza, M. G.; Gonen, T. Three-Dimensional Electron Crystallography of Protein Microcrystals. *eLife* **2013**, *2*. https://doi.org/10.7554/eLife.01345.
(143) Yonekura, K.; Kato, K.; Ogasawara, M.; Tomita, M.; Toyoshima, C. Electron Crystallography of Ultrathin 3D Protein Crystals: Atomic Model with Charges. *Proc. Natl. Acad. Sci.* **2015**, *112*, 3368–3373. https://doi.org/10.1073/pnas.1500724112.
(144) Su, J.; Kapaca, E.; Liu, L.; Georgieva, V.; Wan, W.; Sun, J.; Valtchev, V.; Hovmöller, S.; Zou, X. Structure Analysis of Zeolites by Rotation Electron Diffraction (RED). *Microporous Mesoporous Mater.* **2014**, *189*, 115–125. https://doi.org/10.1016/j.micromeso.2013.10.014.
(145) Huang, Z.; Grape, E. S.; Li, J.; Inge, A. K.; Zou, X. 3D Electron Diffraction as an Important Technique for Structure Elucidation of Metal-Organic Frameworks and Covalent Organic Frameworks. *Coord. Chem. Rev.* **2021**, *427*, 213583. https://doi.org/10.1016/j.ccr.2020.213583.
(146) Sun, T.; Lei, W.; Ma, Y.; Zhang, Y.-B. Unravelling Crystal Structures of Covalent Organic Frameworks by Electron Diffraction Tomography. *Chin. J. Chem. n/a*. https://doi.org/10.1002/cjoc.202000120.

(147) Zhang, Y.-B.; Su, J.; Furukawa, H.; Yun, Y.; Gándara, F.; Duong, A.; Zou, X.; Yaghi, O. M. Single-Crystal Structure of a Covalent Organic Framework. *J. Am. Chem. Soc.* **2013**, *135*, 16336–16339. https://doi.org/10.1021/ja409033p.

(148) Gallagher-Jones, M.; Glynn, C.; Boyer, D. R.; Martynowycz, M. W.; Hernandez, E.; Miao, J.; Zee, C.-T.; Novikova, I. V.; Goldschmidt, L.; McFarlane, H. T.; Helguera, G. F.; Evans, J. E.; Sawaya, M. R.; Cascio, D.; Eisenberg, D. S.; Gonen, T.; Rodriguez, J. A. Sub-Ångström Cryo-EM Structure of a Prion Protofibril Reveals a Polar Clasp. *Nat. Struct. Mol. Biol.* **2018**, *25*, 131–134. https://doi.org/10.1038/s41594-017-0018-0.

(149) Wang, B.; Rhauderwiek, T.; Inge, A. K.; Xu, H.; Yang, T.; Huang, Z.; Stock, N.; Zou, X. A Porous Cobalt Tetraphosphonate Metal–Organic Framework: Accurate Structure and Guest Molecule Location Determined by Continuous-Rotation Electron Diffraction. *Chem. – Eur. J.* **2018**, *24*, 17429–17433. https://doi.org/10.1002/chem.201804133.

(150) Ercius, P.; Alaidi, O.; Rames, M. J.; Ren, G. Electron Tomography: A Three-Dimensional Analytic Tool for Hard and Soft Materials Research. *Adv. Mater.* **2015**, *27*, 5638–5663. https://doi.org/10.1002/adma.201501015.

(151) Ludwig, K.; Baljinnyam, B.; Herrmann, A.; Böttcher, C. The 3D Structure of the Fusion Primed Sendai F-Protein Determined by Electron Cryomicroscopy. *EMBO J.* **2003**, *22*, 3761–3771. https://doi.org/10.1093/emboj/cdg385.

(152) Kellermann, M.; Bauer, W.; Hirsch, A.; Schade, B.; Ludwig, K.; Böttcher, C. The First Account of a Structurally Persistent Micelle. *Angew. Chem. Int. Ed.* **2004**, *43*, 2959–2962. https://doi.org/10.1002/anie.200353510.

(153) Boettcher, C.; Stark, H.; van Heel, M. Stacked Bilayer Helices: A New Structural Organization of Amphiphilic Molecules. *Ultramicroscopy* **1996**, *62*, 133–139. https://doi.org/10.1016/0304-3991(95)00140-9.

(154) Boekema, E. J.; Folea, M.; Kouřil, R. Single Particle Electron Microscopy. *Photosynth. Res.* **2009**, *102*, 189. https://doi.org/10.1007/s11120-009-9443-1.

(155) Böttcher, C.; Schade, B.; Ecker, C.; Rabe, J. P.; Shu, L.; Schlüter, A. D. Double-Helical Ultrastructure of Polycationic Dendronized Polymers Determined by Single-Particle Cryo-TEM. *Chem. – Eur. J.* **2005**, *11*, 2923–2928. https://doi.org/10.1002/chem.200401145.

(156) Bai, X.; Martin, T. G.; Scheres, S. H. W.; Dietz, H. Cryo-EM Structure of a 3D DNA-Origami Object. *Proc. Natl. Acad. Sci.* **2012**, *109*, 20012–20017. https://doi.org/10.1073/pnas.1215713109.

(157) Tian, Y.; Lhermitte, J. R.; Bai, L.; Vo, T.; Xin, H. L.; Li, H.; Li, R.; Fukuto, M.; Yager, K. G.; Kahn, J. S.; Xiong, Y.; Minevich, B.; Kumar, S. K.; Gang, O. Ordered Three-Dimensional Nanomaterials Using DNA-Prescribed and Valence-Controlled Material Voxels. *Nat. Mater.* **2020**, *19*, 789–796. https://doi.org/10.1038/s41563-019-0550-x.

(158) Ong, L. L.; Hanikel, N.; Yaghi, O. K.; Grun, C.; Strauss, M. T.; Bron, P.; Lai-Kee-Him, J.; Schueder, F.; Wang, B.; Wang, P.; Kishi, J. Y.; Myhrvold, C.; Zhu, A.; Jungmann, R.; Bellot, G.; Ke, Y.; Yin, P. Programmable Self-Assembly of Three-Dimensional Nanostructures from 10,000 Unique Components. *Nature* **2017**, *552*, 72–77. https://doi.org/10.1038/nature24648.

(159) He, Y.; Ye, T.; Su, M.; Zhang, C.; Ribbe, A. E.; Jiang, W.; Mao, C. Hierarchical Self-Assembly of DNA into Symmetric Supramolecular Polyhedra. *Nature* **2008**, *452*, 198–201. https://doi.org/10.1038/nature06597.

(160) Zhang, C.; Su, M.; He, Y.; Zhao, X.; Fang, P. -a.; Ribbe, A. E.; Jiang, W.; Mao, C. Conformational Flexibility Facilitates Self-Assembly of Complex DNA Nanostructures. *Proc. Natl. Acad. Sci.* **2008**, *105*, 10665–10669. https://doi.org/10.1073/pnas.0803841105.

(161) Kochovski, Z.; Chen, G.; Yuan, J.; Lu, Y. Cryo-Electron Microscopy for the Study of Self-Assembled Poly(Ionic Liquid) Nanoparticles and Protein Supramolecular Structures. *Colloid Polym. Sci.* **2020**, *298*, 707–717. https://doi.org/10.1007/s00396-020-04657-w.

(162) Koster, A. J.; Grimm, R.; Typke, D.; Hegerl, R.; Stoschek, A.; Walz, J.; Baumeister, W. Perspectives of Molecular and Cellular Electron Tomography. *J. Struct. Biol.* **1997**, *120*, 276–308. https://doi.org/10.1006/jsbi.1997.3933.
(163) Jinnai, H.; Jiang, X. Electron Tomography in Soft Materials. *Curr. Opin. Solid State Mater. Sci.* **2013**, *17*, 135–142. https://doi.org/10.1016/j.cossms.2013.07.001.
(164) Evans, J. E.; Friedrich, H. Advanced Tomography Techniques for Inorganic, Organic, and Biological Materials. 6.
(165) Midgley, P. A.; Weyland, M. 3D Electron Microscopy in the Physical Sciences: The Development of Z-Contrast and EFTEM Tomography. *Ultramicroscopy* **2003**, *96*, 413–431. https://doi.org/10.1016/S0304-3991(03)00105-0.
(166) Midgley, P. A.; Ward, E. P. W.; Hungría, A. B.; Thomas, J. M. Nanotomography in the Chemical, Biological and Materials Sciences. *Chem. Soc. Rev.* **2007**, *36*, 1477–1494. https://doi.org/10.1039/B701569K.
(167) Vanhecke, D.; Asano, S.; Kochovski, Z.; Fernandez-Busnadiego, R.; Schrod, N.; Baumeister, W.; Lučić, V. Cryo-Electron Tomography: Methodology, Developments and Biological Applications. *J. Microsc.* **2011**, *242*, 221–227. https://doi.org/10.1111/j.1365-2818.2010.03478.x.
(168) Mastronarde, D. N. Dual-Axis Tomography: An Approach with Alignment Methods That Preserve Resolution. *J. Struct. Biol.* **1997**, *120*, 343–352. https://doi.org/10.1006/jsbi.1997.3919.
(169) Kawase, N.; Kato, M.; Nishioka, H.; Jinnai, H. Transmission Electron Microtomography without the "Missing Wedge" for Quantitative Structural Analysis. *Ultramicroscopy* **2007**, *107*, 8–15. https://doi.org/10.1016/j.ultramic.2006.04.007.
(170) Precise and Reversible Protein-Microtubule-Like Structure with Helicity Driven by Dual Supramolecular Interactions | Journal of the American Chemical Society https://pubs.acs.org/doi/pdf/10.1021/jacs.5b11733 (accessed 2020 -11 -23).
(171) Merg, A. D.; Boatz, J. C.; Mandal, A.; Zhao, G.; Mokashi-Punekar, S.; Liu, C.; Wang, X.; Zhang, P.; Wel, P. C. A. van der; Rosi, N. L. Peptide-Directed Assembly of Single-Helical Gold Nanoparticle Superstructures Exhibiting Intense Chiroptical Activity https://pubs.acs.org/doi/pdf/10.1021/jacs.6b07322 (accessed 2020 -11 -23). https://doi.org/10.1021/jacs.6b07322.
(172) Holder, S. J.; Sommerdijk, N. A. J. M. New Micellar Morphologies from Amphiphilic Block Copolymers: Disks, Toroids and Bicontinuous Micelles. *Polym. Chem.* **2011**, *2*, 1018–1028. https://doi.org/10.1039/C0PY00379D.
(173) Yamauchi, K.; Takahashi, K.; Hasegawa, H.; Iatrou, H.; Hadjichristidis, N.; Kaneko, T.; Nishikawa, Y.; Jinnai, H.; Matsui, T.; Nishioka, H.; Shimizu, M.; Furukawa, H. Microdomain Morphology in an ABC 3-Miktoarm Star Terpolymer: A Study by Energy-Filtering TEM and 3D Electron Tomography. *Macromolecules* **2003**, *36*, 6962–6966. https://doi.org/10.1021/ma034840k.
(174) Berlepsch, H. v; Böttcher, C.; Skrabania, K.; Laschewsky, A. Complex Domain Architecture of Multicompartment Micelles from a Linear ABC Triblock Copolymer Revealed by Cryogenic Electron Tomography. *Chem. Commun.* **2009**, No. 17, 2290–2292. https://doi.org/10.1039/B903658J.
(175) Hermans, T. M.; Broeren, M. A. C.; Gomopoulos, N.; van der Schoot, P.; van Genderen, M. H. P.; Sommerdijk, N. A. J. M.; Fytas, G.; Meijer, E. W. Self-Assembly of Soft Nanoparticles with Tunable Patchiness. *Nat. Nanotechnol.* **2009**, *4*, 721–726. https://doi.org/10.1038/nnano.2009.232.
(176) Young, W.-S.; Kuan, W.-F.; Epps, T. H. Block Copolymer Electrolytes for Rechargeable Lithium Batteries. *J. Polym. Sci. Part B Polym. Phys.* **2014**, *52*, 1–16. https://doi.org/10.1002/polb.23404.
(177) Andersson, B. V.; Herland, A.; Masich, S.; Inganäs, O. Imaging of the 3D Nanostructure of a Polymer Solar Cell by Electron Tomography https://pubs.acs.org/doi/pdf/10.1021/nl803676e (accessed 2020 -11 -23). https://doi.org/10.1021/nl803676e.

(178) Hindson, J. C.; Saghi, Z.; Hernandez-Garrido, J.-C.; Midgley, P. A.; Greenham, N. C. Morphological Study of Nanoparticle−Polymer Solar Cells Using High-Angle Annular Dark-Field Electron Tomography. *Nano Lett.* **2011**, *11*, 904–909. https://doi.org/10.1021/nl104436j.
(179) Oosterhout, S. D.; Wienk, M. M.; van Bavel, S. S.; Thiedmann, R.; Jan Anton Koster, L.; Gilot, J.; Loos, J.; Schmidt, V.; Janssen, R. A. J. The Effect of Three-Dimensional Morphology on the Efficiency of Hybrid Polymer Solar Cells. *Nat. Mater.* **2009**, *8*, 818–824. https://doi.org/10.1038/nmat2533.
(180) Sai, H.; Tan, K. W.; Hur, K.; Asenath-Smith, E.; Hovden, R.; Jiang, Y.; Riccio, M.; Muller, D. A.; Elser, V.; Estroff, L. A.; Gruner, S. M.; Wiesner, U. Hierarchical Porous Polymer Scaffolds from Block Copolymers. *Science* **2013**, *341*, 530–534. https://doi.org/10.1126/science.1238159.
(181) Jinnai, H.; Spontak, R. J.; Nishi, T. Transmission Electron Microtomography and Polymer Nanostructures. *Macromolecules* **2010**, *43*, 1675–1688. https://doi.org/10.1021/ma902035p.
(182) Park, H.-W.; Jung, J.; Chang, T.; Matsunaga, K.; Jinnai, H. New Epitaxial Phase Transition between DG and HEX in PS-b-PI. *J. Am. Chem. Soc.* **2009**, *131*, 46–47. https://doi.org/10.1021/ja808259m.
(183) Wirix, M. J. M.; Bomans, P. H. H.; Hendrix, M. M. R. M.; Friedrich, H.; Sommerdijk, N. A. J. M.; With, G. de. Visualizing Order in Dispersions and Solid State Morphology with Cryo-TEM and Electron Tomography: P3HT : PCBM Organic Solar Cells. *J. Mater. Chem. A* **2015**, *3*, 5031–5040. https://doi.org/10.1039/C4TA05161K.
(184) McKenzie, B. E.; Friedrich, H.; Wirix, M. J. M.; de Visser, J. F.; Monaghan, O. R.; Bomans, P. H. H.; Nudelman, F.; Holder, S. J.; Sommerdijk, N. A. J. M. Controlling Internal Pore Sizes in Bicontinuous Polymeric Nanospheres. *Angew. Chem.* **2015**, *127*, 2487–2491. https://doi.org/10.1002/ange.201408811.
(185) McKenzie, B. E.; Visser, J. F. de; Friedrich, H.; Wirix, M. J. M.; Bomans, P. H. H.; With, G. de; Holder, S. J.; Sommerdijk, N. A. J. M. Bicontinuous Nanospheres from Simple Amorphous Amphiphilic Diblock Copolymers https://pubs.acs.org/doi/pdf/10.1021/ma4019729 (accessed 2020 -11 -23). https://doi.org/10.1021/ma4019729.
(186) McKenzie, B. E.; Nudelman, F.; Bomans, P. H. H.; Holder, S. J.; Sommerdijk, N. A. J. M. Temperature-Responsive Nanospheres with Bicontinuous Internal Structures from a Semicrystalline Amphiphilic Block Copolymer. *J. Am. Chem. Soc.* **2010**, *132*, 10256–10259. https://doi.org/10.1021/ja102040u.
(187) Parry, A. L.; Bomans, P. H. H.; Holder, S. J.; Sommerdijk, N. A. J. M.; Biagini, S. C. G. Cryo Electron Tomography Reveals Confined Complex Morphologies of Tripeptide-Containing Amphiphilic Double-Comb Diblock Copolymers. *Angew. Chem.* **2008**, *120*, 8991–8994. https://doi.org/10.1002/ange.200802834.
(188) Sharma, J.; Chhabra, R.; Cheng, A.; Brownell, J.; Liu, Y.; Yan, H. Control of Self-Assembly of DNA Tubules Through Integration of Gold Nanoparticles. *Science* **2009**, *323*, 112–116. https://doi.org/10.1126/science.1165831.
(189) Wong, C. K.; Heidelmann, M.; Dulle, M.; Qiang, X.; Förster, S.; Stenzel, M. H.; Gröschel, A. H. Vesicular Polymer Hexosomes Exhibit Topological Defects. *J. Am. Chem. Soc.* **2020**, *142*, 10989–10995. https://doi.org/10.1021/jacs.0c02009.
(190) Park, J.; Elmlund, H.; Ercius, P.; Yuk, J. M.; Limmer, D. T.; Chen, Q.; Kim, K.; Han, S. H.; Weitz, D. A.; Zettl, A.; Alivisatos, A. P. 3D Structure of Individual Nanocrystals in Solution by Electron Microscopy. *Science* **2015**, *349*, 290–295. https://doi.org/10.1126/science.aab1343.
(191) Kim, B. H.; Heo, J.; Kim, S.; Reboul, C. F.; Chun, H.; Kang, D.; Bae, H.; Hyun, H.; Lim, J.; Lee, H.; Han, B.; Hyeon, T.; Alivisatos, A. P.; Ercius, P.; Elmlund, H.; Park, J. Critical Differences in 3D Atomic Structure of Individual Ligand-Protected Nanocrystals in Solution. *Science* **2020**, *368*, 60–67. https://doi.org/10.1126/science.aax3233.

(192) Park, J.; Elmlund, H.; Ercius, P.; Yuk, J. M.; Limmer, D. T.; Chen, Q.; Kim, K.; Han, S. H.; Weitz, D. A.; Zettl, A.; Alivisatos, A. P. 3D Structure of Individual Nanocrystals in Solution by Electron Microscopy. *Science* **2015**, *349*, 290–295. https://doi.org/10.1126/science.aab1343.
(193) Kim, B. H.; Heo, J.; Park, J. Determination of the 3D Atomic Structures of Nanoparticles. *Small Sci.* **2021**, *1*, 2000045. https://doi.org/10.1002/smsc.202000045.
(194) Pal, R.; Sikder, A. K.; Saito, K.; Funston, A. M.; Bellare, J. R. Electron Energy Loss Spectroscopy for Polymers: A Review. *Polym. Chem.* **2017**, *8*, 6927–6937. https://doi.org/10.1039/C7PY01459G.
(195) Allen, L. J.; D'Alfonso, A. J.; Freitag, B.; Klenov, D. O. Chemical Mapping at Atomic Resolution Using Energy-Dispersive x-Ray Spectroscopy. *MRS Bull.* **2012**, *37*, 47–52. https://doi.org/10.1557/mrs.2011.331.
(196) Ebnesajjad, S. Chapter 4 - Surface and Material Characterization Techniques. In *Surface Treatment of Materials for Adhesive Bonding (Second Edition)*; Ebnesajjad, S., Ed.; William Andrew Publishing: Oxford, 2014; pp 39–75. https://doi.org/10.1016/B978-0-323-26435-8.00004-6.
(197) Krivanek, O. L.; Lovejoy, T. C.; Dellby, N.; Aoki, T.; Carpenter, R. W.; Rez, P.; Soignard, E.; Zhu, J.; Batson, P. E.; Lagos, M. J.; Egerton, R. F.; Crozier, P. A. Vibrational Spectroscopy in the Electron Microscope. *Nature* **2014**, *514*, 209–212. https://doi.org/10.1038/nature13870.
(198) Arora, H.; Du, P.; Tan, K. W.; Hyun, J. K.; Grazul, J.; Xin, H. L.; Muller, D. A.; Thompson, M. O.; Wiesner, U. Block Copolymer Self-Assembly–Directed Single-Crystal Homo- and Heteroepitaxial Nanostructures. *Science* **2010**, *330*, 214–219. https://doi.org/10.1126/science.1193369.
(199) Yuan, Z.; Zhang, L.; Li, S.; Zhang, W.; Lu, M.; Pan, Y.; Xie, X.; Huang, L.; Huang, W. Paving Metal–Organic Frameworks with Upconversion Nanoparticles via Self-Assembly. *J. Am. Chem. Soc.* **2018**, *140*, 15507–15515. https://doi.org/10.1021/jacs.8b10122.
(200) He, H.; Rahimi, K.; Zhong, M.; Mourran, A.; Luebke, D. R.; Nulwala, H. B.; Möller, M.; Matyjaszewski, K. Cubosomes from Hierarchical Self-Assembly of Poly(Ionic Liquid) Block Copolymers. *Nat. Commun.* **2017**, *8*, 14057. https://doi.org/10.1038/ncomms14057.
(201) Howe, D. H.; Hart, J. L.; McDaniel, R. M.; Taheri, M. L.; Magenau, A. J. D. Functionalization-Induced Self-Assembly of Block Copolymers for Nanoparticle Synthesis. *ACS Macro Lett.* **2018**, *7*, 1503–1508. https://doi.org/10.1021/acsmacrolett.8b00815.
(202) Hickey, R. J.; Haynes, A. S.; Kikkawa, J. M.; Park, S.-J. Controlling the Self-Assembly Structure of Magnetic Nanoparticles and Amphiphilic Block-Copolymers: From Micelles to Vesicles. *J. Am. Chem. Soc.* **2011**, *133*, 1517–1525. https://doi.org/10.1021/ja1090113.
(203) Denny, M. S.; Parent, L. R.; Patterson, J. P.; Meena, S. K.; Pham, H.; Abellan, P.; Ramasse, Q. M.; Paesani, F.; Gianneschi, N. C.; Cohen, S. M. Transmission Electron Microscopy Reveals Deposition of Metal Oxide Coatings onto Metal–Organic Frameworks. *J. Am. Chem. Soc.* **2018**, *140*, 1348–1357. https://doi.org/10.1021/jacs.7b10453.
(204) Sainsbury, T.; Ikuno, T.; Okawa, D.; Pacilé, D.; Fréchet, J. M. J.; Zettl, A. Self-Assembly of Gold Nanoparticles at the Surface of Amine- and Thiol-Functionalized Boron Nitride Nanotubes. *J. Phys. Chem. C* **2007**, *111*, 12992–12999. https://doi.org/10.1021/jp072958n.
(205) Leyva-Porras, C.; Ornelas-Gutiérrez, C.; Miki-Yoshida, M.; Avila-Vega, Y. I.; Macossay, J.; Bonilla-Cruz, J. EELS Analysis of Nylon 6 Nanofibers Reinforced with Nitroxide-Functionalized Graphene Oxide. *Carbon* **2014**, *70*, 164–172. https://doi.org/10.1016/j.carbon.2013.12.087.
(206) Wang, D.-W.; Li, F.; Zhao, J.; Ren, W.; Chen, Z.-G.; Tan, J.; Wu, Z.-S.; Gentle, I.; Lu, G. Q.; Cheng, H.-M. Fabrication of Graphene/Polyaniline Composite Paper via In Situ Anodic Electropolymerization for High-Performance Flexible Electrode. *ACS Nano* **2009**, *3*, 1745–1752. https://doi.org/10.1021/nn900297m.
(207) Esken, D.; Turner, S.; Wiktor, C.; Kalidindi, S. B.; Van Tendeloo, G.; Fischer, R. A. GaN@ZIF-8: Selective Formation of Gallium Nitride Quantum Dots inside a Zinc Methylimidazolate Framework. *J. Am. Chem. Soc.* **2011**, *133*, 16370–16373. https://doi.org/10.1021/ja207077u.

(208) Rez, P.; Aoki, T.; March, K.; Gur, D.; Krivanek, O. L.; Dellby, N.; Lovejoy, T. C.; Wolf, S. G.; Cohen, H. Damage-Free Vibrational Spectroscopy of Biological Materials in the Electron Microscope. *Nat. Commun.* **2016**, *7*, 10945. https://doi.org/10.1038/ncomms10945.

(209) Ophus, C. Four-Dimensional Scanning Transmission Electron Microscopy (4D-STEM): From Scanning Nanodiffraction to Ptychography and Beyond. *Microsc. Microanal.* **2019**, *25*, 563–582. https://doi.org/10.1017/S1431927619000497.

(210) Ophus, C.; Ercius, P.; Sarahan, M.; Czarnik, C.; Ciston, J. Recording and Using 4D-STEM Datasets in Materials Science. *Microsc. Microanal.* **2014**, *20*, 62–63. https://doi.org/10.1017/S1431927614002037.

(211) Gallagher-Jones, M.; Ophus, C.; Bustillo, K. C.; Boyer, D. R.; Panova, O.; Glynn, C.; Zee, C.-T.; Ciston, J.; Mancia, K. C.; Minor, A. M.; Rodriguez, J. A. Nanoscale Mosaicity Revealed in Peptide Microcrystals by Scanning Electron Nanodiffraction. *Commun. Biol.* **2019**, *2*, 26. https://doi.org/10.1038/s42003-018-0263-8.

(212) Ortiz, G. C.; Zhu, M.; Dou, L.; Hwang, J. 4D-STEM Quantification of Nanoscale Ordered Domains in Organic Semiconducting Polymers. *Microsc. Microanal.* **2020**, *26*, 1740–1742. https://doi.org/10.1017/S1431927620019170.

(213) Londoño-Calderon, A.; Williams, D. J.; Schneider, M.; Savitzky, B. H.; Ophus, C.; Pettes, M. T. Local Lattice Deformation of Tellurene Grain Boundaries by Four-Dimensional Electron Microscopy. *J. Phys. Chem. C* **2021**, *125*, 3396–3405. https://doi.org/10.1021/acs.jpcc.1c00308.

(214) Johnstone, D. N.; Firth, F. C. N.; Grey, C. P.; Midgley, P. A.; Cliffe, M. J.; Collins, S. M. Direct Imaging of Correlated Defect Nanodomains in a Metal–Organic Framework. *J. Am. Chem. Soc.* **2020**, *142*, 13081–13089. https://doi.org/10.1021/jacs.0c04468.

(215) Mu, X.; Mazilkin, A.; Sprau, C.; Colsmann, A.; Kübel, C. Mapping Structure and Morphology of Amorphous Organic Thin Films by 4D-STEM Pair Distribution Function Analysis. *Microscopy* **2019**, *68*, 301–309. https://doi.org/10.1093/jmicro/dfz015.

(216) Bustillo, K. C.; Panova, O.; Chen, X. C.; Takacs, C. J.; Ciston, J.; Ophus, C.; Balsara, N. P.; Minor, A. M. Nanobeam Scanning Diffraction for Orientation Mapping of Polymers. *Microsc. Microanal.* **2017**, *23*, 1782–1783. https://doi.org/10.1017/S1431927617009576.

(217) Panova, O.; Chen, X. C.; Bustillo, K. C.; Ophus, C.; Bhatt, M. P.; Balsara, N.; Minor, A. M. Orientation Mapping of Semicrystalline Polymers Using Scanning Electron Nanobeam Diffraction. *Micron* **2016**, *88*, 30–36. https://doi.org/10.1016/j.micron.2016.05.008.

(218) Kanomi, S.; Marubayashi, H.; Miyata, T.; Tsuda, K.; Jinnai, H. Nanodiffraction Imaging of Polymer Crystals. *Macromolecules* **2021**, *54*, 6028–6037. https://doi.org/10.1021/acs.macromol.1c00683.

(219) Gallagher-Jones, M.; Bustillo, K. C.; Ophus, C.; Richards, L. S.; Ciston, J.; Lee, S.; Minor, A. M.; Rodriguez, J. A. Atomic Structures Determined from Digitally Defined Nanocrystalline Regions. *IUCrJ* **2020**, *7*, 490–499. https://doi.org/10.1107/S2052252520004030.

(220) Hou, J.; Ashling, C. W.; Collins, S. M.; Krajnc, A.; Zhou, C.; Longley, L.; Johnstone, D. N.; Chater, P. A.; Li, S.; Coulet, M.-V.; Llewellyn, P. L.; Coudert, F.-X.; Keen, D. A.; Midgley, P. A.; Mali, G.; Chen, V.; Bennett, T. D. Metal-Organic Framework Crystal-Glass Composites. *Nat. Commun.* **2019**, *10*, 2580. https://doi.org/10.1038/s41467-019-10470-z.

(221) Bustillo, K. C.; Zeltmann, S. E.; Chen, M.; Donohue, J.; Ciston, J.; Ophus, C.; Minor, A. M. 4D-STEM of Beam-Sensitive Materials. *Acc. Chem. Res.* **2021**, acs.accounts.1c00073. https://doi.org/10.1021/acs.accounts.1c00073.

(222) Zhou, L.; Song, J.; Kim, J. S.; Pei, X.; Huang, C.; Boyce, M.; Mendonça, L.; Clare, D.; Siebert, A.; Allen, C. S.; Liberti, E.; Stuart, D.; Pan, X.; Nellist, P. D.; Zhang, P.; Kirkland, A. I.; Wang, P. Low-Dose Phase Retrieval of Biological Specimens Using Cryo-Electron Ptychography. *Nat. Commun.* **2020**, *11*, 2773. https://doi.org/10.1038/s41467-020-16391-6.

(223) Bustillo, K.; Zeltmann, S.; Chen, M.; Donohue, J.; Mueller, A.; Ophus, C.; Ciston, J.; Minor, A. 4DSTEM of Beam-Sensitive Materials: Optimizing SNR and Improving Spatial Resolution. *Microsc. Microanal.* **2020**, *26*, 1734–1735. https://doi.org/10.1017/S1431927620019157.

(224) Panova, O.; Ophus, C.; Takacs, C. J.; Bustillo, K. C.; Balhorn, L.; Salleo, A.; Balsara, N.; Minor, A. M. Diffraction Imaging of Nanocrystalline Structures in Organic Semiconductor Molecular Thin Films. *Nat. Mater.* **2019**, *18*, 860–865. https://doi.org/10.1038/s41563-019-0387-3.

(225) Song, J.; Allen, C. S.; Gao, S.; Huang, C.; Sawada, H.; Pan, X.; Warner, J.; Wang, P.; Kirkland, A. I. Atomic Resolution Defocused Electron Ptychography at Low Dose with a Fast, Direct Electron Detector. *Sci. Rep.* **2019**, *9*, 3919. https://doi.org/10.1038/s41598-019-40413-z.

(226) Ciston, J.; Johnson, I. J.; Draney, B. R.; Ercius, P.; Fong, E.; Goldschmidt, A.; Joseph, J. M.; Lee, J. R.; Mueller, A.; Ophus, C.; Selvarajan, A.; Skinner, D. E.; Stezelberger, T.; Tindall, C. S.; Minor, A. M.; Denes, P. The 4D Camera: Very High Speed Electron Counting for 4D-STEM. *Microsc. Microanal.* **2019**, *25*, 1930–1931. https://doi.org/10.1017/S1431927619010389.

(227) Savitzky, B. H.; Hughes, L. A.; Zeltmann, S. E.; Brown, H. G.; Zhao, S.; Pelz, P. M.; Barnard, E. S.; Donohue, J.; DaCosta, L. R.; Pekin, T. C.; Kennedy, E.; Janish, M. T.; Schneider, M. M.; Herring, P.; Gopal, C.; Anapolsky, A.; Ercius, P.; Scott, M.; Ciston, J.; Minor, A. M.; Ophus, C. Py4DSTEM: A Software Package for Multimodal Analysis of Four-Dimensional Scanning Transmission Electron Microscopy Datasets. *ArXiv200309523 Cond-Mat Physicsphysics* **2020**.

(228) Ercius, P.; Johnson, I.; Brown, H.; Pelz, P.; Hsu, S.-L.; Draney, B.; Fong, E.; Goldschmidt, A.; Joseph, J.; Lee, J.; Ciston, J.; Ophus, C.; Scott, M.; Selvarajan, A.; Paul, D.; Skinner, D.; Hanwell, M.; Harris, C.; Avery, P.; Stezelberger, T.; Tindall, C.; Ramesh, R.; Minor, A.; Denes, P. The 4D Camera – An 87 KHz Frame-Rate Detector for Counted 4D-STEM Experiments. *Microsc. Microanal.* **2020**, *26*, 1896–1897. https://doi.org/10.1017/S1431927620019753.

(229) Roe, R.-J.; Roe, P. of M. S. R.-J. *Methods of X-Ray and Neutron Scattering in Polymer Science*; Oxford University Press, 2000.

(230) Fundamental Concepts. In *Light Scattering from Polymer Solutions and Nanoparticle Dispersions*; Schärtl, W., Ed.; Springer Laboratory; Springer: Berlin, Heidelberg, 2007; pp 1–24. https://doi.org/10.1007/978-3-540-71951-9_1.

(231) Patterson, J. P.; Robin, M. P.; Chassenieux, C.; Colombani, O.; O'Reilly, R. K. The Analysis of Solution Self-Assembled Polymeric Nanomaterials. *Chem. Soc. Rev.* **2014**, *43*, 2412–2425. https://doi.org/10.1039/C3CS60454C.

(232) Simone, P. M.; Lodge, T. P. Micellization of PS-PMMA Diblock Copolymers in an Ionic Liquid. *Macromol. Chem. Phys.* **2007**, *208*, 339–348. https://doi.org/10.1002/macp.200600392.

(233) Walther, A.; Drechsler, M.; Rosenfeldt, S.; Harnau, L.; Ballauff, M.; Abetz, V.; Müller, A. H. E. Self-Assembly of Janus Cylinders into Hierarchical Superstructures. *J. Am. Chem. Soc.* **2009**, *131*, 4720–4728. https://doi.org/10.1021/ja808614q.

(234) Colombani, O.; Markus Ruppel; Burkhardt, M.; Drechsler, M.; Schumacher, M.; Gradzielski, M.; Schweins, R.; Müller, A. H. E. Structure of Micelles of Poly(*n* -Butyl Acrylate)- *Block* -Poly(Acrylic Acid) Diblock Copolymers in Aqueous Solution. *Macromolecules* **2007**, *40*, 4351–4362. https://doi.org/10.1021/ma0609580.

(235) Massey, J.; Power, K. N.; Manners, I.; Winnik, M. A. Self-Assembly of a Novel Organometallic−Inorganic Block Copolymer in Solution and the Solid State: Nonintrusive Observation of Novel Wormlike Poly(Ferrocenyldimethylsilane)-b-Poly(Dimethylsiloxane) Micelles. *J. Am. Chem. Soc.* **1998**, *120*, 9533–9540. https://doi.org/10.1021/ja981803d.

(236) Ruzette, A.-V.; Tencé-Girault, S.; Leibler, L.; Chauvin, F.; Bertin, D.; Guerret, O.; Gérard, P. Molecular Disorder and Mesoscopic Order in Polydisperse Acrylic Block Copolymers Prepared by Controlled Radical Polymerization. *Macromolecules* **2006**, *39*, 5804–5814. https://doi.org/10.1021/ma060541u.

(237) Derry, M. J.; Fielding, L. A.; Warren, N. J.; Mable, C. J.; Smith, A. J.; Mykhaylyk, O. O.; Armes, S. P. In Situ Small-Angle X-Ray Scattering Studies of Sterically-Stabilized Diblock Copolymer Nanoparticles Formed during Polymerization-Induced Self-Assembly in Non-Polar Media. *Chem. Sci.* **2016**, *7*, 5078–5090. https://doi.org/10.1039/C6SC01243D.

(238) Kelley, E. G.; Murphy, R. P.; Seppala, J. E.; Smart, T. P.; Hann, S. D.; Sullivan, M. O.; Epps, T. H. Size Evolution of Highly Amphiphilic Macromolecular Solution Assemblies via a Distinct Bimodal Pathway. *Nat. Commun.* **2014**, *5*, 3599. https://doi.org/10.1038/ncomms4599.

(239) Bang, J.; Jain, S.; Li, Z.; Lodge, T. P.; Pedersen, J. S.; Kesselman, E.; Talmon, Y. Sphere, Cylinder, and Vesicle Nanoaggregates in Poly(Styrene-b-Isoprene) Diblock Copolymer Solutions. *Macromolecules* **2006**, *39*, 1199–1208. https://doi.org/10.1021/ma052023+.

(240) Xu, H.; Das, A. K.; Horie, M.; Shaik, M. S.; Smith, A. M.; Luo, Y.; Lu, X.; Collins, R.; Liem, S. Y.; Song, A.; Popelier, P. L. A.; Turner, M. L.; Xiao, P.; Kinloch, I. A.; Ulijn, R. V. An Investigation of the Conductivity of Peptide Nanotube Networks Prepared by Enzyme-Triggered Self-Assembly. *Nanoscale* **2010**, *2*, 960. https://doi.org/10.1039/b9nr00233b.

(241) Tang, C.; Smith, A. M.; Collins, R. F.; Ulijn, R. V.; Saiani, A. Fmoc-Diphenylalanine Self-Assembly Mechanism Induces Apparent PKa Shifts. *Langmuir* **2009**, *25*, 9447–9453. https://doi.org/10.1021/la900653q.

(242) Hollamby, M. J. Practical Applications of Small-Angle Neutron Scattering. *Phys. Chem. Chem. Phys.* **2013**, *15*, 10566–10579. https://doi.org/10.1039/C3CP50293G.

(243) Pochan, D. J.; Pakstis, L.; Ozbas, B.; Nowak, A. P.; Deming, T. J. SANS and Cryo-TEM Study of Self-Assembled Diblock Copolypeptide Hydrogels with Rich Nano- through Microscale Morphology. *Macromolecules* **2002**, *35*, 5358–5360. https://doi.org/10.1021/ma025526d.

(244) Förster, S.; Hermsdorf, N.; Böttcher, C.; Lindner, P. Structure of Polyelectrolyte Block Copolymer Micelles. *Macromolecules* **2002**, *35*, 4096–4105. https://doi.org/10.1021/ma011565y.

(245) Fauquignon, M.; Ibarboure, E.; Carlotti, S.; Brûlet, A.; Schmutz, M.; Le Meins, J.-F. Large and Giant Unilamellar Vesicle(s) Obtained by Self-Assembly of Poly(Dimethylsiloxane)-b-Poly(Ethylene Oxide) Diblock Copolymers, Membrane Properties and Preliminary Investigation of Their Ability to Form Hybrid Polymer/Lipid Vesicles. *Polymers* **2019**, *11*, 2013. https://doi.org/10.3390/polym11122013.

(246) Davidson, M. W.; Abramowitz, M. Optical Microscopy. In *Encyclopedia of Imaging Science and Technology*; American Cancer Society, 2002. https://doi.org/10.1002/0471443395.img074.

(247) Bayguinov, P. O.; Oakley, D. M.; Shih, C.-C.; Geanon, D. J.; Joens, M. S.; Fitzpatrick, J. A. J. Modern Laser Scanning Confocal Microscopy: Bayguinov et Al. *Curr. Protoc. Cytom.* **2018**, *85*, e39. https://doi.org/10.1002/cpcy.39.

(248) Du, Y.; Pan, J.; Choi, J. H. A Review on Optical Imaging of DNA Nanostructures and Dynamic Processes. *Methods Appl. Fluoresc.* **2019**, *7*, 012002. https://doi.org/10.1088/2050-6120/aaed11.

(249) Sanderson, M. J.; Smith, I.; Parker, I.; Bootman, M. D. Fluorescence Microscopy. *Cold Spring Harb. Protoc.* **2014**, *2014*, pdb.top071795-pdb.top071795. https://doi.org/10.1101/pdb.top071795.

(250) Oldenbourg, R. Polarized Light Microscopy: Principles and Practice. *Cold Spring Harb. Protoc.* **2013**, *2013*, pdb.top078600-pdb.top078600. https://doi.org/10.1101/pdb.top078600.

(251) Kino, G. S.; Corle, T. R. *Confocal Scanning Optical Microscopy and Related Imaging Systems*; Academic Press, 1996.

(252) Voelker-Pop, L. M. Optical Methods in Rheology: Polarized Light Imaging. *Chem. Listy* **2014**, *108*, 707–710.

(253) Pujals, S.; Feiner-Gracia, N.; Delcanale, P.; Voets, I.; Albertazzi, L. Super-Resolution Microscopy as a Powerful Tool to Study Complex Synthetic Materials. *Nat. Rev. Chem.* **2019**, *3*, 68–84. https://doi.org/10.1038/s41570-018-0070-2.

(254) He, C.; Lu, K.; Liu, D.; Lin, W. Nanoscale Metal−Organic Frameworks for the Co-Delivery of Cisplatin and Pooled SiRNAs to Enhance Therapeutic Efficacy in Drug-Resistant Ovarian Cancer Cells. *J Am Chem Soc* **2014**, 4.

(255) Zhang, H.; Li, Q.; Liu, R.; Zhang, X.; Li, Z.; Luan, Y. A Versatile Prodrug Strategy to In Situ Encapsulate Drugs in MOF Nanocarriers: A Case of Cytarabine-IR820 Prodrug Encapsulated ZIF-8 toward Chemo-Photothermal Therapy. *Adv. Funct. Mater.* **2018**, *28*, 1802830. https://doi.org/10.1002/adfm.201802830.

(256) Borchert, U.; Lipprandt, U.; Bilang, M.; Kimpfler, A.; Rank, A.; Peschka-Süss, R.; Schubert, R.; Lindner, P.; Förster, S. PH-Induced Release from P2VP−PEO Block Copolymer Vesicles. *Langmuir* **2006**, *22*, 5843–5847. https://doi.org/10.1021/la060227t.

(257) Gudlur, S.; Sukthankar, P.; Gao, J.; Avila, L. A.; Hiromasa, Y.; Chen, J.; Iwamoto, T.; Tomich, J. M. Peptide Nanovesicles Formed by the Self-Assembly of Branched Amphiphilic Peptides. *PLoS ONE* **2012**, *7*, e45374. https://doi.org/10.1371/journal.pone.0045374.

(258) Yallapu, M. M.; Jaggi, M.; Chauhan, S. C. β-Cyclodextrin-Curcumin Self-Assembly Enhances Curcumin Delivery in Prostate Cancer Cells. *Colloids Surf. B Biointerfaces* **2010**, *79*, 113–125. https://doi.org/10.1016/j.colsurfb.2010.03.039.

(259) Bag, B. G.; Das, S.; Hasan, S. N.; Chandan Barai, A. Nanoarchitectures by Hierarchical Self-Assembly of Ursolic Acid: Entrapment and Release of Fluorophores Including Anticancer Drug Doxorubicin. *RSC Adv.* **2017**, *7*, 18136–18143. https://doi.org/10.1039/C7RA02123B.

(260) Zhu, G.; Hu, R.; Zhao, Z.; Chen, Z.; Zhang, X.; Tan, W. Noncanonical Self-Assembly of Multifunctional DNA Nanoflowers for Biomedical Applications. *J. Am. Chem. Soc.* **2013**, *135*, 16438–16445. https://doi.org/10.1021/ja406115e.

(261) Zhuang, J.; Kuo, C.-H.; Chou, L.-Y.; Liu, D.-Y.; Weerapana, E.; Tsung, C.-K. Optimized Metal–Organic-Framework Nanospheres for Drug Delivery: Evaluation of Small-Molecule Encapsulation. *ACS Nano* **2014**, *8*, 2812–2819. https://doi.org/10.1021/nn406590q.

(262) Zhou, J.; Du, X.; Xu, B. Regulating the Rate of Molecular Self-Assembly for Targeting Cancer Cells. *Angew. Chem.* **2016**, *128*, 5864–5869. https://doi.org/10.1002/ange.201600753.

(263) Zhan, J.; Cai, Y.; He, S.; Wang, L.; Yang, Z. Tandem Molecular Self-Assembly in Liver Cancer Cells. *Angew. Chem.* **2018**, *130*, 1831–1834. https://doi.org/10.1002/ange.201710237.

(264) Lin, Y.; Qiao, Y.; Cheng, X.; Yan, Y.; Li, Z.; Huang, J. Hydrotropic Salt Promotes Anionic Surfactant Self-Assembly into Vesicles and Ultralong Fibers. *J. Colloid Interface Sci.* **2012**, *369*, 238–244. https://doi.org/10.1016/j.jcis.2011.11.067.

(265) Ghoroghchian, P. P.; Li, G.; Levine, D. H.; Davis, K. P.; Bates, F. S.; Hammer, D. A.; Therien, M. J. Bioresorbable Vesicles Formed through Spontaneous Self-Assembly of Amphiphilic Poly(Ethylene Oxide)- *Block* -Polycaprolactone. *Macromolecules* **2006**, *39*, 1673–1675. https://doi.org/10.1021/ma0519009.

(266) Lomora, M.; Garni, M.; Itel, F.; Tanner, P.; Spulber, M.; Palivan, C. G. Polymersomes with Engineered Ion Selective Permeability as Stimuli-Responsive Nanocompartments with Preserved Architecture. *Biomaterials* **2015**, *53*, 406–414. https://doi.org/10.1016/j.biomaterials.2015.02.080.

(267) Percec, V.; Wilson, D. A.; Leowanawat, P.; Wilson, C. J.; Hughes, A. D.; Kaucher, M. S.; Hammer, D. A.; Levine, D. H.; Kim, A. J.; Bates, F. S.; Davis, K. P.; Lodge, T. P.; Klein, M. L.; DeVane, R. H.; Aqad, E.; Rosen, B. M.; Argintaru, A. O.; Sienkowska, M. J.; Rissanen, K.; Nummelin, S.; Ropponen, J. Self-Assembly of Janus Dendrimers into Uniform Dendrimersomes and Other Complex Architectures. *Science* **2010**, *328*, 1009–1014. https://doi.org/10.1126/science.1185547.

(268) Qiu, F.; Tu, C.; Wang, R.; Zhu, L.; Chen, Y.; Tong, G.; Zhu, B.; He, L.; Yan, D.; Zhu, X. Emission Enhancement of Conjugated Polymers through Self-Assembly of Unimolecular Micelles to Multi-Micelle Aggregates. *Chem. Commun.* **2011**, *47*, 9678. https://doi.org/10.1039/c1cc13587b.

(269) Okesola, B. O.; Wu, Y.; Derkus, B.; Gani, S.; Wu, D.; Knani, D.; Smith, D. K.; Adams, D. J.; Mata, A. Supramolecular Self-Assembly To Control Structural and Biological Properties of Multicomponent Hydrogels. *Chem. Mater.* **2019**, *31*, 7883–7897. https://doi.org/10.1021/acs.chemmater.9b01882.
(270) Shen, J.; Xin, X.; Liu, T.; Wang, S.; Yang, Y.; Luan, X.; Xu, G.; Yuan, S. Ionic Self-Assembly of a Giant Vesicle as a Smart Microcarrier and Microreactor. *Langmuir* **2016**, *32*, 9548–9556. https://doi.org/10.1021/acs.langmuir.6b01829.
(271) Kumar, N. S. S.; Varghese, S.; Narayan, G.; Das, S. Hierarchical Self-Assembly of Donor–Acceptor-Substituted Butadiene Amphiphiles into Photoresponsive Vesicles and Gels. *Angew. Chem. Int. Ed.* **2006**, *45*, 6317–6321. https://doi.org/10.1002/anie.200602088.
(272) Qiu, H.; Hudson, Z. M.; Winnik, M. A.; Manners, I. Multidimensional Hierarchical Self-Assembly of Amphiphilic Cylindrical Block Comicelles. *Science* **2015**, *347*, 1329–1332. https://doi.org/10.1126/science.1261816.
(273) Dou, H.; Li, M.; Qiao, Y.; Harniman, R.; Li, X.; Boott, C. E.; Mann, S.; Manners, I. Higher-Order Assembly of Crystalline Cylindrical Micelles into Membrane-Extendable Colloidosomes. *Nat. Commun.* **2017**, *8*, 426. https://doi.org/10.1038/s41467-017-00465-z.
(274) Hudson, Z. M.; Lunn, D. J.; Winnik, M. A.; Manners, I. Colour-Tunable Fluorescent Multiblock Micelles. *Nat. Commun.* **2014**, *5*, 3372. https://doi.org/10.1038/ncomms4372.
(275) Wang, X.; Miller, D. S.; Bukusoglu, E.; de Pablo, J. J.; Abbott, N. L. Topological Defects in Liquid Crystals as Templates for Molecular Self-Assembly. *Nat. Mater.* **2016**, *15*, 106–112. https://doi.org/10.1038/nmat4421.
(276) Nakayama, M.; Kajiyama, S.; Kumamoto, A.; Nishimura, T.; Ikuhara, Y.; Yamato, M.; Kato, T. Stimuli-Responsive Hydroxyapatite Liquid Crystal with Macroscopically Controllable Ordering and Magneto-Optical Functions. *Nat. Commun.* **2018**, *9*, 568. https://doi.org/10.1038/s41467-018-02932-7.
(277) Jia, L.; Liu, M.; Di Cicco, A.; Albouy, P.-A.; Brissault, B.; Penelle, J.; Boileau, S.; Barbier, V.; Li, M.-H. Self-Assembly of Amphiphilic Liquid Crystal Polymers Obtained from a Cyclopropane-1,1-Dicarboxylate Bearing a Cholesteryl Mesogen. *Langmuir* **2012**, *28*, 11215–11224. https://doi.org/10.1021/la301860b.
(278) Zhang, H.; Yu, M.; Song, A.; Song, Y.; Xin, X.; Shen, J.; Yuan, S. Modulating Hierarchical Self-Assembly Behavior of a Peptide Amphiphile/Nonionic Surfactant Mixed System. *RSC Adv.* **2016**, *6*, 9186–9193. https://doi.org/10.1039/C5RA25437J.
(279) Wall, B. D.; Diegelmann, S. R.; Zhang, S.; Dawidczyk, T. J.; Wilson, W. L.; Katz, H. E.; Mao, H.-Q.; Tovar, J. D. Aligned Macroscopic Domains of Optoelectronic Nanostructures Prepared via Shear-Flow Assembly of Peptide Hydrogels. *Adv. Mater.* **2011**, *23*, 5009–5014. https://doi.org/10.1002/adma.201102963.
(280) Lu, Q.; Bai, S.; Ding, Z.; Guo, H.; Shao, Z.; Zhu, H.; Kaplan, D. L. Hydrogel Assembly with Hierarchical Alignment by Balancing Electrostatic Forces. *Adv. Mater. Interfaces* **2016**, *3*, 1500687. https://doi.org/10.1002/admi.201500687.
(281) Zhou, J.; Du, X.; Gao, Y.; Shi, J.; Xu, B. Aromatic–Aromatic Interactions Enhance Interfiber Contacts for Enzymatic Formation of a Spontaneously Aligned Supramolecular Hydrogel. *J. Am. Chem. Soc.* **2014**, *136*, 2970–2973. https://doi.org/10.1021/ja4127399.
(282) Xu, S.; Lin, Y.; Huang, J.; Li, Z.; Xu, X.; Zhang, L. Construction of High Strength Hollow Fibers by Self-Assembly of a Stiff Polysaccharide with Short Branches in Water. *J. Mater. Chem. A* **2013**, *1*, 4198. https://doi.org/10.1039/c3ta00050h.
(283) Bo, H. G.; Geng, Y.; Discher, D. E.; Hellweg, T.; Brandt, A. Organization of Self-Assembled Peptide-Polymer Nanofibers in Solution. **2008**, *41*, 8.
(284) Feng, X.; Tousley, M. E.; Cowan, M. G.; Wiesenauer, B. R.; Nejati, S.; Choo, Y.; Noble, R. D.; Elimelech, M.; Gin, D. L.; Osuji, C. O. Scalable Fabrication of Polymer Membranes with Vertically

Aligned 1 Nm Pores by Magnetic Field Directed Self-Assembly. *ACS Nano* **2014**, *8*, 11977–11986. https://doi.org/10.1021/nn505037b.

(285) Zhang, S.; Greenfield, M. A.; Mata, A.; Palmer, L. C.; Bitton, R.; Mantei, J. R.; Aparicio, C.; de la Cruz, M. O.; Stupp, S. I. A Self-Assembly Pathway to Aligned Monodomain Gels. *Nat. Mater.* **2010**, *9*, 594–601. https://doi.org/10.1038/nmat2778.

(286) Robin, M. P.; O'Reilly, R. K. Strategies for Preparing Fluorescently Labelled Polymer Nanoparticles. *Polym. Int.* **2015**, *64*, 174–182. https://doi.org/10.1002/pi.4842.

(287) Dai, M.; Jungmann, R.; Yin, P. Optical Imaging of Individual Biomolecules in Densely Packed Clusters. *Nat. Nanotechnol.* **2016**, *11*, 798–807. https://doi.org/10.1038/nnano.2016.95.

(288) Kubota, R.; Tanaka, W.; Hamachi, I. Microscopic Imaging Techniques for Molecular Assemblies: Electron, Atomic Force, and Confocal Microscopies. *Chem. Rev.* **2021**, acs.chemrev.0c01334. https://doi.org/10.1021/acs.chemrev.0c01334.

(289) Vladár, A. E.; Postek, M. T.; Ming, B. On the Sub-Nanometer Resolution of Scanning Electron and Helium Ion Microscopes. *Microsc. Today* **2009**, *17*, 6–13. https://doi.org/10.1017/S1551929500054420.

(290) Patterson, J. P.; Sanchez, A. M.; Petzetakis, N.; Smart, T. P.; Epps, III, T. H.; Portman, I.; Wilson, N. R.; O'Reilly, R. K. A Simple Approach to Characterizing Block Copolymer Assemblies: Graphene Oxide Supports for High Contrast Multi-Technique Imaging. *Soft Matter* **2012**, *8*, 3322. https://doi.org/10.1039/c2sm07040e.

(291) Goldstein, J. I.; Newbury, D. E.; Michael, J. R.; Ritchie, N. W. M.; Scott, J. H. J.; Joy, D. C. *Scanning Electron Microscopy and X-Ray Microanalysis*; Springer New York: New York, NY, 2018. https://doi.org/10.1007/978-1-4939-6676-9.

(292) Scanning Electron Microscopy (SEM). In *Electron Microscopy of Polymers*; Springer Berlin Heidelberg: Berlin, Heidelberg, 2008; pp 87–120. https://doi.org/10.1007/978-3-540-36352-1_5.

(293) Butler, J. H.; Joy, D. C.; Bradley, G. F.; Krause, S. J. Low-Voltage Scanning Electron Microscopy of Polymers. *Polymer* **1995**, *36*, 1781–1790. https://doi.org/10.1016/0032-3861(95)90924-Q.

(294) Goldstein, J. I.; Newbury, D. E.; Echlin, P.; Joy, D. C.; Romig, A. D.; Lyman, C. E.; Fiori, C.; Lifshin, E. Coating and Conductivity Techniques for SEM and Microanalysis. In *Scanning Electron Microscopy and X-Ray Microanalysis*; Springer US: Boston, MA, 1992; pp 671–740. https://doi.org/10.1007/978-1-4613-0491-3_13.

(295) Aston, R. Evaluation of the Impact of Freezing Preparation Techniques on the Characterisation of Alginate Hydrogels by Cryo-SEM. *Eur. Polym. J.* **2016**, 15.

(296) Ruozi, B.; Belletti, D.; Tombesi, A.; Tosi, G.; Bondioli, L.; Forni, F.; Maria Angela Vandelli. AFM, ESEM, TEM, and CLSM in Liposomal Characterization: A Comparative Study. *Int. J. Nanomedicine* **2011**, 557. https://doi.org/10.2147/IJN.S14615.

(297) Zankel, A.; Nachtnebel, M.; Mayrhofer, C.; Wewerka, K.; Müllner, T. Characterisation of Polymers in the Scanning Electron Microscope—From Low-Voltage Surface Imaging to the 3D Reconstruction of Specimens. In *Deformation and Fracture Behaviour of Polymer Materials*; Grellmann, W., Langer, B., Eds.; Springer Series in Materials Science; Springer International Publishing: Cham, 2017; Vol. 247, pp 95–108. https://doi.org/10.1007/978-3-319-41879-7_7.

(298) Inkson, B. J. Scanning Electron Microscopy (SEM) and Transmission Electron Microscopy (TEM) for Materials Characterization. In *Materials Characterization Using Nondestructive Evaluation (NDE) Methods*; Elsevier, 2016; pp 17–43. https://doi.org/10.1016/B978-0-08-100040-3.00002-X.

(299) Suga, M.; Asahina, S.; Sakuda, Y.; Kazumori, H.; Nishiyama, H.; Nokuo, T.; Alfredsson, V.; Kjellman, T.; Stevens, S. M.; Cho, H. S.; Cho, M.; Han, L.; Che, S.; Anderson, M. W.; Schüth, F.; Deng, H.; Yaghi, O. M.; Liu, Z.; Jeong, H. Y.; Stein, A.; Sakamoto, K.; Ryoo, R.; Terasaki, O. Recent Progress in Scanning Electron Microscopy for the Characterization of Fine Structural Details of Nano

Materials. *Prog. Solid State Chem.* **2014**, *42*, 1–21. https://doi.org/10.1016/j.progsolidstchem.2014.02.001.
(300) Koley, P.; Pramanik, A. Multilayer Vesicles, Tubes, Various Porous Structures and Organo Gels through the Solvent-Assisted Self-Assembly of Two Modified Tripeptides and Their Different Applications. *Soft Matter* **2012**, *8*, 5364. https://doi.org/10.1039/c2sm25205h.
(301) Rizvi, A.; Patel, U.; Ianiro, A.; Hurst, P. J.; Merham, J. G.; Patterson, J. P. Nonionic Block Copolymer Coacervates. *Macromolecules* **2020**, *53*, 6078–6086. https://doi.org/10.1021/acs.macromol.0c00979.
(302) Baral, A.; Roy, S.; Dehsorkhi, A.; Hamley, I. W.; Mohapatra, S.; Ghosh, S.; Banerjee, A. Assembly of an Injectable Noncytotoxic Peptide-Based Hydrogelator for Sustained Release of Drugs. **2014**, 8.
(303) Huang, R.; Qi, W.; Feng, L.; Su, R.; He, Z. Self-Assembling Peptide–Polysaccharide Hybrid Hydrogel as a Potential Carrier for Drug Delivery. *Soft Matter* **2011**, *7*, 6222. https://doi.org/10.1039/c1sm05375b.
(304) Naskar, J.; Palui, G.; Banerjee, A. Tetrapeptide-Based Hydrogels: For Encapsulation and Slow Release of an Anticancer Drug at Physiological PH. *J. Phys. Chem. B* **2009**, *113*, 11787–11792. https://doi.org/10.1021/jp904251j.
(305) Gao, Y.; Kuang, Y.; Guo, Z.-F.; Guo, Z.; Krauss, I. J.; Xu, B. Enzyme-Instructed Molecular Self-Assembly Confers Nanofibers and a Supramolecular Hydrogel of Taxol Derivative. *J. Am. Chem. Soc.* **2009**, *131*, 13576–13577. https://doi.org/10.1021/ja904411z.
(306) Orbach, R.; Adler-Abramovich, L.; Zigerson, S.; Mironi-Harpaz, I.; Seliktar, D.; Gazit, E. Self-Assembled Fmoc-Peptides as a Platform for the Formation of Nanostructures and Hydrogels. *Biomacromolecules* **2009**, *10*, 2646–2651. https://doi.org/10.1021/bm900584m.
(307) Matson, J. B. Peptide Self-Assembly for Crafting Functional Biological Materials. *Curr. Opin. Solid State Mater. Sci.* **2011**, 11.
(308) Mahler, A.; Reches, M.; Rechter, M.; Cohen, S.; Gazit, E. Rigid, Self-Assembled Hydrogel Composed of a Modified Aromatic Dipeptide. *Adv. Mater.* **2006**, *18*, 1365–1370. https://doi.org/10.1002/adma.200501765.
(309) Wei, Q.; Duan, J.; Ma, G.; Zhang, W.; Wang, Q.; Hu, Z. Enzymatic Crosslinking to Fabricate Antioxidant Peptide-Based Supramolecular Hydrogel for Improving Cutaneous Wound Healing. *J. Mater. Chem. B* **2019**, *7*, 2220–2225. https://doi.org/10.1039/C8TB03147A.
(310) O'Leary, L. E. R. Multi-Hierarchical Self-Assembly of a Collagen Mimetic Peptide from Triple Helix to Nanofibre and Hydrogel. *Nat. Chem.* **2011**, *3*, 8.
(311) Ko, J. W.; Choi, W. S.; Kim, J.; Kuk, S. K.; Lee, S. H.; Park, C. B. Self-Assembled Peptide-Carbon Nitride Hydrogel as a Light- Responsive Scaffold Material. **2017**, 6.
(312) Feng, L.; Wang, A.; Ren, P.; Wang, M.; Dong, Q.; Li, J.; Bai, S. Self-Assembled Peptide Hydrogel With Porphyrin as a Dopant for Enhanced Photocurrent Generation. *Colloid Interface Sci. Commun.* **2018**, *23*, 29–33. https://doi.org/10.1016/j.colcom.2018.01.006.
(313) Kim, J. H.; Nam, D. H.; Lee, Y. W.; Nam, Y. S.; Park, C. B. Self-Assembly of Metalloporphyrins into Light-Harvesting Peptide Nanofiber Hydrogels for Solar Water Oxidation. *Small* **2014**, *10*, 1272–1277. https://doi.org/10.1002/smll.201302627.
(314) Krieg, E.; Shirman, E.; Weissman, H.; Shimoni, E.; Wolf, S. G.; Pinkas, I.; Rybtchinski, B. Supramolecular Gel Based on a Perylene Diimide Dye: Multiple Stimuli Responsiveness, Robustness, and Photofunction. *J. Am. Chem. Soc.* **2009**, *131*, 14365–14373. https://doi.org/10.1021/ja903938g.
(315) Wang, Q.; Astruc, D. State of the Art and Prospects in Metal–Organic Framework (MOF)-Based and MOF-Derived Nanocatalysis. *Chem. Rev.* **2020**, *120*, 1438–1511. https://doi.org/10.1021/acs.chemrev.9b00223.

(316) Park, Y. K.; Choi, S. B.; Kim, H.; Kim, K.; Won, B.-H.; Choi, K.; Choi, J.-S.; Ahn, W.-S.; Won, N.; Kim, S.; Jung, D. H.; Choi, S.-H.; Kim, G.-H.; Cha, S.-S.; Jhon, Y. H.; Yang, J. K.; Kim, J. Crystal Structure and Guest Uptake of a Mesoporous Metal–Organic Framework Containing Cages of 3.9 and 4.7 Nm in Diameter. *Angew. Chem. Int. Ed.* **2007**, *46*, 8230–8233. https://doi.org/10.1002/anie.200702324.

(317) Xuan, W.; Zhu, C.; Liu, Y.; Cui, Y. Mesoporous Metal–Organic Framework Materials. *Chem Soc Rev* **2012**, *41*, 1677–1695. https://doi.org/10.1039/C1CS15196G.

(318) Deng, H.; Grunder, S.; Cordova, K. E.; Valente, C.; Furukawa, H.; Hmadeh, M.; Gandara, F.; Whalley, A. C.; Liu, Z.; Asahina, S.; Kazumori, H.; O'Keeffe, M.; Terasaki, O.; Stoddart, J. F.; Yaghi, O. M. Large-Pore Apertures in a Series of Metal-Organic Frameworks. *Science* **2012**, *336*, 1018–1023. https://doi.org/10.1126/science.1220131.

(319) Zheng, C.; Greer, H. F.; Chiang, C.-Y.; Zhou, W. Microstructural Study of the Formation Mechanism of Metal–Organic Framework MOF-5. *CrystEngComm* **2014**, *16*, 1064–1070. https://doi.org/10.1039/C3CE41291A.

(320) Cravillon, J.; Schröder, C. A.; Bux, H.; Rothkirch, A.; Caro, J.; Wiebcke, M. Formate Modulated Solvothermal Synthesis of ZIF-8 Investigated Using Time-Resolved in Situ X-Ray Diffraction and Scanning Electron Microscopy. *CrystEngComm* **2012**, *14*, 492–498. https://doi.org/10.1039/C1CE06002C.

(321) Cohen, H.; Nogues, C.; Ullien, D.; Daube, S.; Naaman, R.; Porath, D. Electrical Characterization of Self-Assembled Single- and Double-Stranded DNA Monolayers Using Conductive AFM. *Faraday Discuss* **2006**, *131*, 367–376. https://doi.org/10.1039/B507706K.

(322) Passeri, D.; Dong, C.; Reggente, M.; Angeloni, L.; Barteri, M.; Scaramuzzo, F. A.; De Angelis, F.; Marinelli, F.; Antonelli, F.; Rinaldi, F.; Marianecci, C.; Carafa, M.; Sorbo, A.; Sordi, D.; Arends, I. W.; Rossi, M. Magnetic Force Microscopy: Quantitative Issues in Biomaterials. *Biomatter* **2014**, *4*, e29507. https://doi.org/10.4161/biom.29507.

(323) Dazzi, A.; Prater, C. B. AFM-IR: Technology and Applications in Nanoscale Infrared Spectroscopy and Chemical Imaging. *Chem. Rev.* **2017**, *117*, 5146–5173. https://doi.org/10.1021/acs.chemrev.6b00448.

(324) Fukuma, T.; Higgins, M. J. Dynamic-Mode AFM in Liquid. In *Atomic Force Microscopy in Liquid*; John Wiley & Sons, Ltd; pp 87–119. https://doi.org/10.1002/9783527649808.ch4.

(325) Xu, K.; Sun, W.; Shao, Y.; Wei, F.; Zhang, X.; Wang, W.; Li, P. Recent Development of PeakForce Tapping Mode Atomic Force Microscopy and Its Applications on Nanoscience. *Nanotechnol. Rev.* **2018**, *7*, 605–621. https://doi.org/10.1515/ntrev-2018-0086.

(326) Zeng, C.; Vitale-Sullivan, C.; Ma, X. In Situ Atomic Force Microscopy Studies on Nucleation and Self-Assembly of Biogenic and Bio-Inspired Materials. *Minerals* **2017**, *7*, 158. https://doi.org/10.3390/min7090158.

(327) Pan, J.; Khadka, N. K. Kinetic Defects Induced by Melittin in Model Lipid Membranes: A Solution Atomic Force Microscopy Study. *J. Phys. Chem. B* **2016**, *120*, 4625–4634. https://doi.org/10.1021/acs.jpcb.6b02332.

(328) Mandemaker, L. D. B.; Filez, M.; Delen, G.; Tan, H.; Zhang, X.; Lohse, D.; Weckhuysen, B. M. Time-Resolved In Situ Liquid-Phase Atomic Force Microscopy and Infrared Nanospectroscopy during the Formation of Metal–Organic Framework Thin Films. *J. Phys. Chem. Lett.* **2018**, *9*, 1838–1844. https://doi.org/10.1021/acs.jpclett.8b00203.

(329) Jeong, J. S.; Ansaloni, A.; Mezzenga, R.; Lashuel, H. A.; Dietler, G. Novel Mechanistic Insight into the Molecular Basis of Amyloid Polymorphism and Secondary Nucleation during Amyloid Formation. *J. Mol. Biol.* **2013**, *425*, 1765–1781. https://doi.org/10.1016/j.jmb.2013.02.005.

(330) Neuman, K. C.; Nagy, A. Single-Molecule Force Spectroscopy: Optical Tweezers, Magnetic Tweezers and Atomic Force Microscopy. *Nat. Methods* **2008**, *5*, 491–505. https://doi.org/10.1038/nmeth.1218.

(331) Li, Y.; Liang, H.; Zhao, H.; Chen, D.; Liu, B.; Fuhs, T.; Dong, M. Characterization of Inter- and Intramolecular Interactions of Amyloid Fibrils by AFM-Based Single-Molecule Force Spectroscopy. *J. Nanomater.* **2016**, *2016*, 1–18. https://doi.org/10.1155/2016/5463201.
(332) Pera, I.; Stark, R.; Kappl, M.; Butt, H.-J.; Benfenati, F. Using the Atomic Force Microscope to Study the Interaction between Two Solid Supported Lipid Bilayers and the Influence of Synapsin I. *Biophys. J.* **2004**, *87*, 2446–2455. https://doi.org/10.1529/biophysj.104.044214.
(333) Kainz, B.; Oprzeska-Zingrebe, E. A.; Herrera, J. L. Biomaterial and Cellular Properties as Examined through Atomic Force Microscopy, Fluorescence Optical Microscopies and Spectroscopic Techniques. *Biotechnol. J.* **2014**, *9*, 51–60. https://doi.org/10.1002/biot.201300087.
(334) Dufrêne, Y. F.; Pelling, A. E. Force Nanoscopy of Cell Mechanics and Cell Adhesion. *Nanoscale* **2013**, *5*, 4094. https://doi.org/10.1039/c3nr00340j.
(335) Vahabi, S.; Salman, N.; Salman, B. N. Atomic Force Microscopy Application in Biological Research: A Review Study. *38*, 8.
(336) Qian, L.; Zhao, H. Nanoindentation of Soft Biological Materials. *Micromachines* **2018**, *9*, 654. https://doi.org/10.3390/mi9120654.
(337) Gan, Y. Atomic and Subnanometer Resolution in Ambient Conditions by Atomic Force Microscopy. *Surf. Sci. Rep.* **2009**, *64*, 99–121. https://doi.org/10.1016/j.surfrep.2008.12.001.
(338) Goksu, E. I.; Vanegas, J. M.; Blanchette, C. D.; Lin, W.-C.; Longo, M. L. AFM for Structure and Dynamics of Biomembranes. *Biochim. Biophys. Acta BBA - Biomembr.* **2009**, *1788*, 254–266. https://doi.org/10.1016/j.bbamem.2008.08.021.
(339) Galluzzi, M.; Biswas, C. S.; Wu, Y.; Wang, Q.; Du, B.; Stadler, F. J. Space-Resolved Quantitative Mechanical Measurements of Soft and Supersoft Materials by Atomic Force Microscopy. *NPG Asia Mater.* **2016**, *8*, e327–e327. https://doi.org/10.1038/am.2016.170.
(340) Moughton, A. O.; O'Reilly, R. K. Noncovalently Connected Micelles, Nanoparticles, and Metal-Functionalized Nanocages Using Supramolecular Self-Assembly. *J. Am. Chem. Soc.* **2008**, *130*, 8714–8725. https://doi.org/10.1021/ja800230k.
(341) Kotch, F. W.; Raines, R. T. Self-Assembly of Synthetic Collagen Triple Helices. *Proc. Natl. Acad. Sci.* **2006**, *103*, 3028–3033. https://doi.org/10.1073/pnas.0508783103.
(342) Bhosale, S. V.; Kalyankar, M. B.; Nalage, S. V.; Lalander, C. H.; Bhosale, S. V.; Langford, S. J.; Oliver, R. F. PH Dependent Molecular Self-Assembly of Octaphosphonate Porphyrin of Nanoscale Dimensions: Nanosphere and Nanorod Aggregates. *Int. J. Mol. Sci.* **2011**, *12*, 1464–1473. https://doi.org/10.3390/ijms12031464.
(343) Jaskiewicz, K.; Makowski, M.; Kappl, M.; Landfester, K.; Kroeger, A. Mechanical Properties of Poly(Dimethylsiloxane)- *Block* -Poly(2-Methyloxazoline) Polymersomes Probed by Atomic Force Microscopy. *Langmuir* **2012**, *28*, 12629–12636. https://doi.org/10.1021/la301608k.
(344) Li, C.; Chen, C.; Li, S.; Rasheed, T.; Huang, P.; Huang, T.; Zhang, Y.; Huang, W.; Zhou, Y. Self-Assembly and Functionalization of Alternating Copolymer Vesicles. *Polym. Chem.* **2017**, *8*, 4688–4695. https://doi.org/10.1039/C7PY00908A.
(345) Xu, Y.-X.; Wang, G.-T.; Zhao, X.; Jiang, X.-K.; Li, Z.-T. Self-Assembly of Vesicles from Amphiphilic Aromatic Amide-Based Oligomers. *Langmuir* **2009**, *25*, 2684–2688. https://doi.org/10.1021/la8034243.
(346) Seo, S. H.; Chang, J. Y.; Tew, G. N. Self-Assembled Vesicles from an Amphiphilicortho-Phenylene Ethynylene Macrocycle. *Angew. Chem. Int. Ed.* **2006**, *45*, 7526–7530. https://doi.org/10.1002/anie.200600688.
(347) Zhang, X.; Tanner, P.; Graff, A.; Palivan, C. G.; Meier, W. Mimicking the Cell Membrane with Block Copolymer Membranes. *J. Polym. Sci. Part Polym. Chem.* **2012**, *50*, 2293–2318. https://doi.org/10.1002/pola.26000.

(348) Sherman, S. E.; Xiao, Q.; Percec, V. Mimicking Complex Biological Membranes and Their Programmable Glycan Ligands with Dendrimersomes and Glycodendrimersomes. *Chem. Rev.* **2017**, *117*, 6538–6631. https://doi.org/10.1021/acs.chemrev.7b00097.
(349) Palmer, L. C.; Stupp, S. I. Molecular Self-Assembly into One-Dimensional Nanostructures. *Acc. Chem. Res.* **2008**, *41*, 1674–1684. https://doi.org/10.1021/ar8000926.
(350) Zhou, M.; Smith, A. M.; Das, A. K.; Hodson, N. W.; Collins, R. F.; Ulijn, R. V.; Gough, J. E. Self-Assembled Peptide-Based Hydrogels as Scaffolds for Anchorage-Dependent Cells. *Biomaterials* **2009**, *30*, 2523–2530. https://doi.org/10.1016/j.biomaterials.2009.01.010.
(351) Lu, K.; Jacob, J.; Thiyagarajan, P.; Conticello, V. P.; Lynn, D. G. Exploiting Amyloid Fibril Lamination for Nanotube Self-Assembly. *J. Am. Chem. Soc.* **2003**, *125*, 6391–6393. https://doi.org/10.1021/ja0341642.
(352) Mandal, D.; Shirazi, A. N.; Parang, K. Self-Assembly of Peptides to Nanostructures. *Org. Biomol. Chem.* **2014**, *12*, 3544–3561. https://doi.org/10.1039/C4OB00447G.
(353) Li, F.; Han, J.; Cao, T.; Lam, W.; Fan, B.; Tang, W.; Chen, S.; Fok, K. L.; Li, L. Design of Self-Assembly Dipeptide Hydrogels and Machine Learning via Their Chemical Features. *Proc. Natl. Acad. Sci.* **2019**, *116*, 11259–11264. https://doi.org/10.1073/pnas.1903376116.
(354) Wang, M.; Zhou, P.; Wang, J.; Zhao, Y.; Ma, H.; Lu, J. R.; Xu, H. Left or Right: How Does Amino Acid Chirality Affect the Handedness of Nanostructures Self-Assembled from Short Amphiphilic Peptides? *J. Am. Chem. Soc.* **2017**, *139*, 4185–4194. https://doi.org/10.1021/jacs.7b00847.
(355) Song, B.; Liu, B.; Jin, Y.; He, X.; Tang, D.; Wu, G.; Yin, S. Controlled Self-Assembly of Helical Nano-Ribbons Formed by Achiral Amphiphiles. *Nanoscale* **2015**, *7*, 930–935. https://doi.org/10.1039/C4NR06693F.
(356) Muraoka, T.; Cui, H.; Stupp, S. I. Quadruple Helix Formation of a Photoresponsive Peptide Amphiphile and Its Light-Triggered Dissociation into Single Fibers. *J. Am. Chem. Soc.* **2008**, *130*, 2946–2947. https://doi.org/10.1021/ja711213s.
(357) Wang, M.; Wang, J.; Zhou, P.; Deng, J.; Zhao, Y.; Sun, Y.; Yang, W.; Wang, D.; Li, Z.; Hu, X.; King, S. M.; Rogers, S. E.; Cox, H.; Waigh, T. A.; Yang, J.; Lu, J. R.; Xu, H. Nanoribbons Self-Assembled from Short Peptides Demonstrate the Formation of Polar Zippers between β-Sheets. *Nat. Commun.* **2018**, *9*, 5118. https://doi.org/10.1038/s41467-018-07583-2.
(358) Egawa, H.; Furusawa, K. Liposome Adhesion on Mica Surface Studied by Atomic Force Microscopy. *Langmuir* **1999**, *15*, 1660–1666. https://doi.org/10.1021/la980923w.
(359) Chen, Y.; Xue, S.; Xia, Q.; Li, H.; Liu, Q.; Li, B. S.; Tang, B. Z. Surface Effect on the Self-Assembly of Nanofibers Revealed by in Situ AFM Imaging and Molecular Simulation. *J. Phys. Chem. C* **2019**, *123*, 9292–9297. https://doi.org/10.1021/acs.jpcc.9b02205.
(360) Ando, T. High-Speed Atomic Force Microscopy and Its Future Prospects. *Biophys. Rev.* **2018**, *10*, 285–292. https://doi.org/10.1007/s12551-017-0356-5.
(361) Chen, J.; Zhu, E.; Liu, J.; Zhang, S.; Lin, Z.; Duan, X.; Heinz, H.; Huang, Y.; De Yoreo, J. J. Building Two-Dimensional Materials One Row at a Time: Avoiding the Nucleation Barrier. *Science* **2018**, *362*, 1135–1139. https://doi.org/10.1126/science.aau4146.
(362) Zhang, Q.; Lin, J.; Wang, L.; Xu, Z. Theoretical Modeling and Simulations of Self-Assembly of Copolymers in Solution. *Prog. Polym. Sci.* **2017**, *75*, 1–30. https://doi.org/10.1016/j.progpolymsci.2017.04.003.
(363) Orsi, M. Molecular Simulation of Self-Assembly. In *Self-assembling Biomaterials*; Elsevier, 2018; pp 305–318. https://doi.org/10.1016/B978-0-08-102015-9.00016-2.
(364) Gartner, T. E.; Jayaraman, A. Modeling and Simulations of Polymers: A Roadmap. *Macromolecules* **2019**, *52*, 755–786. https://doi.org/10.1021/acs.macromol.8b01836.

(365) Marrink, S. J.; de Vries, A. H.; Tieleman, D. P. Lipids on the Move: Simulations of Membrane Pores, Domains, Stalks and Curves. *Biochim. Biophys. Acta BBA - Biomembr.* **2009**, *1788*, 149–168. https://doi.org/10.1016/j.bbamem.2008.10.006.
(366) Taddese, T.; Anderson, R. L.; Bray, D. J.; Warren, P. B. Recent Advances in Particle-Based Simulation of Surfactants. *Curr. Opin. Colloid Interface Sci.* **2020**, *48*, 137–148. https://doi.org/10.1016/j.cocis.2020.04.001.
(367) Frederix, P. W. J. M.; Scott, G. G.; Abul-Haija, Y. M.; Kalafatovic, D.; Pappas, C. G.; Javid, N.; Hunt, N. T.; Ulijn, R. V.; Tuttle, T. Exploring the Sequence Space for (Tri-)Peptide Self-Assembly to Design and Discover New Hydrogels. *Nat. Chem.* **2015**, *7*, 30–37. https://doi.org/10.1038/nchem.2122.
(368) Liu, Y.; Yu, C.; Jin, H.; Jiang, B.; Zhu, X.; Zhou, Y.; Lu, Z.; Yan, D. A Supramolecular Janus Hyperbranched Polymer and Its Photoresponsive Self-Assembly of Vesicles with Narrow Size Distribution. *J. Am. Chem. Soc.* **2013**, *135*, 4765–4770. https://doi.org/10.1021/ja3122608.
(369) Wright, D. B.; Ramírez-Hernández, A.; Touve, M. A.; Carlini, A. S.; Thompson, M. P.; Patterson, J. P.; de Pablo, J. J.; Gianneschi, N. C. Enzyme-Induced Kinetic Control of Peptide–Polymer Micelle Morphology. *ACS Macro Lett.* **2019**, *8*, 676–681. https://doi.org/10.1021/acsmacrolett.8b00887.
(370) Klumpp, K.; Crépin, T. Capsid Proteins of Enveloped Viruses as Antiviral Drug Targets. *Curr. Opin. Virol.* **2014**, *5*, 63–71. https://doi.org/10.1016/j.coviro.2014.02.002.
(371) Hagan, M. F. Modeling Viral Capsid Assembly. In *Advances in Chemical Physics*; Rice, S. A., Dinner, A. R., Eds.; John Wiley & Sons, Inc.: Hoboken, New Jersey, 2014; pp 1–68. https://doi.org/10.1002/9781118755815.ch01.
(372) Perilla, J. R.; Hadden, J. A.; Goh, B. C.; Mayne, C. G.; Schulten, K. All-Atom Molecular Dynamics of Virus Capsids as Drug Targets. *J. Phys. Chem. Lett.* **2016**, *7*, 1836–1844. https://doi.org/10.1021/acs.jpclett.6b00517.
(373) Borhani, D. W.; Shaw, D. E. The Future of Molecular Dynamics Simulations in Drug Discovery. *J. Comput. Aided Mol. Des.* **2012**, *26*, 15–26. https://doi.org/10.1007/s10822-011-9517-y.
(374) Zhao, G.; Perilla, J. R.; Yufenyuy, E. L.; Meng, X.; Chen, B.; Ning, J.; Ahn, J.; Gronenborn, A. M.; Schulten, K.; Aiken, C.; Zhang, P. Mature HIV-1 Capsid Structure by Cryo-Electron Microscopy and All-Atom Molecular Dynamics. *Nature* **2013**, *497*, 643–646. https://doi.org/10.1038/nature12162.
(375) Irobalieva, R. N.; Fogg, J. M.; Catanese, D. J.; Sutthibutpong, T.; Chen, M.; Barker, A. K.; Ludtke, S. J.; Harris, S. A.; Schmid, M. F.; Chiu, W.; Zechiedrich, L. Structural Diversity of Supercoiled DNA. *Nat. Commun.* **2015**, *6*, 8440. https://doi.org/10.1038/ncomms9440.
(376) Sharp, T. H.; Bruning, M.; Mantell, J.; Sessions, R. B.; Thomson, A. R.; Zaccai, N. R.; Brady, R. L.; Verkade, P.; Woolfson, D. N. Cryo-Transmission Electron Microscopy Structure of a Gigadalton Peptide Fiber of de Novo Design. *Proc. Natl. Acad. Sci.* **2012**, *109*, 13266–13271. https://doi.org/10.1073/pnas.1118622109.
(377) Zhou, P.; Deng, L.; Wang, Y.; Lu, J. R.; Xu, H. Different Nanostructures Caused by Competition of Intra- and Inter- β -Sheet Interactions in Hierarchical Self-Assembly of Short Peptides. *J. Colloid Interface Sci.* **2016**, *464*, 219–228. https://doi.org/10.1016/j.jcis.2015.11.030.
(378) Zhao, Y.; Wang, J.; Deng, L.; Zhou, P.; Wang, S.; Wang, Y.; Xu, H.; Lu, J. R. Tuning the Self-Assembly of Short Peptides via Sequence Variations. *Langmuir* **2013**, *29*, 13457–13464. https://doi.org/10.1021/la402441w.
(379) Friedl, C.; Renger, T.; Berlepsch, H. v.; Ludwig, K.; Schmidt am Busch, M.; Megow, J. Structure Prediction of Self-Assembled Dye Aggregates from Cryogenic Transmission Electron Microscopy, Molecular Mechanics, and Theory of Optical Spectra. *J. Phys. Chem. C* **2016**, *120*, 19416–19433. https://doi.org/10.1021/acs.jpcc.6b05856.
(380) Parent, L. R.; Pham, C. H.; Patterson, J. P.; Denny, M. S.; Cohen, S. M.; Gianneschi, N. C.; Paesani, F. Pore Breathing of Metal–Organic Frameworks by Environmental Transmission Electron Microscopy. *J. Am. Chem. Soc.* **2017**, *139*, 13973–13976. https://doi.org/10.1021/jacs.7b06585.

(381) Feng, Y. H.; Zhang, X. P.; Zhao, Z. Q.; Guo, X. D. Dissipative Particle Dynamics Aided Design of Drug Delivery Systems: A Review. *Mol Pharm.* **2020**, 22.
(382) Wu, H.; Friedrich, H.; Patterson, J. P.; Sommerdijk, N. A. J. M.; Jonge, N. Liquid-Phase Electron Microscopy for Soft Matter Science and Biology. *Adv. Mater.* **2020**, *32*, 2001582. https://doi.org/10.1002/adma.202001582.
(383) Bai, Y.; Luo, Q.; Liu, J. Protein Self-Assembly via Supramolecular Strategies. *Chem. Soc. Rev.* **2016**, *45*, 2756–2767. https://doi.org/10.1039/C6CS00004E.
(384) Seeman, N. C. DNA in a Material World. *Nature* **2003**, *421*, 427–431. https://doi.org/10.1038/nature01406.
(385) Aldaye, F. A.; Palmer, A. L.; Sleiman, H. F. Assembling Materials with DNA as the Guide. *Science* **2008**, *321*, 1795–1799. https://doi.org/10.1126/science.1154533.
(386) Milles, S.; Jensen, M. R.; Communie, G.; Maurin, D.; Schoehn, G.; Ruigrok, R. W. H.; Blackledge, M. Self-Assembly of Measles Virus Nucleocapsid-like Particles: Kinetics and RNA Sequence Dependence. *Angew. Chem. Int. Ed.* **2016**, *55*, 9356–9360. https://doi.org/10.1002/anie.201602619.
(387) Integrating Enzymatic Self-Assembly and Mitochondria Targeting for Selectively Killing Cancer Cells without Acquired Drug Resistance | Journal of the American Chemical Society https://pubs.acs.org/doi/10.1021/jacs.6b09783 (accessed 2020 -11 -17).
(388) Fong, W.-K.; Negrini, R.; Vallooran, J. J.; Mezzenga, R.; Boyd, B. J. Responsive Self-Assembled Nanostructured Lipid Systems for Drug Delivery and Diagnostics. *J. Colloid Interface Sci.* **2016**, *484*, 320–339. https://doi.org/10.1016/j.jcis.2016.08.077.
(389) Das, S.; Das, M. K. Surface Modification of Resorcinarene-Based Self-Assembled Solid Lipid Nanoparticles for Drug Targeting. In *Surface Modification of Nanoparticles for Targeted Drug Delivery*; Pathak, Y. V., Ed.; Springer International Publishing: Cham, 2019; pp 311–329. https://doi.org/10.1007/978-3-030-06115-9_16.
(390) Date, T.; Sawada, T.; Serizawa, T. Self-Assembled Peptides on Polymer Surfaces: Towards Morphology-Dependent Surface Functionalization. *Soft Matter* **2013**, *9*, 3469–3472. https://doi.org/10.1039/C3SM27841G.
(391) Subburaman, K.; Pernodet, N.; Kwak, S. Y.; DiMasi, E.; Ge, S.; Zaitsev, V.; Ba, X.; Yang, N. L.; Rafailovich, M. Templated Biomineralization on Self-Assembled Protein Fibers. *Proc. Natl. Acad. Sci.* **2006**, *103*, 14672–14677. https://doi.org/10.1073/pnas.0602952103.
(392) Kyle, S.; Aggeli, A.; Ingham, E.; McPherson, M. J. Production of Self-Assembling Biomaterials for Tissue Engineering. *Trends Biotechnol.* **2009**, *27*, 423–433. https://doi.org/10.1016/j.tibtech.2009.04.002.
(393) Maji, S. K.; Schubert, D.; Rivier, C.; Lee, S.; Rivier, J. E.; Riek, R. Amyloid as a Depot for the Formulation of Long-Acting Drugs. *PLoS Biol.* **2008**, *6*, e17. https://doi.org/10.1371/journal.pbio.0060017.
(394) Standley, S. M.; Toft, D. J.; Cheng, H.; Soukasene, S.; Chen, J.; Raja, S. M.; Band, V.; Band, H.; Cryns, V. L.; Stupp, S. I. Induction of Cancer Cell Death by Self-Assembling Nanostructures Incorporating a Cytotoxic Peptide. *Cancer Res.* **2010**, *70*, 3020–3026. https://doi.org/10.1158/0008-5472.CAN-09-3267.
(395) Garmann, R. F.; Goldfain, A. M.; Manoharan, V. N. Measurements of the Self-Assembly Kinetics of Individual Viral Capsids around Their RNA Genome. *Proc. Natl. Acad. Sci.* **2019**, *116*, 22485–22490. https://doi.org/10.1073/pnas.1909223116.
(396) Brenner, S.; Horne, R. W. A Negative Staining Method for High Resolution Electron Microscopy of Viruses. *Biochim. Biophys. Acta* **1959**, *34*, 103–110. https://doi.org/10.1016/0006-3002(59)90237-9.

(397) Hall, C. E. Electron Densitometry of Stained Virus Particles. *J. Biophys. Biochem. Cytol.* **1955**, *1*, 1–12. https://doi.org/10.1083/jcb.1.1.1.
(398) Adrian, M.; Dubochet, J.; Lepault, J.; McDowall, A. W. Cryo-Electron Microscopy of Viruses. *Nature* **1984**, *308*, 32–36. https://doi.org/10.1038/308032a0.
(399) Murata, K.; Wolf, M. Cryo-Electron Microscopy for Structural Analysis of Dynamic Biological Macromolecules. *Biochim. Biophys. Acta BBA - Gen. Subj.* **2018**, *1862*, 324–334. https://doi.org/10.1016/j.bbagen.2017.07.020.
(400) Aronova, M. A.; Leapman, R. D. Development of Electron Energy Loss Spectroscopy in the Biological Sciences. *MRS Bull. Mater. Res. Soc.* **2012**, *37*, 53–62. https://doi.org/10.1557/mrs.2011.329.
(401) King, N. P.; Sheffler, W.; Sawaya, M. R.; Vollmar, B. S.; Sumida, J. P.; André, I.; Gonen, T.; Yeates, T. O.; Baker, D. Computational Design of Self-Assembling Protein Nanomaterials with Atomic Level Accuracy. *Science* **2012**, *336*, 1171–1174. https://doi.org/10.1126/science.1219364.
(402) Mio, K.; Ogura, T.; Kiyonaka, S.; Hiroaki, Y.; Tanimura, Y.; Fujiyoshi, Y.; Mori, Y.; Sato, C. The TRPC3 Channel Has a Large Internal Chamber Surrounded by Signal Sensing Antennas. *J. Mol. Biol.* **2007**, *367*, 373–383. https://doi.org/10.1016/j.jmb.2006.12.043.
(403) Liu, H.; Jin, L.; Koh, S. B. S.; Atanasov, I.; Schein, S.; Wu, L.; Zhou, Z. H. Atomic Structure of Human Adenovirus by Cryo-EM Reveals Interactions Among Protein Networks. *Science* **2010**, *329*, 1038–1043. https://doi.org/10.1126/science.1187433.
(404) Zhang, R.; Hu, X.; Khant, H.; Ludtke, S. J.; Chiu, W.; Schmid, M. F.; Frieden, C.; Lee, J.-M. Interprotofilament Interactions between Alzheimer's A□1–42 Peptides in Amyloid Fibrils Revealed by CryoEM. 6.
(405) Schmidt, A.; Annamalai, K.; Schmidt, M.; Grigorieff, N.; Fändrich, M. Cryo-EM Reveals the Steric Zipper Structure of a Light Chain-Derived Amyloid Fibril. *Proc. Natl. Acad. Sci.* **2016**, *113*, 6200–6205. https://doi.org/10.1073/pnas.1522282113.
(406) Amyloid Inspired Self-Assembled Peptide Nanofibers | Biomacromolecules https://pubs.acs.org/doi/abs/10.1021/bm301141h (accessed 2020 -11 -10).
(407) Artificial Peptide-Nanospheres Self-Assembled from Three-Way Junctions of β-Sheet-Forming Peptides | Journal of the American Chemical Society https://pubs.acs.org/doi/10.1021/ja052644i (accessed 2020 -11 -10).
(408) Bellomo, E. G.; Wyrsta, M. D.; Pakstis, L.; Pochan, D. J.; Deming, T. J. Stimuli-Responsive Polypeptide Vesicles by Conformation-Specific Assembly. *Nat. Mater.* **2004**, *3*, 244–248. https://doi.org/10.1038/nmat1093.
(409) Reches, M.; Gazit, E. Formation of Closed-Cage Nanostructures by Self-Assembly of Aromatic Dipeptides. *Nano Lett.* **2004**, *4*, 581–585. https://doi.org/10.1021/nl035159z.
(410) Multiphase Complex Coacervate Droplets | Journal of the American Chemical Society https://pubs.acs.org/doi/full/10.1021/jacs.9b11468 (accessed 2020 -11 -10).
(411) Banwell, E. F.; Abelardo, E. S.; Adams, D. J.; Birchall, M. A.; Corrigan, A.; Donald, A. M.; Kirkland, M.; Serpell, L. C.; Butler, M. F.; Woolfson, D. N. Rational Design and Application of Responsive α - Helical Peptide Hydrogels. *Nat. Mater.* **2009**, *8*, 596–600. https://doi.org/10.1038/nmat2479.
(412) Smith, A. M.; Williams, R. J.; Tang, C.; Coppo, P.; Collins, R. F.; Turner, M. L.; Saiani, A.; Ulijn, R. V. Fmoc-Diphenylalanine Self Assembles to a Hydrogel via a Novel Architecture Based on π–π Interlocked β-Sheets. *Adv. Mater.* **2008**, *20*, 37–41. https://doi.org/10.1002/adma.200701221.
(413) Kuzuya, A.; Komiyama, M. DNA Origami: Fold, Stick, and Beyond. *Nanoscale* **2010**, *2*, 309–321. https://doi.org/10.1039/B9NR00246D.
(414) Pinheiro, A. V.; Han, D.; Shih, W. M.; Yan, H. Challenges and Opportunities for Structural DNA Nanotechnology. *Nat. Nanotechnol.* **2011**, *6*, 763–772. https://doi.org/10.1038/nnano.2011.187.

(415) Dietz, H.; Douglas, S. M.; Shih, W. M. Folding DNA into Twisted and Curved Nanoscale Shapes. *Science* **2009**, *325*, 725–730. https://doi.org/10.1126/science.1174251.
(416) Zhang, S.; Chen, J.; Liu, J.; Pyles, H.; Baker, D.; Chen, C.-L.; Yoreo, J. J. D. Engineering Biomolecular Self-Assembly at Solid–Liquid Interfaces. *Adv. Mater. n/a*, 1905784. https://doi.org/10.1002/adma.201905784.
(417) Chen, B.; Frank, J. Two Promising Future Developments of Cryo-EM: Capturing Short-Lived States and Mapping a Continuum of States of a Macromolecule. *Microscopy* **2016**, *65*, 69–79. https://doi.org/10.1093/jmicro/dfv344.
(418) Brodin, J. D.; Ambroggio, X. I.; Tang, C.; Parent, K. N.; Baker, T. S.; Tezcan, F. A. Metal-Directed, Chemically Tunable Assembly of One-, Two- and Three-Dimensional Crystalline Protein Arrays. *Nat. Chem.* **2012**, *4*, 375–382. https://doi.org/10.1038/nchem.1290.
(419) Suzuki, Y.; Cardone, G.; Restrepo, D.; Zavattieri, P. D.; Baker, T. S.; Tezcan, F. A. Self-Assembly of Coherently Dynamic, Auxetic, Two-Dimensional Protein Crystals. *Nature* **2016**, *533*, 369–373. https://doi.org/10.1038/nature17633.
(420) Le Ferrand, H.; Duchamp, M.; Gabryelczyk, B.; Cai, H.; Miserez, A. Time-Resolved Observations of Liquid–Liquid Phase Separation at the Nanoscale Using in Situ Liquid Transmission Electron Microscopy. *J. Am. Chem. Soc.* **2019**, *141*, 7202–7210. https://doi.org/10.1021/jacs.9b03083.
(421) Hyman, A. A.; Weber, C. A.; Jülicher, F. Liquid-Liquid Phase Separation in Biology. *Annu. Rev. Cell Dev. Biol.* **2014**, *30*, 39–58. https://doi.org/10.1146/annurev-cellbio-100913-013325.
(422) Alberti, S.; Dormann, D. Liquid–Liquid Phase Separation in Disease. *Annu. Rev. Genet.* **2019**, *53*, 171–194. https://doi.org/10.1146/annurev-genet-112618-043527.
(423) Yuan, C.; Levin, A.; Chen, W.; Xing, R.; Zou, Q.; Herling, T. W.; Challa, P. K.; Knowles, T. P. J.; Yan, X. Nucleation and Growth of Amino Acid and Peptide Supramolecular Polymers through Liquid–Liquid Phase Separation. *Angew. Chem. Int. Ed.* **2019**, *58*, 18116–18123. https://doi.org/10.1002/anie.201911782.
(424) Iinuma, R.; Ke, Y.; Jungmann, R.; Schlichthaerle, T.; Woehrstein, J. B.; Yin, P. Polyhedra Self-Assembled from DNA Tripods and Characterized with 3D DNA-PAINT. *Science* **2014**, *344*, 65–69. https://doi.org/10.1126/science.1250944.
(425) Das, S.; Heasman, P.; Ben, T.; Qiu, S. Porous Organic Materials: Strategic Design and Structure–Function Correlation. *Chem. Rev.* **2017**, *117*, 1515–1563. https://doi.org/10.1021/acs.chemrev.6b00439.
(426) Jiao, J.; Gong, W.; Wu, X.; Yang, S.; Cui, Y. Multivariate Crystalline Porous Materials: Synthesis, Property and Potential Application. *Coord. Chem. Rev.* **2019**, *385*, 174–190. https://doi.org/10.1016/j.ccr.2019.01.016.
(427) Zhou, H.-C. "Joe"; Kitagawa, S. Metal–Organic Frameworks (MOFs). *Chem. Soc. Rev.* **2014**, *43*, 5415–5418. https://doi.org/10.1039/C4CS90059F.
(428) Reticular synthesis and the design of new materials | Nature https://www.nature.com/articles/nature01650 (accessed 2020 -09 -08).
(429) Li, P.-Z.; Su, J.; Liang, J.; Liu, J.; Zhang, Y.; Chen, H.; Zhao, Y. A Highly Porous Metal–Organic Framework for Large Organic Molecule Capture and Chromatographic Separation. *Chem. Commun.* **2017**, *53*, 3434–3437. https://doi.org/10.1039/C7CC01063J.
(430) Metal–Organic Framework Materials with Ultrahigh Surface Areas: Is the Sky the Limit? | Journal of the American Chemical Society https://pubs.acs.org/doi/10.1021/ja3055639 (accessed 2020 -10 -15).
(431) Scheurle, P. I.; Mähringer, A.; Jakowetz, A. C.; Hosseini, P.; Richter, A. F.; Wittstock, G.; Medina, D. D.; Bein, T. A Highly Crystalline Anthracene-Based MOF-74 Series Featuring Electrical Conductivity and Luminescence. *Nanoscale* **2019**, *11*, 20949–20955. https://doi.org/10.1039/C9NR05431F.

(432) Gong, X.; Gnanasekaran, K.; Chen, Z.; Robison, L.; Wasson, M. C.; Bentz, K. C.; Cohen, S. M.; Farha, O. K.; Gianneschi, N. C. Insights into the Structure and Dynamics of Metal–Organic Frameworks via Transmission Electron Microscopy. *J. Am. Chem. Soc.* **2020**, *142*, 17224–17235. https://doi.org/10.1021/jacs.0c08773.

(433) Sun, T.; Wei, L.; Chen, Y.; Ma, Y.; Zhang, Y.-B. Atomic-Level Characterization of Dynamics of a 3D Covalent Organic Framework by Cryo-Electron Diffraction Tomography. *J. Am. Chem. Soc.* **2019**, *141*, 10962–10966. https://doi.org/10.1021/jacs.9b04895.

(434) Rational Synthesis of Metal–Organic Framework Nanocubes and Nanosheets Using Selective Modulators and Their Morphology-Dependent Gas-Sorption Properties | Crystal Growth & Design https://pubs.acs.org/doi/abs/10.1021/cg300297p (accessed 2020 -10 -07).

(435) Liu, L.; Chen, Z.; Wang, J.; Zhang, D.; Zhu, Y.; Ling, S.; Huang, K.-W.; Belmabkhout, Y.; Adil, K.; Zhang, Y.; Slater, B.; Eddaoudi, M.; Han, Y. Imaging Defects and Their Evolution in a Metal–Organic Framework at Sub-Unit-Cell Resolution. *Nat. Chem.* **2019**, *11*, 622–628. https://doi.org/10.1038/s41557-019-0263-4.

(436) Wu, X.; Yue, H.; Zhang, Y.; Gao, X.; Li, X.; Wang, L.; Cao, Y.; Hou, M.; An, H.; Zhang, L.; Li, S.; Ma, J.; Lin, H.; Fu, Y.; Gu, H.; Lou, W.; Wei, W.; Zare, R. N.; Ge, J. Packaging and Delivering Enzymes by Amorphous Metal-Organic Frameworks. *Nat. Commun.* **2019**, *10*, 5165. https://doi.org/10.1038/s41467-019-13153-x.

(437) Hermes, S.; Schröder, F.; Amirjalayer, S.; Schmid, R.; Fischer, R. A. Loading of Porous Metal–Organic Open Frameworks with Organometallic CVD Precursors: Inclusion Compounds of the Type [LnM]A@MOF-5. *J. Mater. Chem.* **2006**, *16*, 2464–2472. https://doi.org/10.1039/B603664C.

(438) Ogata, A. F.; Rakowski, A. M.; Carpenter, B. P.; Fishman, D. A.; Merham, J. G.; Hurst, P. J.; Patterson, J. P. Direct Observation of Amorphous Precursor Phases in the Nucleation of Protein–Metal–Organic Frameworks. *J. Am. Chem. Soc.* **2020**, *142*, 1433–1442. https://doi.org/10.1021/jacs.9b11371.

(439) Smith, B. J.; Parent, L. R.; Overholts, A. C.; Beaucage, P. A.; Bisbey, R. P.; Chavez, A. D.; Hwang, N.; Park, C.; Evans, A. M.; Gianneschi, N. C.; Dichtel, W. R. Colloidal Covalent Organic Frameworks. *ACS Cent. Sci.* **2017**, *3*, 58–65. https://doi.org/10.1021/acscentsci.6b00331.

(440) Huang, Z.; Grape, E. S.; Li, J.; Inge, A. K.; Zou, X. 3D Electron Diffraction as an Important Technique for Structure Elucidation of Metal-Organic Frameworks and Covalent Organic Frameworks. *Coord. Chem. Rev.* **2021**, *427*, 213583. https://doi.org/10.1016/j.ccr.2020.213583.

(441) Banihashemi, F.; Bu, G.; Thaker, A.; Williams, D.; Lin, J. Y. S.; Nannenga, B. L. Beam-Sensitive Metal-Organic Framework Structure Determination by Microcrystal Electron Diffraction. *Ultramicroscopy* **2020**, *216*, 113048. https://doi.org/10.1016/j.ultramic.2020.113048.

(442) Zhu, L.; Zhang, D.; Xue, M.; Li, H.; Qiu, S. Direct Observations of the MOF (UiO-66) Structure by Transmission Electron Microscopy. *CrystEngComm* **2013**, *15*, 9356–9359. https://doi.org/10.1039/C3CE41122B.

(443) Denysenko, D.; Grzywa, M.; Tonigold, M.; Streppel, B.; Krkljus, I.; Hirscher, M.; Mugnaioli, E.; Kolb, U.; Hanss, J.; Volkmer, D. Elucidating Gating Effects for Hydrogen Sorption in MFU-4-Type Triazolate-Based Metal–Organic Frameworks Featuring Different Pore Sizes. *Chem. – Eur. J.* **2011**, *17*, 1837–1848. https://doi.org/10.1002/chem.201001872.

(444) Smolders, S.; Willhammar, T.; Krajnc, A.; Sentosun, K.; Wharmby, M. T.; Lomachenko, K. A.; Bals, S.; Mali, G.; Roeffaers, M. B. J.; De Vos, D. E.; Bueken, B. A Titanium(IV)-Based Metal–Organic Framework Featuring Defect-Rich Ti-O Sheets as an Oxidative Desulfurization Catalyst. *Angew. Chem.* **2019**, *131*, 9258–9263. https://doi.org/10.1002/ange.201904347.

(445) Feyand, M.; Mugnaioli, E.; Vermoortele, F.; Bueken, B.; Dieterich, J. M.; Reimer, T.; Kolb, U.; de Vos, D.; Stock, N. Automated Diffraction Tomography for the Structure Elucidation of Twinned, Sub-Micrometer Crystals of a Highly Porous, Catalytically Active Bismuth Metal–Organic

Framework. *Angew. Chem. Int. Ed.* **2012**, *51*, 10373–10376. https://doi.org/10.1002/anie.201204963.
(446) Richards, V. Imaging Grain Boundaries in a Two-Dimensional Polymer. *Commun. Chem.* **2020**, *3*, 1–2. https://doi.org/10.1038/s42004-020-00380-3.
(447) Evans, A. M.; Parent, L. R.; Flanders, N. C.; Bisbey, R. P.; Vitaku, E.; Kirschner, M. S.; Schaller, R. D.; Chen, L. X.; Gianneschi, N. C.; Dichtel, W. R. Seeded Growth of Single-Crystal Two-Dimensional Covalent Organic Frameworks. *Science* **2018**, *361*, 52–57. https://doi.org/10.1126/science.aar7883.
(448) Insight and Control of the Crystal Growth of Zeolitic Imidazolate Framework ZIF-67 by Atomic Force Microscopy and Mass Spectrometry | Crystal Growth & Design https://pubs.acs.org/doi/abs/10.1021/acs.cgd.7b01058 (accessed 2020 -10 -15).
(449) Moh, P. Y.; Cubillas, P.; Anderson, M. W.; Attfield, M. P. Revelation of the Molecular Assembly of the Nanoporous Metal Organic Framework ZIF-8. *J. Am. Chem. Soc.* **2011**, *133*, 13304–13307. https://doi.org/10.1021/ja205900f.
(450) Tolentino, M. Q.; Hartmann, A. K.; Loe, D. T.; Rouge, J. L. Controlled Release of Small Molecules and Proteins from DNA-Surfactant Stabilized Metal Organic Frameworks. *J. Mater. Chem. B* **2020**, *8*, 5627–5635. https://doi.org/10.1039/D0TB00767F.
(451) Uemura, T.; Yanai, N.; Kitagawa, S. Polymerization Reactions in Porous Coordination Polymers. *Chem. Soc. Rev.* **2009**, *38*, 1228–1236. https://doi.org/10.1039/B802583P.
(452) Lian, X.; Fang, Y.; Joseph, E.; Wang, Q.; Li, J.; Banerjee, S.; Lollar, C.; Wang, X.; Zhou, H.-C. Enzyme–MOF (Metal–Organic Framework) Composites. *Chem. Soc. Rev.* **2017**, *46*, 3386–3401. https://doi.org/10.1039/C7CS00058H.
(453) Liang, K.; Ricco, R.; Doherty, C. M.; Styles, M. J.; Bell, S.; Kirby, N.; Mudie, S.; Haylock, D.; Hill, A. J.; Doonan, C. J.; Falcaro, P. Biomimetic Mineralization of Metal-Organic Frameworks as Protective Coatings for Biomacromolecules. *Nat. Commun.* **2015**, *6*, 7240. https://doi.org/10.1038/ncomms8240.
(454) Meilikhov, M.; Yusenko, K.; Esken, D.; Turner, S.; Van Tendeloo, G.; Fischer, R. A. Metals@MOFs – Loading MOFs with Metal Nanoparticles for Hybrid Functions. *Eur. J. Inorg. Chem.* **2010**, *2010*, 3701–3714. https://doi.org/10.1002/ejic.201000473.
(455) Lyu, F.; Zhang, Y.; Zare, R. N.; Ge, J.; Liu, Z. One-Pot Synthesis of Protein-Embedded Metal–Organic Frameworks with Enhanced Biological Activities. *Nano Lett.* **2014**, *14*, 5761–5765. https://doi.org/10.1021/nl5026419.
(456) Van Vleet, M. J.; Weng, T.; Li, X.; Schmidt, J. R. In Situ, Time-Resolved, and Mechanistic Studies of Metal–Organic Framework Nucleation and Growth. *Chem. Rev.* **2018**, *118*, 3681–3721. https://doi.org/10.1021/acs.chemrev.7b00582.
(457) Colón, Y. J.; Guo, A. Z.; Antony, L. W.; Hoffmann, K. Q.; de Pablo, J. J. Free Energy of Metal-Organic Framework Self-Assembly. *J. Chem. Phys.* **2019**, *150*, 104502. https://doi.org/10.1063/1.5063588.
(458) Structural Evolution of Zeolitic Imidazolate Framework-8 | Journal of the American Chemical Society https://pubs.acs.org/doi/10.1021/ja109268m (accessed 2020 -10 -15).
(459) Gnanasekaran, K.; Vailonis, K. M.; Jenkins, D. M.; Gianneschi, N. C. *In Situ* Monitoring of the Seeding and Growth of Silver Metal–Organic Nanotubes by Liquid-Cell Transmission Electron Microscopy. *ACS Nano* **2020**, *14*, 8735–8743. https://doi.org/10.1021/acsnano.0c03209.
(460) Kalaj, M.; Cohen, S. M. Postsynthetic Modification: An Enabling Technology for the Advancement of Metal–Organic Frameworks. *ACS Cent. Sci.* **2020**, *6*, 1046–1057. https://doi.org/10.1021/acscentsci.0c00690.
(461) Denny, M. S.; Parent, L. R.; Patterson, J. P.; Meena, S. K.; Pham, H.; Abellan, P.; Ramasse, Q. M.; Paesani, F.; Gianneschi, N. C.; Cohen, S. M. Transmission Electron Microscopy Reveals Deposition

of Metal Oxide Coatings onto Metal–Organic Frameworks. *J. Am. Chem. Soc.* **2018**, *140*, 1348–1357. https://doi.org/10.1021/jacs.7b10453.

(462) Israelachvili, J. N.; Mitchell, D. J.; Ninham, B. W. Theory of Self-Assembly of Hydrocarbon Amphiphiles into Micelles and Bilayers. *J. Chem. Soc. Faraday Trans. 2 Mol. Chem. Phys.* **1976**, *72*, 1525–1568. https://doi.org/10.1039/F29767201525.

(463) Tachibana, T.; Kambara, H. Enantiomorphism in the Helical Aggregate of Lithium 12-Hydroxystearate. *J. Am. Chem. Soc.* **1965**, *87*, 3015–3016. https://doi.org/10.1021/ja01091a046.

(464) Cui, H.; Webber, M. J.; Stupp, S. I. Self-Assembly of Peptide Amphiphiles: From Molecules to Nanostructures to Biomaterials. *Pept. Sci.* **2010**, *94*, 1–18. https://doi.org/10.1002/bip.21328.

(465) Gore, T.; Dori, Y.; Talmon, Y.; Tirrell, M.; Bianco-Peled, H. Self-Assembly of Model Collagen Peptide Amphiphiles. *Langmuir* **2001**, *17*, 5352–5360. https://doi.org/10.1021/la010223i.

(466) Parry, A. L.; Bomans, P. H. H.; Holder, S. J.; Sommerdijk, N. A. J. M.; Biagini, S. C. G. Cryo Electron Tomography Reveals Confined Complex Morphologies of Tripeptide-Containing Amphiphilic Double-Comb Diblock Copolymers. *Angew. Chem. Int. Ed.* **2008**, *47*, 8859–8862. https://doi.org/10.1002/anie.200802834.

(467) Zeng, G.; Qiu, L.; Wen, T. Recent Advances in Crystallization and Self-Assembly of Polypeptoid Polymers. *Polym. Cryst.* **2019**, *2*, e10065. https://doi.org/10.1002/pcr2.10065.

(468) Sun, J.; Jiang, X.; Lund, R.; Downing, K. H.; Balsara, N. P.; Zuckermann, R. N. Self-Assembly of Crystalline Nanotubes from Monodisperse Amphiphilic Diblock Copolypeptoid Tiles. *Proc. Natl. Acad. Sci. U. S. A.* **2016**, *113*, 3954–3959. https://doi.org/10.1073/pnas.1517169113.

(469) Rosales, A. M.; McCulloch, B. L.; Zuckermann, R. N.; Segalman, R. A. Tunable Phase Behavior of Polystyrene–Polypeptoid Block Copolymers. *Macromolecules* **2012**, *45*, 6027–6035. https://doi.org/10.1021/ma300625b.

(470) Sun, J.; Jiang, X.; Siegmund, A.; Connolly, M. D.; Downing, K. H.; Balsara, N. P.; Zuckermann, R. N. Morphology and Proton Transport in Humidified Phosphonated Peptoid Block Copolymers. *Macromolecules* **2016**, *49*, 3083–3090. https://doi.org/10.1021/acs.macromol.6b00353.

(471) Nam, K. T.; Shelby, S. A.; Choi, P. H.; Marciel, A. B.; Chen, R.; Tan, L.; Chu, T. K.; Mesch, R. A.; Lee, B.-C.; Connolly, M. D.; Kisielowski, C.; Zuckermann, R. N. Free-Floating Ultrathin Two-Dimensional Crystals from Sequence-Specific Peptoid Polymers. *Nat. Mater.* **2010**, *9*, 454–460. https://doi.org/10.1038/nmat2742.

(472) Lee, C.-U.; Smart, T. P.; Guo, L.; Epps, T. H.; Zhang, D. Synthesis and Characterization of Amphiphilic Cyclic Diblock Copolypeptoids from N-Heterocyclic Carbene-Mediated Zwitterionic Polymerization of N-Substituted N-Carboxyanhydride. *Macromolecules* **2011**, *44*, 9574–9585. https://doi.org/10.1021/ma2020936.

(473) Armand, M.; Endres, F.; MacFarlane, D. R.; Ohno, H.; Scrosati, B. Ionic-Liquid Materials for the Electrochemical Challenges of the Future. *Nat. Mater.* **2009**, *8*, 621–629. https://doi.org/10.1038/nmat2448.

(474) Chen, S.; Kobayashi, K.; Kitaura, R.; Miyata, Y.; Shinohara, H. Direct HRTEM Observation of Ultrathin Freestanding Ionic Liquid Film on Carbon Nanotube Grid. *ACS Nano* **2011**, *5*, 4902–4908. https://doi.org/10.1021/nn2009968.

(475) Krieg, E.; Bastings, M. M. C.; Besenius, P.; Rybtchinski, B. Supramolecular Polymers in Aqueous Media. *Chem. Rev.* **2016**, *116*, 2414–2477. https://doi.org/10.1021/acs.chemrev.5b00369.

(476) Park, W. I.; Kim, Y.; Jeong, J. W.; Kim, K.; Yoo, J.-K.; Hur, Y. H.; Kim, J. M.; Thomas, E. L.; Alexander-Katz, A.; Jung, Y. S. Host-Guest Self-Assembly in Block Copolymer Blends. *Sci. Rep.* **2013**, *3*, 3190. https://doi.org/10.1038/srep03190.

(477) Bai, W.; Wang, Z.; Tong, J.; Mei, J.; Qin, A.; Sun, J. Z.; Tang, B. Z. A Self-Assembly Induced Emission System Constructed by the Host–Guest Interaction of AIE-Active Building Blocks. *Chem. Commun.* **2014**, *51*, 1089–1091. https://doi.org/10.1039/C4CC06510G.

(478) Bosman, A. W.; Janssen, H. M.; Meijer, E. W. About Dendrimers: Structure, Physical Properties, and Applications. *Chem. Rev.* **1999**, *99*, 1665–1688. https://doi.org/10.1021/cr970069y.
(479) Fréchet, J. M. J. Dendrimers and Supramolecular Chemistry. *Proc. Natl. Acad. Sci.* **2002**, *99*, 4782–4787. https://doi.org/10.1073/pnas.082013899.
(480) Mai, Y.; Eisenberg, A. Self-Assembly of Block Copolymers. *Chem. Soc. Rev.* **2012**, *41*, 5969–5985. https://doi.org/10.1039/C2CS35115C.
(481) Li, Z.; Kesselman, E.; Talmon, Y.; Hillmyer, M. A.; Lodge, T. P. Multicompartment Micelles from ABC Miktoarm Stars in Water. *Science* **2004**, *306*, 98–101. https://doi.org/10.1126/science.1103350.
(482) Choucair, A.; Eisenberg, A. Control of Amphiphilic Block Copolymer Morphologies Using Solution Conditions. *Eur. Phys. J. E Soft Matter* **2003**, *10*, 37–44. https://doi.org/10.1140/epje/e2003-00002-5.
(483) Epps, T. H.; Cochran, E. W.; Hardy, C. M.; Bailey, T. S.; Waletzko, R. S.; Bates, F. S. Network Phases in ABC Triblock Copolymers. *Macromolecules* **2004**, *37*, 7085–7088. https://doi.org/10.1021/ma0493426.
(484) Spontak, R. J.; Williams, M. C. Microstructural Response of SIm and SBS Block Copolymers to Heat Treatment. *Polym. J.* **1988**, *20*, 649–671. https://doi.org/10.1295/polymj.20.649.
(485) Jinnai, H.; Sawa, K.; Nishi, T. Direct Observation of Twisted Grain Boundary in a Block Copolymer Lamellar Nanostructure. *Macromolecules* **2006**, *39*, 5815–5819. https://doi.org/10.1021/ma0600153.
(486) Tosaka, M.; Danev, R.; Nagayama, K. Application of Phase Contrast Transmission Microscopic Methods to Polymer Materials. *Macromolecules* **2005**, *38*, 7884–7886. https://doi.org/10.1021/ma0512197.
(487) Jiang, X.; Balsara, N. P. High-Resolution Imaging of Unstained Polymer Materials. *ACS Appl. Polym. Mater.* **2021**. https://doi.org/10.1021/acsapm.1c00217.
(488) McKenzie, B. E.; Nudelman, F.; Bomans, P. H. H.; Holder, S. J.; Sommerdijk, N. A. J. M. Temperature-Responsive Nanospheres with Bicontinuous Internal Structures from a Semicrystalline Amphiphilic Block Copolymer. *J. Am. Chem. Soc.* **2010**, *132*, 10256–10259. https://doi.org/10.1021/ja102040u.
(489) Nudelman, F.; With, G. de; Sommerdijk, N. A. J. M. Cryo-Electron Tomography: 3-Dimensional Imaging of Soft Matter. *Soft Matter* **2010**, *7*, 17–24. https://doi.org/10.1039/C0SM00441C.
(490) Saito, N.; Liu, C.; Lodge, T. P.; Hillmyer, M. A. Multicompartment Micelle Morphology Evolution in Degradable Miktoarm Star Terpolymers. *ACS Nano* **2010**, *4*, 1907–1912. https://doi.org/10.1021/nn9016873.
(491) Sheth, T.; Seshadri, S.; Prileszky, T.; Helgeson, M. E. Multiple Nanoemulsions. *Nat. Rev. Mater.* **2020**. https://doi.org/10.1038/s41578-019-0161-9.
(492) Malo de Molina, P.; Zhang, M.; Bayles, A. V.; Helgeson, M. E. Oil-in-Water-in-Oil Multinanoemulsions for Templating Complex Nanoparticles. *Nano Lett.* **2016**, *16*, 7325–7332. https://doi.org/10.1021/acs.nanolett.6b02073.
(493) Zhang, M.; Corona, P. T.; Ruocco, N.; Alvarez, D.; Malo de Molina, P.; Mitragotri, S.; Helgeson, M. E. Controlling Complex Nanoemulsion Morphology Using Asymmetric Cosurfactants for the Preparation of Polymer Nanocapsules. *Langmuir* **2018**, *34*, 978–990. https://doi.org/10.1021/acs.langmuir.7b02843.
(494) Wu, S.-H.; Hung, Y.; Mou, C.-Y. Compartmentalized Hollow Silica Nanospheres Templated from Nanoemulsions. *Chem. Mater.* **2013**, *25*, 352–364. https://doi.org/10.1021/cm303116u.
(495) Sing, C. E.; Perry, S. L. Recent Progress in the Science of Complex Coacervation. *Soft Matter* **2020**, *16*, 2885–2914. https://doi.org/10.1039/D0SM00001A.

(496) Kim, S.; Huang, J.; Lee, Y.; Dutta, S.; Yoo, H. Y.; Jung, Y. M.; Jho, Y.; Zeng, H.; Hwang, D. S. Complexation and Coacervation of Like-Charged Polyelectrolytes Inspired by Mussels. *Proc. Natl. Acad. Sci.* **2016**, *113*, E847–E853. https://doi.org/10.1073/pnas.1521521113.
(497) Hanemann, T.; Szabó, D. V. Polymer-Nanoparticle Composites: From Synthesis to Modern Applications. *Materials* **2010**, *3*, 3468–3517. https://doi.org/10.3390/ma3063468.
(498) Weitkamp, A. W. The Acidic Constituents of Degras. A New Method of Structure Elucidation1. *J. Am. Chem. Soc.* **1945**, *67*, 447–454. https://doi.org/10.1021/ja01219a027.
(499) Hill, J. P.; Jin, W.; Kosaka, A.; Fukushima, T.; Ichihara, H.; Shimomura, T.; Ito, K.; Hashizume, T.; Ishii, N.; Aida, T. Self-Assembled Hexa-Peri-Hexabenzocoronene Graphitic Nanotube. *Science* **2004**, *304*, 1481–1483. https://doi.org/10.1126/science.1097789.
(500) Besenius, P.; Portale, G.; Bomans, P. H. H.; Janssen, H. M.; Palmans, A. R. A.; Meijer, E. W. Controlling the Growth and Shape of Chiral Supramolecular Polymers in Water. *Proc. Natl. Acad. Sci.* **2010**, *107*, 17888–17893. https://doi.org/10.1073/pnas.1009592107.
(501) Fryd, M. M.; Mason, T. G. Cerberus Nanoemulsions Produced by Multidroplet Flow-Induced Fusion. *Langmuir* **2013**, *29*, 15787–15793. https://doi.org/10.1021/la403817a.
(502) Demurtas, D.; Guichard, P.; Martiel, I.; Mezzenga, R.; Hébert, C.; Sagalowicz, L. Direct Visualization of Dispersed Lipid Bicontinuous Cubic Phases by Cryo-Electron Tomography. *Nat. Commun.* **2015**, *6*, 8915. https://doi.org/10.1038/ncomms9915.
(503) Jinnai, H.; Nishikawa, Y.; Spontak, R. J.; Smith, S. D.; Agard, D. A.; Hashimoto, T. Direct Measurement of Interfacial Curvature Distributions in a Bicontinuous Block Copolymer Morphology. *Phys. Rev. Lett.* **2000**, *84*, 518–521. https://doi.org/10.1103/PhysRevLett.84.518.
(504) Stupp, S. I.; LeBonheur, V.; Walker, K.; Li, L. S.; Huggins, K. E.; Keser, M.; Amstutz, A. Supramolecular Materials: Self-Organized Nanostructures. *Science* **1997**, *276*, 384–389. https://doi.org/10.1126/science.276.5311.384.
(505) Patterson, J. P.; Proetto, M. T.; Gianneschi, N. C. Soft Nanomaterials Analysed by in Situ Liquid TEM: Towards High Resolution Characterisation of Nanoparticles in Motion. *Perspect. Sci.* **2015**, *6*, 106–112. https://doi.org/10.1016/j.pisc.2015.10.003.
(506) Pashuck, E. T.; Stupp, S. I. Direct Observation of Morphological Tranformation from Twisted Ribbons into Helical Ribbons. *J. Am. Chem. Soc.* **2010**, *132*, 8819–8821. https://doi.org/10.1021/ja100613w.
(507) Li, C.; Tho, C. C.; Galaktionova, D.; Chen, X.; Král, P.; Mirsaidov, U. Dynamics of Amphiphilic Block Copolymers in an Aqueous Solution: Direct Imaging of Micelle Formation and Nanoparticle Encapsulation. *Nanoscale* **2019**, *11*, 2299–2305. https://doi.org/10.1039/C8NR08922A.
(508) Soubaneh, Y. D.; Pelletier, E.; Desbiens, I.; Rouleau, C. Radiolabeling of Amide Functionalized Multi-Walled Carbon Nanotubes for Bioaccumulation Study in Fish Bone Using Whole-Body Autoradiography. *Environ. Sci. Pollut. Res.* **2020**, *27*, 3756–3767. https://doi.org/10.1007/s11356-019-05794-8.
(509) Carver, J. A.; Simpson, A. L.; Rathi, R. P.; Normil, N.; Lee, A. G.; Force, M. D.; Fiocca, K. A.; Maley, C. E.; DiJoseph, K. M.; Goldstein, A. L.; Attari, A. A.; O'Malley, H. L.; Zaccaro, J. G.; McCampbell, N. M.; Wentz, C. A.; Long, J. E.; McQueen, L. M.; Sirch, F. J.; Johnson, B. K.; Divis, M. E.; Chorney, M. L.; DiStefano, S. L.; Yost, H. M.; Greyson, B. L.; Cid, E. A.; Lee, K.; Yhap, C. J.; Dong, M.; Thomas, D. L.; Banks, B. E.; Newman, R. B.; Rodriguez, J.; Segil, A. T.; Siberski, J. A.; Lobo, A. L.; Ellison, M. D. Functionalized Single-Walled Carbon Nanotubes and Nanographene Oxide to Overcome Antibiotic Resistance in Tetracycline-Resistant Escherichia Coli. *ACS Appl. Nano Mater.* **2020**, *3*, 3910–3921. https://doi.org/10.1021/acsanm.0c00677.
(510) Darrow, M.; Moore, J.; Doering, K.; Vandekerckhove, H.; Thaw, P.; King, R. Chameleon: Delivering Improved Sample Preparation for Single Particle CryoEM. *Microsc. Microanal.* **2020**, *26*, 332–333. https://doi.org/10.1017/S1431927620014270.

(511) Touve, M. A.; Wright, D. B.; Mu, C.; Sun, H.; Park, C.; Gianneschi, N. C. Block Copolymer Amphiphile Phase Diagrams by High-Throughput Transmission Electron Microscopy. *Macromolecules* **2019**, *52*, 5529–5537. https://doi.org/10.1021/acs.macromol.9b00563.
(512) Schorb, M.; Haberbosch, I.; Hagen, W. J. H.; Schwab, Y.; Mastronarde, D. N. Software Tools for Automated Transmission Electron Microscopy. *Nat. Methods* **2019**, *16*, 471–477. https://doi.org/10.1038/s41592-019-0396-9.
(513) Spurgeon, S. R.; Ophus, C.; Jones, L.; Petford-Long, A.; Kalinin, S. V.; Olszta, M. J.; Dunin-Borkowski, R. E.; Salmon, N.; Hattar, K.; Yang, W.-C. D.; Sharma, R.; Du, Y.; Chiaramonti, A.; Zheng, H.; Buck, E. C.; Kovarik, L.; Penn, R. L.; Li, D.; Zhang, X.; Murayama, M.; Taheri, M. L. Towards Data-Driven next-Generation Transmission Electron Microscopy. *Nat. Mater.* **2020**, 1–6. https://doi.org/10.1038/s41563-020-00833-z.
(514) Haberl, M. G.; Churas, C.; Tindall, L.; Boassa, D.; Phan, S.; Bushong, E. A.; Madany, M.; Akay, R.; Deerinck, T. J.; Peltier, S. T.; Ellisman, M. H. CDeep3M—Plug-and-Play Cloud-Based Deep Learning for Image Segmentation. *Nat. Methods* **2018**, *15*, 677–680. https://doi.org/10.1038/s41592-018-0106-z.
(515) Computational Reverse-Engineering Analysis for Scattering Experiments on Amphiphilic Block Polymer Solutions | Journal of the American Chemical Society https://pubs.acs.org/doi/abs/10.1021/jacs.9b08028 (accessed 2021 -01 -07).
(516) Van Vleet, M. J.; Weng, T.; Li, X.; Schmidt, J. R. In Situ, Time-Resolved, and Mechanistic Studies of Metal–Organic Framework Nucleation and Growth. *Chem. Rev.* **2018**, *118*, 3681–3721. https://doi.org/10.1021/acs.chemrev.7b00582.
(517) Idrobo, J. C. A New Resolution Quest in Electron Microscopy. *Nat. Rev. Mater.* **2020**, 1–3. https://doi.org/10.1038/s41578-020-00275-8.
(518) VandenBussche, E. J.; Flannigan, D. J. Reducing Radiation Damage in Soft Matter with Femtosecond-Timed Single-Electron Packets. *Nano Lett.* **2019**, *19*, 6687–6694. https://doi.org/10.1021/acs.nanolett.9b03074.
(519) Choe, H.; Ponomarev, I.; Montgomery, E.; Lau, J. W.; Zhu, Y.; Zhao, Y.; Liu, A.; Kanareykin, A.; Jing, C. Mitigation of Radiation Damage in Macromolecules via Tunable Ultrafast Stroboscopic TEM. *bioRxiv* **2020**, 2020.05.15.099036. https://doi.org/10.1101/2020.05.15.099036.
(520) Stevens, A.; Yang, H.; Carin, L.; Arslan, I.; Browning, N. D. The Potential for Bayesian Compressive Sensing to Significantly Reduce Electron Dose in High-Resolution STEM Images. *Microscopy* **2014**, *63*, 41–51. https://doi.org/10.1093/jmicro/dft042.
(521) Faruqi, A. R.; McMullan, G. Direct Imaging Detectors for Electron Microscopy. *Nucl. Instrum. Methods Phys. Res. Sect. Accel. Spectrometers Detect. Assoc. Equip.* **2018**, *878*, 180–190. https://doi.org/10.1016/j.nima.2017.07.037.
(522) Clough, R.; Kirkland, A. I. Chapter One - Direct Digital Electron Detectors. In *Advances in Imaging and Electron Physics*; Hawkes, P. W., Ed.; Elsevier, 2016; Vol. 198, pp 1–42. https://doi.org/10.1016/bs.aiep.2016.09.001.
(523) Faruqi, A. R.; Henderson, R.; McMullan, G. Chapter Two - Progress and Development of Direct Detectors for Electron Cryomicroscopy. In *Advances in Imaging and Electron Physics*; Hawkes, P. W., Ed.; Elsevier, 2015; Vol. 190, pp 103–141. https://doi.org/10.1016/bs.aiep.2015.03.002.
(524) Hetherington, C. Aberration Correction for TEM. *Mater. Today* **2004**, *7*, 50–55. https://doi.org/10.1016/S1369-7021(04)00571-1.
(525) Ogata, A. F.; Mirabello, G.; Rakowski, A. M.; Patterson, J. P. Revealing Nonclassical Nucleation Pathways Using Cryogenic Electron Microscopy. In *Crystallization via Nonclassical Pathways Volume 1: Nucleation, Assembly, Observation & Application*; ACS Symposium Series; American Chemical Society, 2020; Vol. 1358, pp 147–200. https://doi.org/10.1021/bk-2020-1358.ch007.

(526) Schaffer, M.; Pfeffer, S.; Mahamid, J.; Kleindiek, S.; Laugks, T.; Albert, S.; Engel, B. D.; Rummel, A.; Smith, A. J.; Baumeister, W.; Plitzko, J. M. A Cryo-FIB Lift-out Technique Enables Molecular-Resolution Cryo-ET within Native Caenorhabditis Elegans Tissue. *Nat. Methods* **2019**, *16*, 757–762. https://doi.org/10.1038/s41592-019-0497-5.

(527) Winey, M.; Meehl, J. B.; O'Toole, E. T.; Giddings, T. H. Conventional Transmission Electron Microscopy. *Mol. Biol. Cell* **2014**, *25*, 319–323. https://doi.org/10.1091/mbc.E12-12-0863.

(528) Scarff, C. A.; Fuller, M. J. G.; Thompson, R. F.; Iadaza, M. G. Variations on Negative Stain Electron Microscopy Methods: Tools for Tackling Challenging Systems. *J. Vis. Exp. JoVE* **2018**, No. 132. https://doi.org/10.3791/57199.

(529) Talmon, Y. Staining and Drying-Induced Artifacts in Electron Microscopy of Surfactant Dispersions. *J. Colloid Interface Sci.* **1983**, *93*, 366–382. https://doi.org/10.1016/0021-9797(83)90420-4.

(530) Wilson, N. R.; Pandey, P. A.; Beanland, R.; Young, R. J.; Kinloch, I. A.; Gong, L.; Liu, Z.; Suenaga, K.; Rourke, J. P.; York, S. J.; Sloan, J. Graphene Oxide: Structural Analysis and Application as a Highly Transparent Support for Electron Microscopy. *ACS Nano* **2009**, *3*, 2547–2556. https://doi.org/10.1021/nn900694t.

(531) Pantelic, R. S.; Meyer, J. C.; Kaiser, U.; Stahlberg, H. The Application of Graphene as a Sample Support in Transmission Electron Microscopy. *Solid State Commun.* **2012**, *152*, 1375–1382. https://doi.org/10.1016/j.ssc.2012.04.038.

(532) Put, M. W. P. van de; P. Patterson, J.; H. Bomans, P. H.; R. Wilson, N.; Friedrich, H.; Benthem, R. A. T. M. van; With, G. de; K. O'Reilly, R.; M. Sommerdijk, N. A. J. Graphene Oxide Single Sheets as Substrates for High Resolution CryoTEM. *Soft Matter* **2015**, *11*, 1265–1270. https://doi.org/10.1039/C4SM02587C.

(533) Nativ-Roth, E.; Regev, O.; Yerushalmi-Rozen, R. Shear-Induced Ordering of Micellar Arrays in the Presence of Single-Walled Carbon Nanotubes. *Chem. Commun.* **2008**, No. 17, 2037–2039. https://doi.org/10.1039/B718148E.

(534) Danino, D.; Talmon, Y.; Zana, R. Cryo-TEM of Thread-like Micelles: On-the-Grid Microstructural Transformations Induced during Specimen Preparation. *Colloids Surf. Physicochem. Eng. Asp.* **2000**, *169*, 67–73. https://doi.org/10.1016/S0927-7757(00)00418-0.

(535) ten Hove, J. B.; Wang, J.; van Oosterom, M. N.; van Leeuwen, F. W. B.; Velders, A. H. Size-Sorting and Pattern Formation of Nanoparticle-Loaded Micellar Superstructures in Biconcave Thin Films. *ACS Nano* **2017**, *11*, 11225–11231. https://doi.org/10.1021/acsnano.7b05541.

(536) Drulyte, I.; Johnson, R. M.; Hesketh, E. L.; Hurdiss, D. L.; Scarff, C. A.; Porav, S. A.; Ranson, N. A.; Muench, S. P.; Thompson, R. F. Approaches to Altering Particle Distributions in Cryo-Electron Microscopy Sample Preparation. *Acta Crystallogr. Sect. Struct. Biol.* **2018**, *74*, 560–571. https://doi.org/10.1107/S2059798318006496.

(537) *Liquid Cell Electron Microscopy*; Ross, F. M., Ed.; Advances in Microscopy and Microanalysis; Cambridge University Press: Cambridge, 2016. https://doi.org/10.1017/9781316337455.

(538) Mirsaidov, U.; Patterson, J. P.; Zheng, H. Liquid Phase Transmission Electron Microscopy for Imaging of Nanoscale Processes in Solution. *MRS Bull.* **2020**, *45*, 704–712. https://doi.org/10.1557/mrs.2020.222.

(539) Wu, J.; Shan, H.; Chen, W.; Gu, X.; Tao, P.; Song, C.; Shang, W.; Deng, T. In Situ Environmental TEM in Imaging Gas and Liquid Phase Chemical Reactions for Materials Research. *Adv. Mater.* **2016**, *28*, 9686–9712. https://doi.org/10.1002/adma.201602519.

(540) Williamson, M. J.; Tromp, R. M.; Vereecken, P. M.; Hull, R.; Ross, F. M. Dynamic Microscopy of Nanoscale Cluster Growth at the Solid–Liquid Interface. *Nat. Mater.* **2003**, *2*, 532–536. https://doi.org/10.1038/nmat944.

(541) Yuk, J. M.; Park, J.; Ercius, P.; Kim, K.; Hellebusch, D. J.; Crommie, M. F.; Lee, J. Y.; Zettl, A.; Alivisatos, A. P. High-Resolution EM of Colloidal Nanocrystal Growth Using Graphene Liquid Cells. *Science* **2012**, *336*, 61–64. https://doi.org/10.1126/science.1217654.

(542) Mehdi, B. L.; Qian, J.; Nasybulin, E.; Park, C.; Welch, D. A.; Faller, R.; Mehta, H.; Henderson, W. A.; Xu, W.; Wang, C. M.; Evans, J. E.; Liu, J.; Zhang, J.-G.; Mueller, K. T.; Browning, N. D. Observation and Quantification of Nanoscale Processes in Lithium Batteries by Operando Electrochemical (S)TEM. *Nano Lett.* **2015**, *15*, 2168–2173. https://doi.org/10.1021/acs.nanolett.5b00175.

(543) Cho, H.; Jones, M. R.; Nguyen, S. C.; Hauwiller, M. R.; Zettl, A.; Alivisatos, A. P. The Use of Graphene and Its Derivatives for Liquid-Phase Transmission Electron Microscopy of Radiation-Sensitive Specimens. *Nano Lett.* **2017**, *17*, 414–420. https://doi.org/10.1021/acs.nanolett.6b04383.

(544) de Jonge, N.; Houben, L.; Dunin-Borkowski, R. E.; Ross, F. M. Resolution and Aberration Correction in Liquid Cell Transmission Electron Microscopy. *Nat. Rev. Mater.* **2019**, *4*, 61–78. https://doi.org/10.1038/s41578-018-0071-2.

(545) Yalcin, A. O.; Nijs, B. de; Fan, Z.; Tichelaar, F. D.; Vanmaekelbergh, D.; Blaaderen, A. van; Vlugt, T. J. H.; Huis, M. A. van; Zandbergen, H. W. Core–Shell Reconfiguration through Thermal Annealing in FexO/CoFe2O4ordered 2D Nanocrystal Arrays. *Nanotechnology* **2014**, *25*, 055601. https://doi.org/10.1088/0957-4484/25/5/055601.

(546) Ren, D.; Ophus, C.; Chen, M.; Waller, L. A Multiple Scattering Algorithm for Three Dimensional Phase Contrast Atomic Electron Tomography. *Ultramicroscopy* **2020**, *208*, 112860. https://doi.org/10.1016/j.ultramic.2019.112860.

(547) Adam Dyson, M.; M. Sanchez, A.; P. Patterson, J.; K. O'Reilly, R.; Sloan, J.; R. Wilson, N. A New Approach to High Resolution, High Contrast Electron Microscopy of Macromolecular Block Copolymer Assemblies. *Soft Matter* **2013**, *9*, 3741–3749. https://doi.org/10.1039/C3SM27787A.

(548) Cheng, Y. Single-Particle Cryo-EM at Crystallographic Resolution. *Cell* **2015**, *161*, 450–457. https://doi.org/10.1016/j.cell.2015.03.049.

(549) Wan, W.; Briggs, J. A. G. Chapter Thirteen - Cryo-Electron Tomography and Subtomogram Averaging. In *Methods in Enzymology*; Crowther, R. A., Ed.; The Resolution Revolution: Recent Advances In cryoEM; Academic Press, 2016; Vol. 579, pp 329–367. https://doi.org/10.1016/bs.mie.2016.04.014.

(550) Phase Contrast Enhancement with Phase Plates in Biological Electron Microscopy | Microscopy Today | Cambridge Core https://www.cambridge.org/core/journals/microscopy-today/article/phase-contrast-enhancement-with-phase-plates-in-biological-electron-microscopy/0C27770CF007C9C033461316D156CE08 (accessed 2021 -01 -08).

(551) Goodhew, P. J.; Humphreys, J. *Electron Microscopy and Analysis*; CRC Press, 2000.

(552) Reimer, L.; Kohl, H. *Transmission Electron Microscopy: Physics of Image Formation*, 5th ed.; Springer Series in Optical Sciences; Springer-Verlag: New York, 2008. https://doi.org/10.1007/978-0-387-40093-8.

(553) Ou, Z.; Wang, Z.; Luo, B.; Luijten, E.; Chen, Q. Kinetic Pathways of Crystallization at the Nanoscale. *Nat. Mater.* **2020**, *19*, 450–455. https://doi.org/10.1038/s41563-019-0514-1.

(554) Kim, J.; Ou, Z.; Jones, M. R.; Song, X.; Chen, Q. Imaging the Polymerization of Multivalent Nanoparticles in Solution. *Nat. Commun.* **2017**, *8*, 761. https://doi.org/10.1038/s41467-017-00857-1.

(555) Woehl, T. J.; Moser, T.; Evans, J. E.; Ross, F. M. Electron-Beam-Driven Chemical Processes during Liquid Phase Transmission Electron Microscopy. *MRS Bull.* **2020**, *45*, 746–753. https://doi.org/10.1557/mrs.2020.227.

(556) Egerton, R. F. Mechanisms of Radiation Damage in Beam-Sensitive Specimens, for TEM Accelerating Voltages between 10 and 300 KV. *Microsc. Res. Tech.* **2012**, *75*, 1550–1556. https://doi.org/10.1002/jemt.22099.
(557) Hayward, S. B.; Glaeser, R. M. Radiation Damage of Purple Membrane at Low Temperature. *Ultramicroscopy* **1979**, *4*, 201–210. https://doi.org/10.1016/S0304-3991(79)90211-0.
(558) Peet, M. J.; Henderson, R.; Russo, C. J. The Energy Dependence of Contrast and Damage in Electron Cryomicroscopy of Biological Molecules. *Ultramicroscopy* **2019**, *203*, 125–131. https://doi.org/10.1016/j.ultramic.2019.02.007.
(559) Egerton, R. F.; Li, P.; Malac, M. Radiation Damage in the TEM and SEM. *Micron* **2004**, *35*, 399–409. https://doi.org/10.1016/j.micron.2004.02.003.
(560) Leijten, Z. J. W. A.; Keizer, A. D. A.; de With, G.; Friedrich, H. Quantitative Analysis of Electron Beam Damage in Organic Thin Films. *J. Phys. Chem. C* **2017**, *121*, 10552–10561. https://doi.org/10.1021/acs.jpcc.7b01749.
(561) Mehdi, B. L.; Stevens, A.; Kovarik, L.; Jiang, N.; Mehta, H.; Liyu, A.; Reehl, S.; Stanfill, B.; Luzi, L.; Hao, W.; Bramer, L.; Browning, N. D. Controlling the Spatio-Temporal Dose Distribution during STEM Imaging by Subsampled Acquisition: In-Situ Observations of Kinetic Processes in Liquids. *Appl. Phys. Lett.* **2019**, 6.
(562) Leary, R.; Saghi, Z.; Midgley, P. A.; Holland, D. J. Compressed Sensing Electron Tomography. *Ultramicroscopy* **2013**, *131*, 70–91. https://doi.org/10.1016/j.ultramic.2013.03.019.
(563) Stevens, A.; Yang, H.; Hao, W.; Jones, L.; Ophus, C.; Nellist, P. D.; Browning, N. D. Subsampled STEM-Ptychography. *Appl. Phys. Lett.* **2018**, *113*, 033104. https://doi.org/10.1063/1.5040496.
(564) Stevens, A.; Luzi, L.; Yang, H.; Kovarik, L.; Mehdi, B. L.; Liyu, A.; Gehm, M. E.; Browning, N. D. A Sub-Sampled Approach to Extremely Low-Dose STEM. *Appl. Phys. Lett.* **2018**, *112*, 043104. https://doi.org/10.1063/1.5016192.
(565) Egerton, R. F. Choice of Operating Voltage for a Transmission Electron Microscope. *Ultramicroscopy* **2014**, *145*, 85–93. https://doi.org/10.1016/j.ultramic.2013.10.019.
(566) Dubochet, J.; Adrian, M.; Chang, J.-J.; Homo, J.-C.; Lepault, J.; McDowall, A. W.; Schultz, P. Cryo-Electron Microscopy of Vitrified Specimens. *Q. Rev. Biophys.* **1988**, *21*, 129–228. https://doi.org/10.1017/S0033583500004297.
(567) VandenBussche, E. J.; Clark, C. P.; Holmes, R. J.; Flannigan, D. J. Mitigating Damage to Hybrid Perovskites Using Pulsed-Beam TEM. *ACS Omega* **2020**, *5*, 31867–31871. https://doi.org/10.1021/acsomega.0c04711.
(568) Kwon, O.-H.; Ortalan, V.; Zewail, A. H. Macromolecular Structural Dynamics Visualized by Pulsed Dose Control in 4D Electron Microscopy. *Proc. Natl. Acad. Sci.* **2011**, *108*, 6026–6031. https://doi.org/10.1073/pnas.1103109108.
(569) Jiang, N. Note on in Situ (Scanning) Transmission Electron Microscopy Study of Liquid Samples. *Ultramicroscopy* **2017**, *179*, 81–83. https://doi.org/10.1016/j.ultramic.2017.04.012.
(570) Jiang, N. Beam Damage by the Induced Electric Field in Transmission Electron Microscopy. *Micron* **2016**, *83*, 79–92. https://doi.org/10.1016/j.micron.2016.02.007.
(571) Su, H.; Mehdi, B. L.; Patterson, J. P.; Sommerdijk, N. A. J. M.; Browning, N. D.; Friedrich, H. Growth Kinetics of Cobalt Carbonate Nanoparticles Revealed by Liquid-Phase Scanning Transmission Electron Microscopy. *J. Phys. Chem. C* **2019**, *123*, 25448–25455. https://doi.org/10.1021/acs.jpcc.9b06078.
(572) Makitalo, M.; Foi, A. Optimal Inversion of the Generalized Anscombe Transformation for Poisson-Gaussian Noise. *IEEE Trans. Image Process.* **2013**, *22*, 91–103. https://doi.org/10.1109/TIP.2012.2202675.
(573) De Graef, M. *Introduction to Conventional Transmission Electron Microscopy*; Cambridge University Press: Cambridge, 2003. https://doi.org/10.1017/CBO9780511615092.

(574) Schneider, C. A.; Rasband, W. S.; Eliceiri, K. W. NIH Image to ImageJ: 25 Years of Image Analysis. *Nat. Methods* **2012**, *9*, 671–675. https://doi.org/10.1038/nmeth.2089.
(575) Arganda-Carreras, I.; Kaynig, V.; Rueden, C.; Eliceiri, K. W.; Schindelin, J.; Cardona, A.; Sebastian Seung, H. Trainable Weka Segmentation: A Machine Learning Tool for Microscopy Pixel Classification. *Bioinformatics* **2017**, *33*, 2424–2426. https://doi.org/10.1093/bioinformatics/btx180.
(576) Roels, J. An Interactive ImageJ Plugin for Semi-Automated Image Denoising in Electron Microscopy. 13.
(577) Schindelin, J.; Rueden, C. T.; Hiner, M. C.; Eliceiri, K. W. The ImageJ Ecosystem: An Open Platform for Biomedical Image Analysis. *Mol. Reprod. Dev.* **2015**, *82*, 518–529. https://doi.org/10.1002/mrd.22489.
(578) Meyer, C.; Dellby, N.; Hachtel, J. A.; Lovejoy, T.; Mittelberger, A.; Krivanek, O. Nion Swift: Open Source Image Processing Software for Instrument Control, Data Acquisition, Organization, Visualization, and Analysis Using Python. *Microsc. Microanal.* **2019**, *25*, 122–123. https://doi.org/10.1017/S143192761900134X.
(579) Sosa, J. M.; Huber, D. E.; Welk, B.; Fraser, H. L. Development and Application of MIPAR^{TM}: A Novel Software Package for Two- and Three-Dimensional Microstructural Characterization. *Integrating Mater. Manuf. Innov.* **2014**, *3*, 123–140. https://doi.org/10.1186/2193-9772-3-10.
(580) Zivanov, J.; Nakane, T.; Forsberg, B. O.; Kimanius, D.; Hagen, W. J.; Lindahl, E.; Scheres, S. H. New Tools for Automated High-Resolution Cryo-EM Structure Determination in RELION-3. *eLife* **2018**, *7*, e42166. https://doi.org/10.7554/eLife.42166.
(581) Orlova, E. V.; Saibil, H. R. Structural Analysis of Macromolecular Assemblies by Electron Microscopy. *Chem. Rev.* **2011**, *111*, 7710–7748. https://doi.org/10.1021/cr100353t.
(582) Kirkland, E. J. Computation in Electron Microscopy. *Acta Crystallogr. Sect. Found. Adv.* **2016**, *72*, 1–27. https://doi.org/10.1107/S205327331501757X.
(583) Kervrann, C.; Sanchez Sorzano, C. O.; Acton, S. T.; Olivo-Marin, J.-C.; Unser, M. A Guided Tour of Selected Image Processing and Analysis Methods for Fluorescence and Electron Microscopy. *IEEE J. Sel. Top. Signal Process.* **2016**, *10*, 6–30. https://doi.org/10.1109/JSTSP.2015.2505402.
(584) Reimer, L. *Transmission Electron Microscopy: Physics of Image Formation and Microanalysis*; Springer, 2013; Vol. 36.
(585) Crameri, F.; Shephard, G. E.; Heron, P. J. The Misuse of Colour in Science Communication. *Nat. Commun.* **2020**, *11*, 5444. https://doi.org/10.1038/s41467-020-19160-7.
(586) Al-Azzawi, A.; Ouadou, A.; Tanner, J. J.; Cheng, J. AutoCryoPicker: An Unsupervised Learning Approach for Fully Automated Single Particle Picking in Cryo-EM Images. *BMC Bioinformatics* **2019**, *20*, 326. https://doi.org/10.1186/s12859-019-2926-y.
(587) Kushwaha, H. S.; Tanwar, S.; Rathore, K. S.; Srivastava, S. De-Noising Filters for TEM (Transmission Electron Microscopy) Image of Nanomaterials. In *2012 Second International Conference on Advanced Computing & Communication Technologies*; IEEE: Rohtak,Haryana, India, 2012; pp 276–281. https://doi.org/10.1109/ACCT.2012.41.
(588) Yehliu, K.; Vander Wal, R. L.; Boehman, A. L. Development of an HRTEM Image Analysis Method to Quantify Carbon Nanostructure. *Combust. Flame* **2011**, *158*, 1837–1851. https://doi.org/10.1016/j.combustflame.2011.01.009.
(589) Du, H. A Nonlinear Filtering Algorithm for Denoising HR(S)TEM Micrographs. *Ultramicroscopy* **2015**, *151*, 62–67. https://doi.org/10.1016/j.ultramic.2014.11.012.
(590) Muneesawang, P.; Sirisathitkul, C. Size Measurement of Nanoparticle Assembly Using Multilevel Segmented TEM Images. *J. Nanomater.* **2015**, *2015*, 1–8. https://doi.org/10.1155/2015/790508.

(591) Meng, Y.; Zhang, Z.; Yin, H.; Ma, T. Automatic Detection of Particle Size Distribution by Image Analysis Based on Local Adaptive Canny Edge Detection and Modified Circular Hough Transform. *Micron* **2018**, *106*, 34–41. https://doi.org/10.1016/j.micron.2017.12.002.
(592) Otsu, N. A Tlreshold Selection Method from Gray-Level Histograms. 5.
(593) Perez, A. J.; Seyedhosseini, M.; Deerinck, T. J.; Bushong, E. A.; Panda, S.; Tasdizen, T.; Ellisman, M. H. A Workflow for the Automatic Segmentation of Organelles in Electron Microscopy Image Stacks. *Front. Neuroanat.* **2014**, *8*. https://doi.org/10.3389/fnana.2014.00126.
(594) Crouzier, L.; Delvallée, A.; Ducourtieux, S.; Devoille, L.; Tromas, C.; Feltin, N. A New Method for Measuring Nanoparticle Diameter from a Set of SEM Images Using a Remarkable Point. *Ultramicroscopy* **2019**, *207*, 112847. https://doi.org/10.1016/j.ultramic.2019.112847.
(595) Tasel, S. F.; Mumcuoglu, E. U.; Hassanpour, R. Z.; Perkins, G. A Validated Active Contour Method Driven by Parabolic Arc Model for Detection and Segmentation of Mitochondria. *J. Struct. Biol.* **2016**, *194*, 253–271. https://doi.org/10.1016/j.jsb.2016.03.002.
(596) Weber, G. H.; Ophus, C.; Ramakrishnan, L. Automated Labeling of Electron Microscopy Images Using Deep Learning. In *2018 IEEE/ACM Machine Learning in HPC Environments (MLHPC)*; IEEE: Dallas, TX, USA, 2018; pp 26–36. https://doi.org/10.1109/MLHPC.2018.8638633.
(597) Ouyang, J.; Liang, Z.; Chen, C.; Fu, Z.; Zhang, Y.; Liu, H. Cryo-Electron Microscope Image Denoising Based on the Geodesic Distance. *BMC Struct. Biol.* **2018**, *18*, 18. https://doi.org/10.1186/s12900-018-0094-3.
(598) Chiwoo Park; Huang, J. Z.; Ji, J. X.; Yu Ding. Segmentation, Inference and Classification of Partially Overlapping Nanoparticles. *IEEE Trans. Pattern Anal. Mach. Intell.* **2013**, *35*, 1–1. https://doi.org/10.1109/TPAMI.2012.163.
(599) Vo, G. D.; Park, C. Robust Regression for Image Binarization under Heavy Noise and Nonuniform Background. *Pattern Recognit.* **2018**, *81*, 224–239. https://doi.org/10.1016/j.patcog.2018.04.005.
(600) Cervera Gontard, L.; Ozkaya, D.; Dunin-Borkowski, R. E. A Simple Algorithm for Measuring Particle Size Distributions on an Uneven Background from TEM Images. *Ultramicroscopy* **2011**, *111*, 101–106. https://doi.org/10.1016/j.ultramic.2010.10.011.
(601) Jamali, V.; Hargus, C.; Ben Moshe, A.; Aghazadeh, A.; Ha, H. D.; Mandadapu, K. K.; Alivisatos, P. *Anomalous Nanoparticle Surface Diusion in Liquid Cell TEM Is Revealed by Deep Learning-Assisted Analysis*; preprint; 2020. https://doi.org/10.26434/chemrxiv.12894050.v1.
(602) Bakalis, E.; Parent, L. R.; Vratsanos, M.; Park, C.; Gianneschi, N. C.; Zerbetto, F. Complex Nanoparticle Diffusional Motion in Liquid-Cell Transmission Electron Microscopy. *J Phys Chem C* **2020**, 10.
(603) Jordan, M. I.; Mitchell, T. M. Machine Learning: Trends, Perspectives, and Prospects. *Science* **2015**, *349*, 255–260. https://doi.org/10.1126/science.aaa8415.
(604) Ziatdinov, M.; Dyck, O.; Maksov, A.; Li, X.; Sang, X.; Xiao, K.; Unocic, R. R.; Vasudevan, R.; Jesse, S.; Kalinin, S. V. Deep Learning of Atomically Resolved Scanning Transmission Electron Microscopy Images: Chemical Identification and Tracking Local Transformations. *ACS Nano* **2017**, 11.
(605) Madsen, J.; Liu, P.; Kling, J.; Wagner, J. B.; Hansen, T. W.; Winther, O.; Schiøtz, J. A Deep Learning Approach to Identify Local Structures in Atomic-Resolution Transmission Electron Microscopy Images. **2018**, 12.
(606) Hagita, K.; Higuchi, T.; Jinnai, H. Super-Resolution for Asymmetric Resolution of FIB-SEM 3D Imaging Using AI with Deep Learning. *Sci. Rep.* **2018**, *8*, 5877. https://doi.org/10.1038/s41598-018-24330-1.
(607) Ciresan, D.; Giusti, A.; Gambardella, L. M.; Schmidhuber, J. Deep Neural Networks Segment Neuronal Membranes in Electron Microscopy Images. 9.
(608) Park, C.; Ding, Y. Automating Material Image Analysis for Material Discovery. *MRS Commun.* **2019**, *9*, 545–555. https://doi.org/10.1557/mrc.2019.48.

(609) Spurgeon, S. R. Towards Data-Driven next-Generation Transmission Electron Microscopy. *Nat. Mater.* 6.

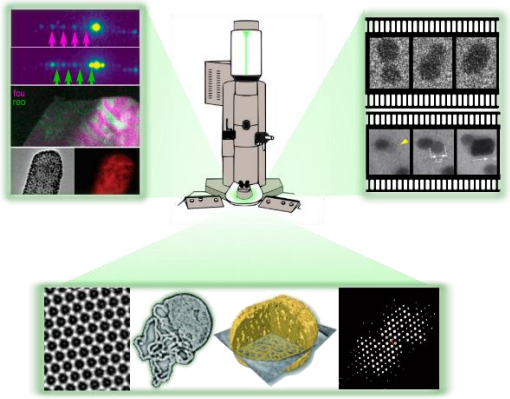

TOC